

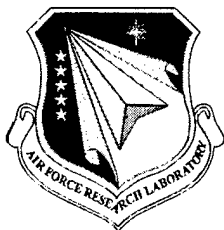
## **Celestial Background Scene Descriptor: Final Report**

**P.V. Noah  
M.A. Noah**

**Mission Research Corporation  
One Tara Boulevard, Suite 302  
Nashua, N.H. 03062-2801**

**February 2001**

**Approved for public release; distribution is unlimited.**




**AIR FORCE RESEARCH LABORATORY  
Space Vehicles Directorate  
29 Randolph Rd  
AIR FORCE MATERIEL COMMAND  
Hanscom AFB, MA 01731-3010**

---

**20030508 074**

This technical report has been reviewed and is approved for publication.



DEAN F. KIMBALL  
Contract Manager



Duane E. Paulsen  
Deputy Chief, AFRL/VSSS

Qualified requestors may obtain additional copies from the Defense Technical Information Center (DTIC). Other requests shall be referred to AFRL/VSSS.

If your address has changed, if you wish to be removed from the mailing list, or if the addressee is no longer employed by your organization, please notify AFRL/VSIM, 29 Randolph Road, Hanscom AFB, MA 01731-3010. This will assist us in maintaining a current mailing list.

Do not return copies of this report unless contractual obligations or notices on a specific document require that it be returned. Destroy by means that will prevent disclosure of contents or reconstruction of this document.

REPORT DOCUMENTATION PAGE		Form Approved OMB NO. 0704.0188	
Public reporting burden for this collection of information is estimated to average 1 hour per response, including the time for reviewing instructions, searching existing data sources, gathering and maintaining the data needed, and completing and reviewing the collection of information. Send comments regarding this burden estimate or any other aspect of the collection of information, including suggestions for reducing this burden, to Washington Headquarters Services, Directorate for Information Operations and Reports, 1215 Jefferson Davis Highway, suite 1204, Arlington, VA 22202-4302, and to the Office of Management and Budget, Paperwork Reduction Project (0704-0188), Washington, DC 20503.			
1. AGENCY USE ONLY (Leave Blank)	2. REPORT DATE February 2001	3. REPORT TYPE AND DATES COVERED FINAL REPORT	
4. TITLE AND SUBTITLE  Celestial Background Scene Descriptor – Final Report		5. FUNDING NUMBERS Contract: F19628-98-C-0028 PE: 63215C PR: S321 TA: GG WU: AA	
6. AUTHOR(s) Paul Noah Meg Noah Mission Research Corp. – Nashua, NH 03062		8. PERFORMING ORGANIZATION REPORT NUMBER	
7. PERFORMING ORGANIZATION NAME(S) AND ADDRESS(ES) Mission Research Corporation P.O. Drawer 719 Santa Barbara, CA 93102-0719		10. SPONSORING/MONITORING AGENCY REPORT NUMBER AFRL/VS-TR-2001-1584	
9. SPONSORING/MONITORING AGENCY NAME(S) AND ADDRESS(ES) Air Force Research Laboratory 29 Randolph Road Hanscom AFB, MA 01731 Contract Manager: Dr. Steven Price		11. SUPPLEMENTARY NOTES	
12a. DISTRIBUTION/AVAILABILITY STATEMENT  Approved for public release; distribution unlimited		12b. DISTRIBUTION CODE	
ABSTRACT (Maximum 200 words)  This report summarizes the results of the Celestial Background Scene Descriptor (CBSD) program. The goal of the CBSD program is to design, build, and validate a suite of FORTRAN codes that simulates the flux from the celestial background, in support of DoD developed optical and infrared sensor systems, realistic scenario generation, and the development of clutter removal algorithms. Components of the CBSD suite are CBSKY4 – stellar point sources (both catalogs of bright stars and a statistical model of faint stars are included), CBAMP4 – solar system objects (planets and asteroids modeled to better than 2 arc-second accuracy), CBZODY6 – solar system, zodiacal, dust, and CBHIII – galactic HII regions. The CBSD codes have a “dial-a-wavelength” capability between 0.2 and 35 μm which provides a predictive capability for new optical and infrared sensor systems. The suite can produce images, spectra, and catalogs of objects in units of radiance or irradiance (W/cm <sup>2</sup> , W/cm <sup>2</sup> /μm, W/cm <sup>2</sup> /sr, W/cm <sup>2</sup> /μm/sr, Jy, MJy, Jy/sr, and MJy/sr). Summaries of two validation reports for CBSKY4 and CBZODY6 are included as Appendices.			
14. SUBJECT TERMS Celestial, Infrared, Visible, Modeling, Stars, Zodiacal, Planets, HII regions			15. NUMBER OF PAGES
			16. PRICE CODE
17. SECURITY CLASSIFICATION OF REPORT UNCLASSIFIED	18. SECURITY CLASSIFICATION OF THIS PAGE UNCLASSIFIED	19. SECURITY CLASSIFICATION OF ABSTRACT UNCLASSIFIED	20. LIMITATION OF ABSTRACT None

## TABLE OF CONTENTS

<b>1 EXECUTIVE SUMMARY .....</b>	<b>1</b>
<b>2 DELIVERABLES .....</b>	<b>2</b>
<b>3 CBSD USERS .....</b>	<b>3</b>
3.1 SSGM .....	3
3.2 PLEXUS .....	4
<b>4 CBSD DATA PRODUCTS.....</b>	<b>7</b>
4.1 THE MAJOR COMPONENTS OF THE CELESTIAL BACKGROUND.....	7
4.2 MOVING SOLAR SYSTEM OBJECTS - CBAMP .....	7
4.3 THE DIFFUSE ZODIACAL BACKGROUND - CBZODY.....	8
4.4 THE GALACTIC POINT SOURCE BACKGROUND - CBSKY .....	10
4.5 SPATIALLY STRUCTURED SOURCES OF EMISSION.....	11
4.5.1 HII regions - CBHII .....	11
4.5.2 Infrared Cirrus - CBCIRRUS .....	12
4.6 THE CBSD SUITE OF ASTRONOMICAL CODES – CBSD4.....	13
<b>5 SUMMARY .....</b>	<b>15</b>
<b>REFERENCES.....</b>	<b>16</b>
<b>APPENDIX A: CBZODY6 VALIDATION SUMMARY .....</b>	<b>17</b>
A.1 INTRODUCTION .....	17
A.1.1 Goals of the CBZODY Program.....	17
A.1.2 About Zodiacal Light.....	17
A.2 CBZODY: A ZODIACAL LIGHT MODEL .....	18
A.3 DUST COMPOSITION AND VOLUME EMISSIVITY.....	20
A.4 VALIDATION.....	23
A.4.1 Parameter sets.....	23
A.4.2 CBZPARMS.DAT Parameter set.....	23
A.4.3 Band parameters .....	25
A.5 RESULTS .....	25
A.5.1 Reach et al. (1996) ISO comparison .....	26
A.5.2 Briotta, et al. 1976 Small Rocket Data.....	26
A.5.3 Extended Spectral Comparisons.....	27
A.5.4 Visible Zodiacal Table.....	29
A.5.5 Photometric observations.....	33
A.5.6 Visible Imaging .....	34
A.5.7 COBE CIO daily all sky coverage.....	38
A.5.8 South Ecliptic Pole (SEP).....	45
A.5.9 COBE CIO in-plane data .....	46
A.5.10 COBE CIO Psuedo-Scans .....	48
A.6 SUMMARY .....	49
<b>REFERENCES.....</b>	<b>50</b>
<b>APPENDIX B: CBSKY4 VALIDATION SUMMARY .....</b>	<b>52</b>
B.1 INTRODUCTION .....	52
B.2 MODEL VALIDATION RESULTS .....	52
B.3 PREDICTIVE VALIDATION OF STELLAR DISTRIBUTIONS.....	52
B.3.1 SKY4 Description .....	52
B.3.2 Cohen's Spectral Classes .....	53
B.3.3 Log(N) vs. Log(S) Plots.....	54
B.3.4 Validation Results For Select Regions .....	59
B.3.5 Validation Results For Zoom-In On Selected Confused Regions .....	62

B.3.6 Galactic North and South Poles .....	65
B.3.7 LMC/SMC Confused Region .....	66
B.3.8 Validation Results For Horizontal Slices .....	68
B.4 IMPLEMENTATION OF STAR CATALOGS .....	69
B.4.1 Historical Notes.....	69
B.4.2 Validation of Catalog Use.....	69
B.4.3 Finding Stars From Other Catalog Listings.....	71
B.4.4 Catalog Synthesis with Statistical Stars .....	73
B.5 PREDICTIVE POSITIONAL VALIDATION .....	74
B.5.1 Different Projections .....	74
B.5.2 Convolution Applied.....	74
B.6 PREDICTIVE FLUX VALIDATION.....	74
B.6.1 Flux of Arcturus In Different Bands.....	74
B.6.2 12 $\mu$ m Flux of Arcturus In Different Units .....	74
B.6.3 User-Defined Flux at Magnitude Zero .....	75
B.6.4 Convolution Applied.....	75
B.6.5 Comparison To Measured Spectra.....	78
B.7 CODE OPERATION VALIDATION.....	80
B.8 ACCEPTANCE REGRESSION VALIDATION.....	80
B.9 DOCUMENTATION VALIDATION.....	80
B.10 SUMMARY.....	81
<b>REFERENCES.....</b>	<b>82</b>

## LIST OF FIGURES

FIGURE 1: SSGM '99 SCENARIO CONSTRUCTION TOOL (SCT) MAIN WINDOW.....	3
FIGURE 2: SSGM '99 SPACE COMPONENT OUTPUT.....	4
FIGURE 3: SELECTION OF COMPONENTS.....	5
FIGURE 4: CBSD MODULE SPECIFICATION.....	6
FIGURE 5: PLEXUS OUTPUT.....	6
FIGURE 6: THIS IMAGE SHOWS JUPITER (CENTER) SURROUNDED BY THE FOUR GALILEAN STAEELLITES.....	8
FIGURE 7: COMPARISON OF CBZODY MODEL WITH IRAS DATA.....	10
FIGURE 8: A 12 $\mu$ m ALL SKY IMAGE WITH MOLECULAR CLOUDS.....	11
FIGURE 9: AN IMAGE LOOKING TOWARD THE GALACTIC CENTER SHOWING THE DISTRIBUTION OF HII SOURCES.....	12
FIGURE 10: THE GALACTIC CENTER WITH ALL COMPONENTS.....	13
FIGURE 11: IMAGE OF THE ZODIACAL LIGHT TAKEN FROM MT. STROMBOLI BY MARCO FULLE (USED WITH PERMISSION).....	14
FIGURE 12: A CBSD AND MODTRAN VIEW OF THE SAME REGION AS FIGURE 11.....	14
FIGURE A-1: IRAS DATA AND THE LORENTZIAN FIT.....	19
FIGURE A-2: TEMPERATURE PROFILES FOR ASTRONOMICAL SILICATE AT THREE DIFFERENT DISTANCES FROM THE SUN AS A FUNCTION OF PARTICLE SIZE.....	21
FIGURE A-3: VOLUME EMISSIVITY.....	22
FIGURE A-4: LATITUDINAL PROFILES OF DUST.....	25
FIGURE A-5: ISO SPECTRUM OF REACH ET AL. (1996).....	26
FIGURE A-6: SPECTRAL OUTPUT OF CBZODY COMPARED TO THE SPECTRUM OBTAINED BY BRIOTTA ET AL. (1976).....	27
FIGURE A-7: ZODIACAL SPECTRUM, SOLID LINE, COMPARED TO A VARIETY OF DATA SETS FOR A 90° ELONGATION... ..	28
FIGURE A-8: SIMILAR TO FIGURE A-7 THE ZODIACAL SPECTRUM OUT TO 300 $\mu$ m.....	29
FIGURE A-9: IMAGE OF THE ZODIACAL LIGHT TAKEN FROM MT. STROMBOLI BY MARCO FULLE.....	36
FIGURE A-10: A CBSD AND MODTRAN VIEW OF THE SAME REGION AS FIGURE A-9.....	37
FIGURE A-11: SINGLE BAND ATMOSPHERIC ATTENUATION.....	38
FIGURE A-12: LOCATION OF THE GALACTIC EXCLUSION ZONE.....	39
FIGURE A-13: MEAN DEVIATION ERRORS VERSUS HELIOCENTRIC ECLIPTIC LONGITUDE OF EARTH.....	43
FIGURE A-14: DAY 90005 BAND 4.....	44
FIGURE A-15: DAY 90005 BAND 5.....	44
FIGURE A-16: DAY 90005 BAND 6.....	45
FIGURE A-17: FINAL SEP FIT.....	46
FIGURE A-18: IN-PLANE FITS TO THE CIO DATA.....	47
FIGURE A-19: POLE-TO-POLE PSEUDO-SCANS.....	48
FIGURE B-1: OUTPUT FOR THE $L=10.43$ $B=0.13$ TEST CASE.....	60
FIGURE B-2: SMALL FIELD-OF-VIEW LOOKING AT THE GALACTIC CENTER.....	63
FIGURE B-3: SMALL FIELDS OF REGARD AT $L = 28^\circ$ AND $B = 0^\circ$ .....	64
FIGURE B-4: SMALL FIELD-OF-REGARD AT THE GALACTIC NORTH POLE.....	65
FIGURE B-5: MAGALLENIC CLOUD COMPARISONS.....	67
FIGURE B-6: K BAND CUMULATIVE STAR COUNTS OF HORIZONTAL SLICES PARALLEL TO THE GALACTIC PLANE.....	68
FIGURE B-7: EXAMPLE STAR ATLAS AND STAR CATALOG.....	69
FIGURE B-8: CHART OF THE CONSTELLATION ORION WITH THE BRIGHTEST STARS LABELED.....	70
FIGURE B-9: LOG(N) VS. LOG(S) PLOTS SHOW NO SKEWING WITH INCLUSION OF CATALOG STARS.....	73
FIGURE B-10: SURFACE PLOTS OF THE RESULT OF CONVOLVING ARCTURUS WITH DIFFERENT FUNCTIONS.....	78
FIGURE B-11: COMPARISON OF ORIGINAL COHEN CLASS 20 SPECTRUM (TOP) WITH THE GENERATED SPECTRUM FROM CBSKY4 (BOTTOM).....	79

## LIST OF TABLES

TABLE A-1: ADOPTED PARAMETERS IN CBZPARMS.DAT FILE.....	24
TABLE A-2: MODIFIED MIGRATING BAND PARAMETERS.....	25
TABLE A-3: ZODIACAL LIGHT BRIGHTNESS (LEINERT ET AL. 1997) IN UNITS OF $10^{-8} \text{ W M}^{-2} \text{ SR}^{-1} \mu\text{M}^{-1}$ FOR A WAVELENGTH OF $0.50 \mu\text{M}$ .....	30
TABLE A-4: ELONGATION OF OBSERVATION POINTS IN TABLE A-3.....	30
TABLE A-5: ZODIACAL LIGHT BRIGHTNESS FROM CBZODY6 IN UNITS OF $10^{-8} \text{ W M}^{-2} \text{ SR}^{-1} \mu\text{M}^{-1}$ FOR A WAVELENGTH OF $0.50 \mu\text{M}$ FOR 21 MARCH.....	31
TABLE A-6: ZODIACAL LIGHT BRIGHTNESS FROM CBZODY6 IN UNITS OF $10^{-8} \text{ W M}^{-2} \text{ SR}^{-1} \mu\text{M}^{-1}$ FOR A WAVELENGTH OF $0.50 \mu\text{M}$ FOR 21 JUNE.....	31
TABLE A-7: ZODIACAL LIGHT BRIGHTNESS FROM CBZODY6 IN UNITS OF $10^{-8} \text{ W M}^{-2} \text{ SR}^{-1} \mu\text{M}^{-1}$ FOR A WAVELENGTH OF $0.50 \mu\text{M}$ FOR 21 SEPTEMBER.....	32
TABLE A-8: ZODIACAL LIGHT BRIGHTNESS FROM CBZODY6 IN UNITS OF $10^{-8} \text{ W M}^{-2} \text{ SR}^{-1} \mu\text{M}^{-1}$ FOR A WAVELENGTH OF $0.50 \mu\text{M}$ FOR 21 DECEMBER.....	32
TABLE A-9: SCHMUDE (1999) POINTINGS FOR ZODIACAL LIGHT OBSERVATIONS.....	33
TABLE A-10: SCHMUDE B, V, AND B-V OBSERVATIONS FOR 6 MARCH 2000.....	33
TABLE A-11: CBZODY6 RUNS FOR THE 7 POINTS OF TABLE A-7.....	33
TABLE A-12: JOHNSON B & V PHOTOMETRIC PARAMETERS.....	33
TABLE A-13: POINT 4 BRIGHTNESS AS COMPUTE BY CBZODY6.....	34
TABLE A-14: ZODIACAL BRIGHTNESS FOR POINT 5.....	34
TABLE A-15: MEAN DEVIATIONS FOR ALL NLS PARAMETER FIT CIO DATASETS FOR BAND 5.....	40
TABLE A-16: MEAN DEVIATIONS AND STANDARD DEVIATIONS FOR ALL MODELED CIO DATASETS IN 3 BANDS USING GENERALIZED PARAMETER SET.....	41
TABLE A-17: AVERAGE OF ALL MEAN DEVIATIONS; THE MEAN DEVIATION OF ALL MODELED OBSERVATIONS.....	42
TABLE B-1: COHEN SPECTRAL CLASSIFICATION TYPES.....	54
TABLE B-2: TIMELINE OF STAR COUNT TECHNIQUES.....	55
TABLE B-3: COMPARISON OF APPARENT AND ABSOLUTE MAGNITUDES.....	57
TABLE B-4: THE 20 (APPARENT) BRIGHTEST STARS IN THE SKY (NOT INCLUDING THE SUN).....	58
TABLE B-5: MAY 1993 TEST REGIONS (K AND $12 \mu\text{M}$ BAND).....	59
TABLE B-6: FEBRUARY 1994 TEST REGIONS.....	61
TABLE B-7: CONFUSED-REGION CENTERS FOR ZOOM-IN.....	62
TABLE B-8: GALACTIC POLES FOR ZOOM-IN.....	65
TABLE B-9: CONFUSED REGIONS FOR ZOOM-IN.....	66
TABLE B-10: OUTPUT OF CBSKY4 FOR THE ORION REGION.....	70
TABLE B-11: THE BRIGHTEST IRAS STARS OF FIGURE B-8.....	70
TABLE B-12: CBSKY4 CATALOG STARS CORRESPONDING TO NASA ARCHIVE OF IR SPECTRA STARS (RA / DEC IN J2000).....	72
TABLE B-13: STAR COUNTS FOR OPTIONS OF STATISTICAL AND REAL STARS.....	73
TABLE B-14: CBSKY4 FLUX VALUES FOR ARCTURUS RUN FOR DIFFERENT OUTPUT SPECTRAL BAND OPTIONS.....	74
TABLE B-15: CBSKY4 $12\mu\text{M}$ FLUX VALUES FOR ARCTURUS RUN FOR DIFFERENT OUTPUT UNIT OPTIONS.....	75
TABLE B-16: FORMULAS FOR CONVERSION BETWEEN UNITS (USING $\text{W}/\text{CM}^2$ AS REFERENCE).....	75
TABLE B-17: CBSKY4 PARAMETERS USED FOR TESTING THE CONVOLUTION ROUTINE.....	76
TABLE B-18: CBSKY4 OUTPUT SHOWS CONVOLUTION PRESERVES TOTAL RADIANCE.....	77

## 1 Executive Summary

This report summarizes the results of the AFRL Celestial background Scene Descriptor (CBSD) project to design, build, and distribute a suite of astronomical modeling codes. The CBSD models predict the flux from astronomical sources for a given line-of-sight or field-of-view that would be detected by optical and infrared sensor systems. Codes are used for sensor development, realistic scenario generation, and development of clutter removal algorithms. The CBSD codes are currently in use by the MDA as a component of the Synthetic Scene Generation Model (SSGM) simulation package and as part of the AFRL PLEXUS Release 3, Version 2, atmospheric effects modeling suite.

The CBSD codes are a set of FORTRAN routines used to model the astronomical sky between 0.2 to 35 $\mu$ m.

Astronomical sources of infrared radiation provide a spectrally, spatially, and even temporally complex infrared background against which surveillance and reconnaissance systems must operate. The general nature and detailed character of this celestial background define the limits of system performance. Tradeoffs between detector size and number, magnitude of data processing, and the size and location of possible outage regions are forced by the intensity and structure of this background. An accurate description of the background at the wavelengths, sensitivities, and spatial resolutions projected for these systems is needed for design and performance analysis.

Although real data is certainly preferred to computer modeled results, such data simply does not exist at the specific wavelengths, sensitivity levels, and spatial resolution contemplated for surveillance systems. Therefore, development of a capability for generation of computer-synthesized celestial background scenes was mandated. This type of modeling capability must rely on existing empirical information, and the computer-modeled scenes must be consistent with relevant experimental data.



## 2 Deliverables

During the CBSD program the following reports have been delivered:

- **Technical Report 1: CBZODY: Reference Manual**
- **Technical Report 2: CBAMP: Reference Manual**
- **Technical Report 3: CBSD: The Celestial Background Scene Descriptor Version 3.0 – Installation and User’s Manual**
- **Technical Report 4: CSIMPS: A PROGRAM FOR DERIVING ASTEROID DIAMETERS AND ALBEDOS FROM IRAS DATA, User’s Manual**
- **Technical Report 5: CSIMPS: A PROGRAM FOR DERIVING ASTEROID DIAMETERS AND ALBEDOS FROM IRAS DATA, Software Final Report**
  - *Appendix A: CSIMPS Albedos and Diameters Catalog (FP202.txt)*
  - *Appendix B: CSIMPS Missed-Predictions Catalog (FP206.txt)*
  - *Appendix C: CSIMPS Reject Catalog (FP205.txt)*
  - *Appendix D: CSIMPS Singleton Catalog (FP203.txt)*
- **Technical Report 6: CBSKY4: Reference Manual**
- **Technical Report 7: CBSD: The Celestial Background Scene Descriptor Version 4.0 – Installation and User’s Manual**
- **Technical Report 8: Validation Report for the Celestial Background Scene Descriptor (CBSD) Zodiacal Emission (CBZODY6) Model**
- **Technical Report 9: Validation Report for the Celestial Background Scene Descriptor (CBSD) Stellar Point Source (CBSKY4) Model**

### 3 CBSD Users

#### 3.1 SSGM

The Synthetic Scene Generation Model (SSGM) (Figure 1) consists of computer software and input databases that provide the capability to generate two-dimensional time-sequenced scenes as well as other supporting data for use in the design, development, and testing of surveillance and weapons systems. The SSGM supports both Theater Missile Defense and National Missile Defense programs.

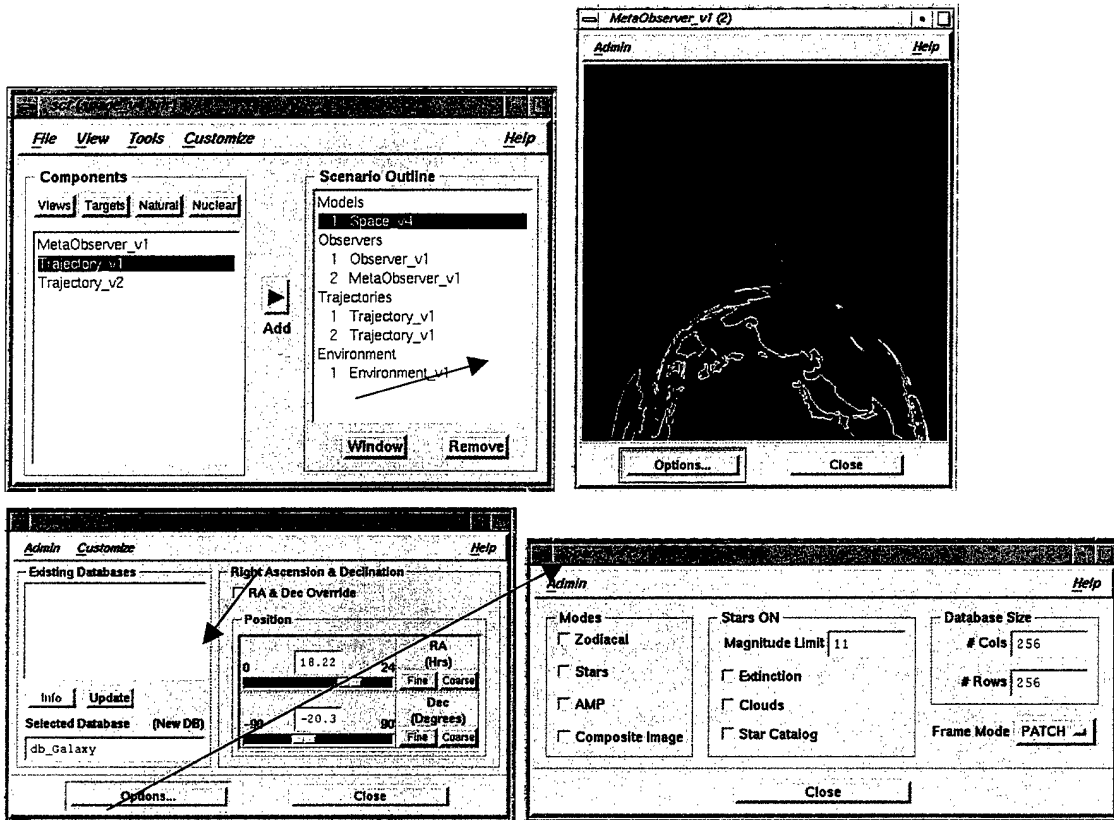


**Figure 1: SSGM '99 Scenario Construction Tool (SCT) Main Window.** This window shows the ease with which the SSGM user can incorporate the CBSD modeling into a scenario that integrates space clutter with other clutter sources and targets. The SSGM user sets the FOV, bandpass, geographic locations, date, GMT, and parameters common to all components in separate screens. When the user selects the space component, the Right Ascension and Declination are set to the FOV already established; however, the user may overwrite this value. The user can select or deselect the various CBSD models and input a very minimal number of variable values. The option of patch mode or movie mode allows the user to save computation time and pan across a large space "patch" or create separate model runs for each frame to model dynamic space clutter such as the motions of solar system bodies. One or more meta-observers can be included in the SSGM scenario to allow the user to interactively visualize the scenario. The gray box shows the location corresponding to the space component output. Lines depict the sensor FOV.

The suite of CBSD models are used to create the SSGM space component. The space component acts as an interface between the CBSD codes and SSGM by performing the output synthesis, image rotations, and other data reformatting to produce output consistent with SSGM conventions. SSGM synthesizes the space component output with other background and target model outputs. Figure 2 depicts the graphic nature of running SSGM '99.

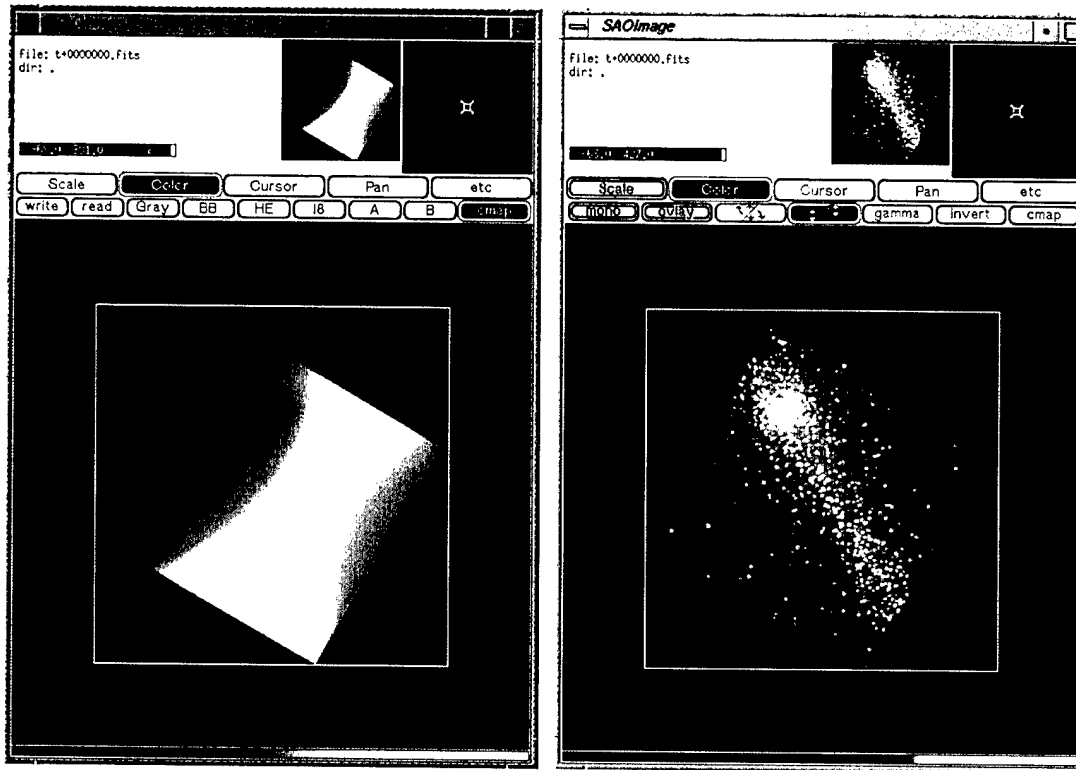


**Figure 2: SSGM '99 Space Component Output.** The image on the left is the scenario run with only zodiacal light included. The image on the right is the output of the space component resampled to the SSGM FOV. Included are the CBSKY4, CBAMP and CBZODY components. Each image has been independently stretched between minimum and maximum value.

### 3.2 PLEXUS

PLEXUS is a user friendly, expert system assisted, GUI enhanced software suite of sophisticated models developed by the Air Force to determine the effects of the atmosphere on Electro-optic sensor performance. PLEXUS has over 300 users in the Electro-Optical community, and is widely accepted as one of the key E-O engineering support tools within the DOD. PLEXUS has been adopted as a teaching tool at the U.S. Air Force Academy, the Engineering Physics Department of the Air Force Institute of Technology (AFIT), and the U.S. Naval Postgraduate School.

The atmospheric definition interface walks the user through several screens to set up the target/sensor/background geometry, location of the target scenario, time of day, season, solar-geophysical environmental parameters, and atmospheric boundary layer and aerosol inputs required to run the required EO effects model(s). The Plexus Expert System is based on the

NASA C Language Integrated Production System (CLIPS) which is Government developed and owned. This allows it to be distributed without license and at no cost.

Figure 3, 4, and 5 demonstrate the usage of PLEXUS and the CBSD modules.

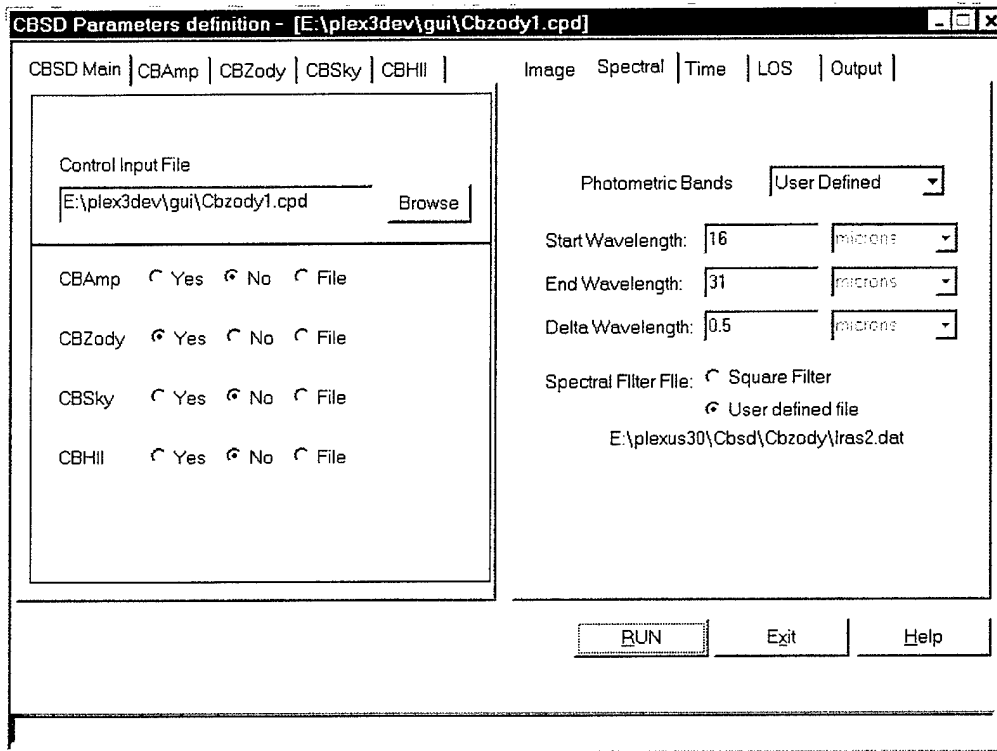


**Figure 3: Selection of components.** The PLEXUS interface allows the user to select which of the codes are to be included in the simulation. The user has the option of running the code through PLEXUS or using a previously run simulation. Additional parameters are easily input such as the spectral, time, image, and output parameters.

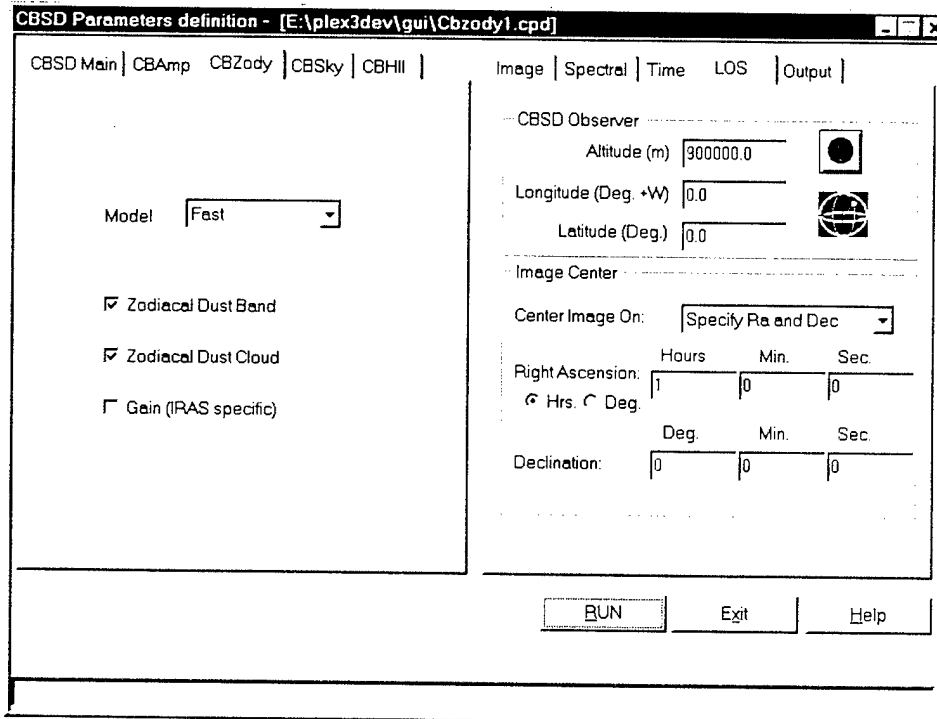


**Figure 4: CBSD module specification.** The user has control over the action of specific modules. Most of the inputs that the text based user has are available to the PLEXUS user. However, the PLEXUS system does limit the user to gnomonic projection images.

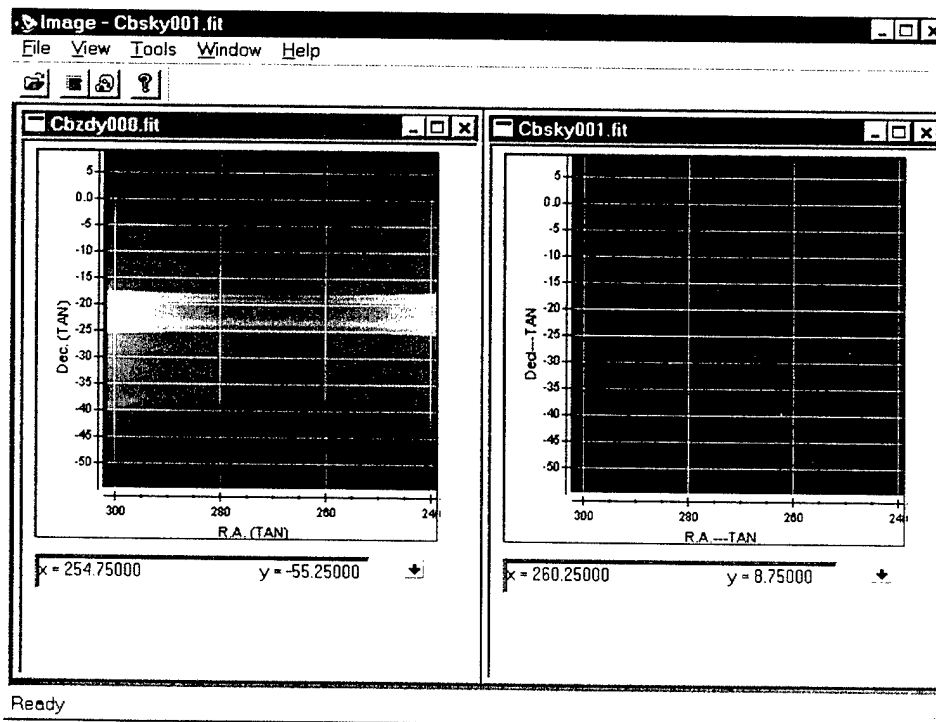


**Figure 5: PLEXUS output.** In addition to the input GUI, the PLEXUS system has an output viewer. Here two images, one from CBZODY6 and one from CBSKY4 are shown.

## **4 CBSD Data Products**

### **4.1 The Major Components of the Celestial Background**

The infrared celestial background may be divided into four major components for analysis and modeling purposes. These categories are:

- Moving Solar System Objects.
- Zodiacal Dust in the Solar System
- Galactic Point Sources
- Spatially Structured Sources of Emission

Each of these categories is phenomenologically different from the others. Each will have a different impact on surveillance systems and each must be treated differently by the CBSD.

### **4.2 Moving Solar System Objects - CBAMP**

Moving objects in the solar system and granularity in the zodiacal background create a temporally and spatially varying form of clutter. If, as is very likely, there is zodiacal granularity due to inhomogeneous distributions of dust in the asteroid belt, then systems will detect a parallax for this component and the phenomenon will vary with aspect and time of observation.

Asteroids, comets and remnants of cometary dust trails constitute non-inertial targets with effective temperatures of 160-260K. IRAS had roughly 15,000 asteroid detections representing 2,500 different asteroids, as well as several score unexpected cometary dust trails. The planets (and their satellites) are moving objects known to be bright in the infrared.

The solar system model, CBAMP, produces images of the solar system objects. These include the Sun, the Moon, the planets, the four brightest moons of Jupiter, and approximately 12,000 of the so called numbered asteroids and an additional 12,000 unnumbered asteroids. For the Sun, Moon, and planets the positional accuracy is better than 2 seconds of arc and in many cases to better than 0.1 second of arc.

The asteroid databases are the set of osculating elements. The osculating elements provide an elliptic orbit prediction for objects that are heavily perturbed by any nearby planet (mainly Jupiter). To improve accuracy, the osculating elements are defined for only a 200-day interval. The sets of osculating elements in CBSD span the years 1970 to 2010. The well-known asteroids thus have a positional accuracy to better than 4 seconds of arc for the years 1970 to 2010.

The flux from all solar system objects is composed of two components, thermal emission and scattered sunlight. In addition to the image generation capabilities, CBAMP has several tabular operational modes for the production of asteroidal ephemerides or for searching a region of the sky for asteroids that meet certain criteria.

The CBAMP code uses the NASA/JPL DE/LE-405 database of planetary positions. The JPL database gives the heliocentric, rectangular coordinates of all the planets, the Earth, the Sun, and the Moon. The values are used by CBAMP to calculate the positions on the sky as seen by an observer. The ephemeris covers the years starting at 1600 and ending at 2200. Figure 6 is an

interesting test of CBAMP. It shows a night in December 1612 around the time Galileo is now known to have observed, but not recognized as a planet, the planet Neptune.

Other CBSD Technical reports relevant to CBAMP are:

SIMPS Software Final Report

SIMPS User Manual

CBAMP: Technical Reference Manual

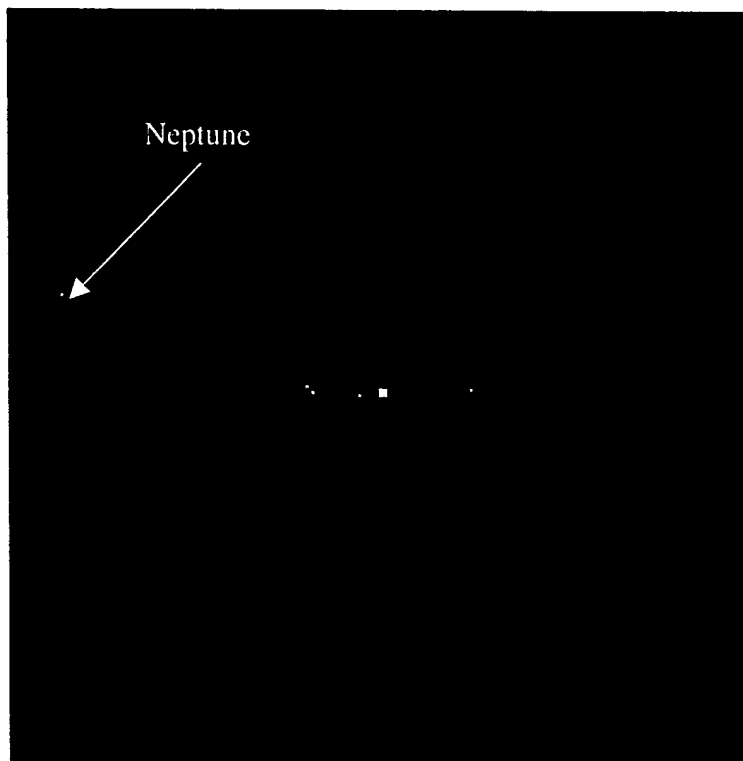


**Figure 6:** This image shows **Jupiter (center)** surrounded by the **four Galilean staellites**. The image represents a night in December 1612 that Galileo is now known to have observed Neptune (left).

### 4.3 The Diffuse Zodiacal Background - CBZODY

The diffuse zodiacal background, arising from both scattering and thermal re-emission of sunlight by dust in the solar system, provides the ultimate limiting background for system performance. Because the Earth is immersed in the zodiacal dust cloud close to the ecliptic plane, the zodiacal background is pervasive and detectable at all viewing angles by any Earth-orbiting sensor. There are also distinct bands of zodiacal dust, arising from relatively recent collisions between large asteroids in the main asteroid belt, circling the sky close to  $i=0$  on the ecliptic plane.

Photon noise from the zodiacal emission begins to dominate other sources of detector noise above an irradiance of  $\sim 10^{-10}$  Watt/cm<sup>2</sup>/μm/sr in an instrument with detectors sized to the diffraction limit of the optics and a  $10^{-17}$  Watt/Hz<sup>-1/2</sup> detector Noise Equivalent Photons. Such a

brightness level is reached for viewing angles less than 40-50° from the sun. Very few measurements have been made outside the solar elongation angle range of 60° -120°. A model **must** be relied upon to get continuous descriptions of the zodiacal background.

The solar system dust cloud, also known as the zodiacal dust, is seen as thermal emission over all the sky and dominates the diffuse IR emission over most of the 4 - 35μm waveband. Below 4μm, scattered sunlight becomes an important contributor to the background. The zodiacal dust is made up of two observable structures, the broad emission and the band structure. The broad emission is that component seen over the entire sky, and is strongest close to the plane of the ecliptic (Sykes 1988, 1990). It is theorized that a toroidal dust cloud, composed of debris from asteroid collisions and comets, encircles the Sun (Dermott et al., 1984). The Earth is located inside this cloud and hence the cloud is visible over the entire sky.

The band structure, discovered by IRAS (Low et al. 1984, Hauser et al. 1984), consists of several pairs of faint bands of emission close to the plane of the ecliptic associated with the remnants of the breakup of individual asteroid families (Sykes et al., 1989, Dermott et al. 1985, 1986). The CBSD zodiacal light model, CBZODY, models both the broad and band contributions, including thermal emission and scattered light, and is capable of producing spectra, line-of-sight radiance, and two-dimensional images. Future developments promise extensions to the ultraviolet and an improved band structure based on the orbital inflow of dust from asteroid breakups.

Over the course of its development, CBZODY has been continuously improved through the comparison of the model to observational data of the zodiacal emissions by some of the premier DoD and astronomical research community research programs. Along with improvements to the realism of its simulated results, CBZODY has also been improved with regard to computational speed, thus making it a candidate for application in complex wargaming and operations research simulations for ballistic missile defense. Figure 7 is one example of CBZODY's capability.

Other CBSD Technical Reports relevant to CBZODY are:

CBZODY6 Validation Report

CBZODY Technical Reference Manual



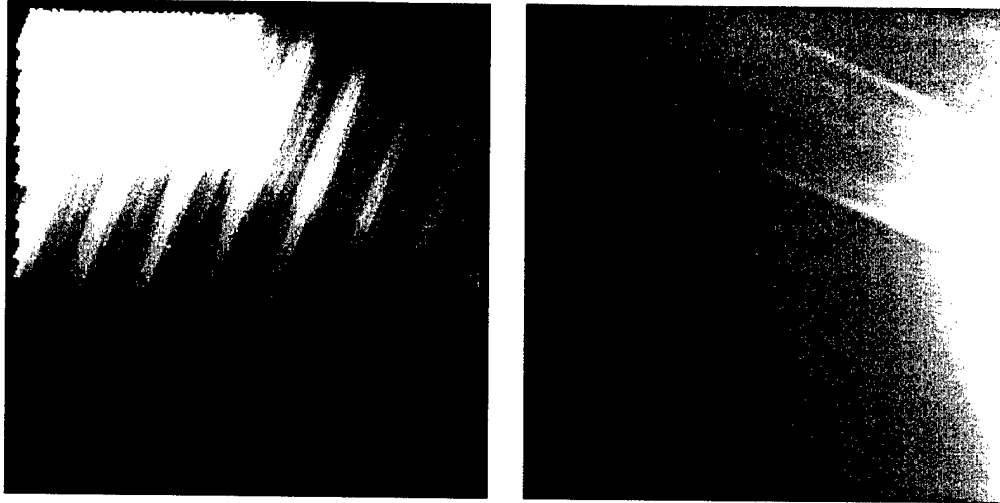


**Figure 7: Comparison of CBZODY model with IRAS data.** IRAS SkyFlux plate (left) of the region  $1^{\text{h}}$  and  $0^{\circ}$ . CBZODY model output (right) of the same region. The striping from upper right to lower left is detector noise. The faint, nearly horizontal line, near the bottom of the image is the dust trail of Comet Temple-2

#### 4.4 The Galactic Point Source Background - CBSKY

The galactic point source background is dominated by stars and those HII regions, molecular clouds, and external galaxies so distant as to be effectively point sources at system-specified resolution. The distribution of infrared point sources is neither uniform across the sky nor random in a specified region. At a sensitivity of  $10^{-20}$  watt/cm<sup>2</sup>/μm, the number of point sources above detection threshold can be thousands per square degree along the galactic plane.

Such high densities will impact on-board satellite data processing. Since these high densities are mainly confined to specific regions, a possible solution is to avoid all areas that have densities greater than the data processing can handle. However, even the extent of those areas above a given threshold is uncertain in the data, bounded only by the confusion limit of the IRAS survey at  $>25$  sources/deg<sup>2</sup>.

The emissions from stellar point sources represent the most important source of clutter in the celestial background. Most infrared point source models use observational data, principally the IRAS (the Infrared Astronomical Satellite) catalog of point sources. Even though the IRAS catalog contains 246,000 objects, it has limited spectral coverage (the entire sky was sampled at only 12 and 25μm within the 0.1 - 35μm region). IRAS had a large pixel size limiting the flux of individual sources and undersampling the star count in the densest part of the sky, the galactic plane.

The Two Micron All Sky Survey (2MASS) second release is now available. Covering approximately 35% of the sky, the 2MASS survey will, by 2002, map the entire sky at 2μm.

To provide realistic star counts over the entire sky, the Air Force Phillips Laboratory, Geophysics Directorate sponsored the development of the SKY model. The SKY model provides a single line-of-sight statistical distribution of the number of point sources per unit angular area per magnitude interval for each of 87 spectral classes (Cohen 1993, 1994a).

The CBSD galactic point source model CBSKY4 is based on the SKY4 model of Wainscoat et al. (1992) and Cohen (1993, 1994a, 1994b). CBSKY4 not only produces images over any part of the sky down to 24<sup>th</sup> magnitude (the SKY4 limit), it also provides smoothing algorithms and other enhancements to increase the realism of a point source scene.

Based on a finite element approach (Schewchuk 1996), the entire sky is gridded into evaluation triangles of varying sizes. The size of an evaluation triangle is inversely proportional to the stellar density. Hence, at the galactic center, very many small triangular elements exist. Near the poles, however, only a few large triangles have been defined.

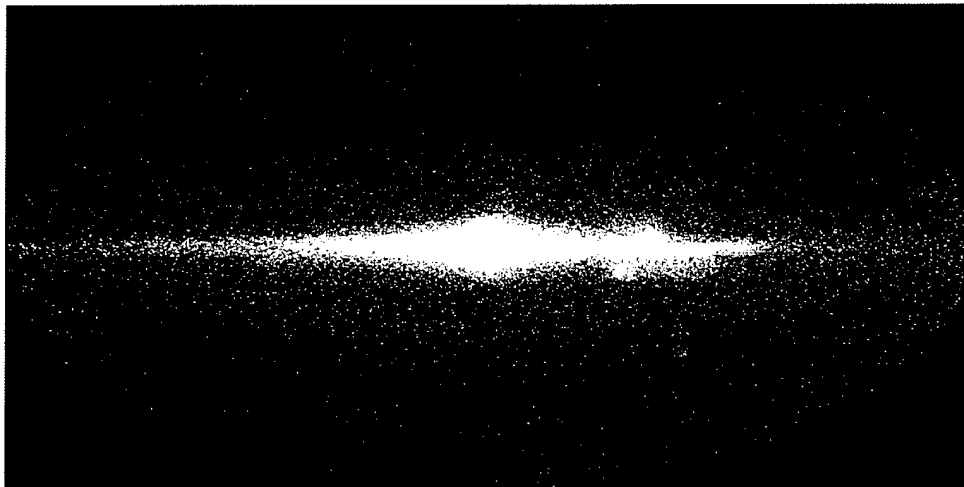
To add to the realism of produced scenes, catalog stars have been added. In the infrared, 2503 IRAS and 49 MSX stars, down to 0<sup>th</sup> magnitude at 12 $\mu$ m, have been included with a spectral template assignment. In the visible, the Yale Bright Star Catalog of over 9000 objects has similarly been assigned a spectral template. Finally, the CBSD point source model includes an estimate of the interstellar extinction, an important consideration for short wavelength studies.

Figure 8 shows the entire sky at 12 $\mu$ m.

Other CBSD Technical reports relevant to CBSKY are:

CBSKY4 Validation Report

CBSKY4 Technical Reference Manual



**Figure 8: A 12 $\mu$ m all sky image with molecular clouds.** Rho Oph is visible above the galactic center. The Large Magellanic Cloud (LMC) is visible in the lower right. Above the LMC enhanced regions are clearly visible.

## 4.5 Spatially Structured Sources of Emission

### 4.5.1 HII regions - CBHII

The HII regions are large clouds of interstellar matter excited and ionized by ultraviolet photons from hot O and B (earlier than B3) stars. Many HII regions exist, but most do not

exhibit extended structure at the resolutions required by CBSD. These unresolved HII regions are handled by the point source model CBSKY. The extended HII regions are modeled individually. The CBSD HII regions model, CBHII, contains ~2000 distinct HII regions. Each is modeled by a disk with a Gaussian fall off, and simple spectra derived from the IRAS Low Resolution Spectrograph (LRS) as defined in the SKY4 spectral template database. Figure 9 shows the distribution of HII regions near the galactic center.

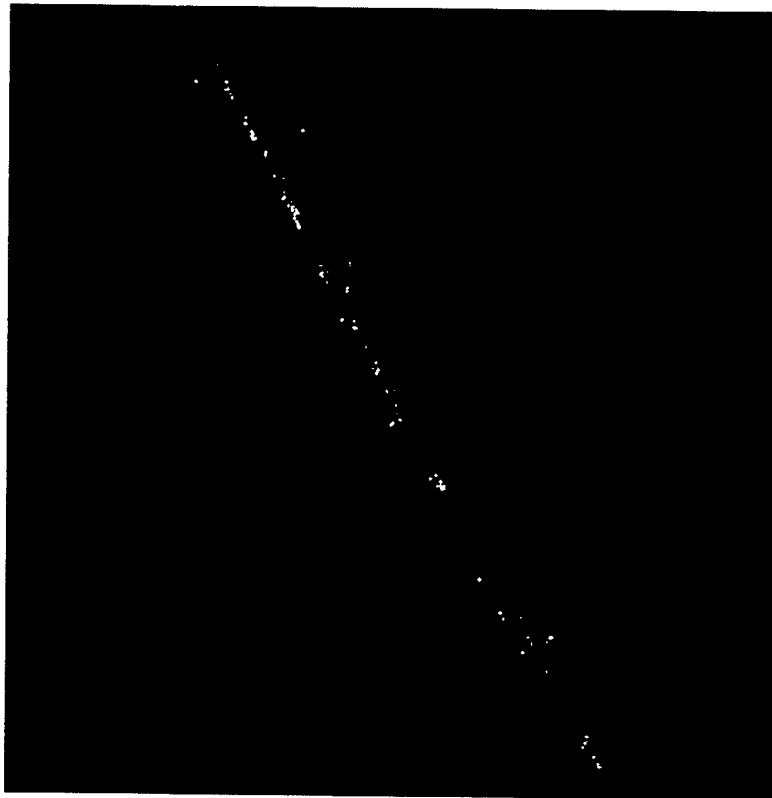


**Figure 9:** An image looking toward the galactic center showing the distribution of HII sources. Centered on the galactic center in equatorial coordinates the distribution of HII regions follows the plane of the galaxy.

#### 4.5.2 Infrared Cirrus - CBCIRRUS

The existence of "infrared cirrus," whose all-pervasive nature was first observed by IRAS, is now quite widely known. Although rather faint at wavelengths shorter than  $\sim 25\text{-}30\mu\text{m}$ , the cirrus is, nevertheless, the most morphologically spectacular spatially structured source of emission. Because intensive studies of the cirrus have only begun to be undertaken during the past few years, neither the underlying phenomenology nor the morphology is yet well enough understood to be reliably modeled.

The CBCIRRUS model will simulate the contribution to the celestial background due the galactic dust known as the Galactic Cirrus. The Cirrus is a tenuous dust veil that is prevalent over the entire sky at wavelengths longer than 25 microns. At shorter wavelengths the Galactic

Cirrus is masked by the more dominant Zodiacal dust (12 microns) and the galactic stars (visible to near infrared).

#### 4.6 The CBSD Suite of Astronomical Codes – CBSD4

The CBSD codes are described as a suite since there are four physically independent modules that are encapsulated into a single unit by use of a control program. The control program (CBSD4) allows a single interface to all of the physical modules providing a consistent set of input parameters. The resultant module outputs are then synthesized into a single scene (Figure 10).

Other CBSD Technical reports relevant to CBSD4 are:

CBSD User's Manual

CBSD4 User's Manual

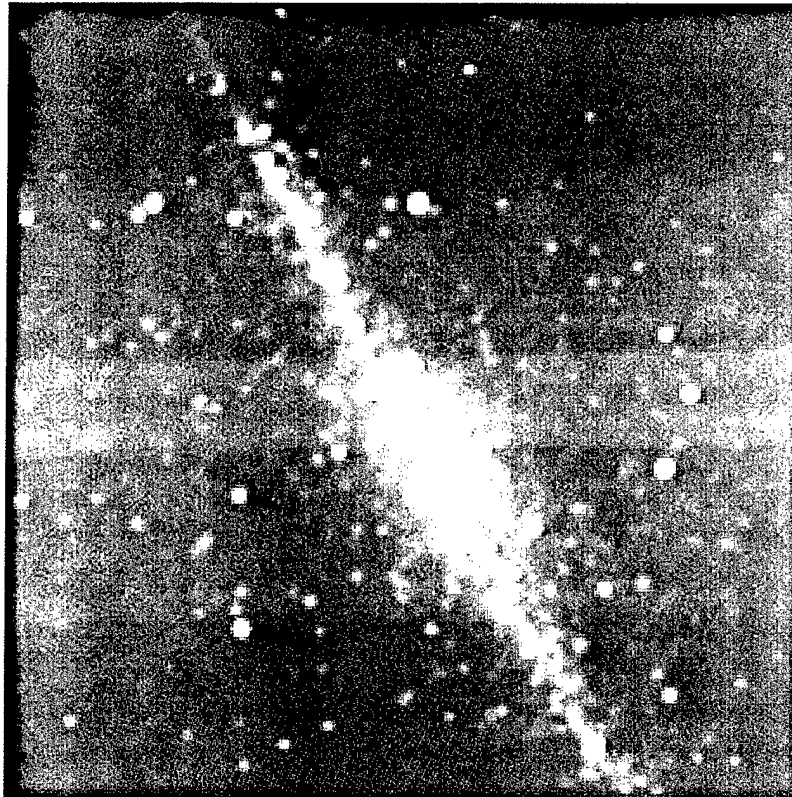


**Figure 10: The galactic center with all components.** In addition, a point –spread function was employed to simulate the instrumental smearing of optical systems.

The CBSD codes are also capable of visible light imaging. Figure 11 shows an image taken on the evening of 5 April 1997 by Marco Fulle from the 750m mark on the volcanic island of Mt. Stromboli off the coast Sicily. The 3-minute photograph shown has appeared in the January 2001 issue of Sky & Telescope. The image has several components:

- Twilight is visible as the bright yellow band.
- Just above the twilight, bottom left of center, is the planet Mercury
- The stars are visible with the Pleiades prominent near the top left of center
- Comet Hale-Bopp is very noticeable to the right of center
- The zodiacal light is visible above the twilight

Figure 12 shows our effort to recreate this image using the components of CBSD and the Air Force Research Laboratory's atmospheric model MODTRAN. The creation of the image took several steps. Since this is a horizon image, atmospheric attenuation is an important factor. Also, the sky radiance from twilight was included. The three band composite image also includes the effects of the photographic film. This image is discussed further in the CBZODY6 Validation Report.



**Figure 11: Image of the zodiacal light taken from Mt. Stromboli by Marco Fulle (used with permission).** On the evening of 5 April 1997 Marco Fulle took an image of the zodiacal light seen stretching from the horizon to the Pleiades. (© Marco Fulle, 1997, used with permission.)

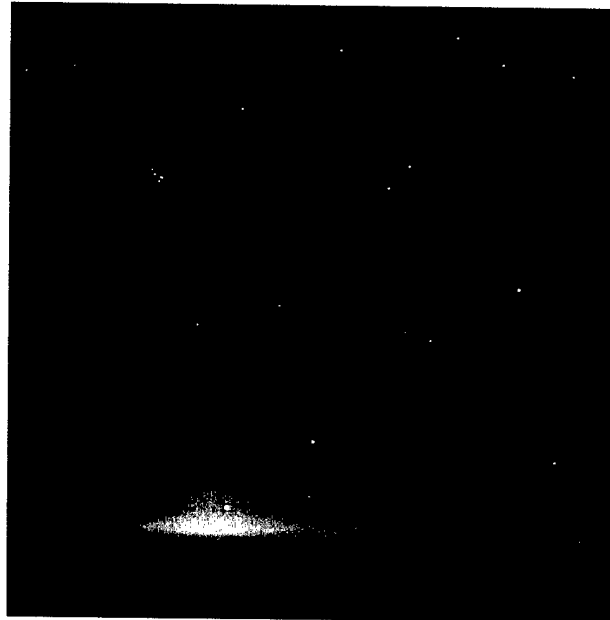


**Figure 12: A CBSD and MODTRAN view of the same region as Figure 11.** Uncertainties in the low light level film responses account for most of the differences between the images.

## 5 Summary

The Air Force's CBSD suite of models describes the astronomical sky in the region 0.1 to 35 $\mu$ m and beyond. Designed for sensor development efforts in support of target detection and discrimination, the CBSD codes provide modeling capabilities based on a solid physical background. The CBSD codes are not only good sensor models, they are good science.

With a positional accuracy to 2 arc-seconds and a flux accuracy to better than 10%, the CBSD can be developed into teaching tools at the graduate school level.

Several data sets are now available that will be incorporated into future versions of CBSD. The Two Micron All Sky Survey (2MASS) has recently released its data and will be incorporated into future versions of CBSD. MSX data will aid in improving the CBZODY model beyond the 60 –120  $\mu$ m range.

Project Stardust is scheduled to rendezvous with Comet Wild-2 in 2004 and return cometary samples to Earth in 2006. This will be extremely beneficial to the CBZODY in defining a zodiacal dust composition.

The SIRTf mission, scheduled for launch in December 2001, is the next cryogenically cooled space observatory. SIRTf will return a wealth of information on stars, galactic dust, and solar system objects. These data will enhance the CBSD model with information on small-scale structures, time variability, and composition.

New asteroids are being added at nearly 1000 per month. Rather than rely on osculating elements, it would be beneficial to include a perturbation model for accurate asteroid positions. Additionally, asteroids are treated as spherical, non-varying objects. Asteroids are anything but spherical. They provide a time dependent light source that could momentarily confuse target detection systems. Providing a time varying asteroid light curve will aid in discriminating these rapidly moving sources.

While strides have been made to increase the execution speed of CBSD, two factors have changed. The speed of the average processor has increased markedly since the beginning of the program. At the same time, the complexity and expectations of the components have increased. To be included into real-time war-gaming scenarios, future developments of CBSD will have to stress efficiency while maintaining fidelity.

With all of their accomplishments, much work remains to be done on the CBSD models.

## References

- Cohen, M. (1993). "A Model of the 2-35  $\mu\text{m}$  Point Source Infrared Sky," *Astron. J.*, **105**, 1860.
- Cohen, M. (1994a). "Powerful Model for the Point Source Sky: Far-Ultraviolet and Enhanced Midrange Performance," *Astron. J.*, **107**, 1993.
- Cohen, M. (1994b). "A Powerful New Model for the Point Source Sky," *Astron. & Space Sci.*, **217**, 181.
- Dermott, S. F., P. D. Nicholson, J. A. Burns, and J. R. Houck. (1984). "Origin of the Solar System Dust Bands Discovered by IRAS," *Nature*, **312**, 505.
- Dermott, S.F., P. D. Nicholson, J. A. Burns and J. R. Houck. (1985). "Properties and Interaction of Interplanetary Dust," in IAU Colloquium #85, (eds. R. H. Giese and P. Lamy) (D. Reidel Pub. Co.) p395.
- Dermott, S.F., P. D. Nicholson, and B. Wolven. (1986). "Preliminary Analysis of the IRAS Solar System Dust Data," in *Asteroids, Comets and Meteors, II* (eds. C-I. Lagerkvist and H. Rickman), Uppsala, p583.
- Hauser, M. G.; Gillett, F. C.; Low, F. J.; Gautier, T. N.; Beichman, C. A.; Aumann, H. H.; Neugebauer, G.; Baud, B.; Boggess, N.; Emerson, J. P. (1984). "IRAS Observations of the Diffuse Infrared Background," *Astrophys. J.*, **278**, L15-L18.
- Low, F. J.; Young, E.; Beintema, D. A.; Gautier, T. N.; Beichman, C. A.; Aumann, H. H.; Gillett, F. C.; Neugebauer, G.; Boggess, N.; Emerson, J. P. (1984). "Infrared Cirrus - New Components of the Extended Infrared Emission," *Astrophys. J.*, **278**, L19-L22.
- Shewchuk, R. J. (1996). "Triangle: Engineering a 2D Quality Mesh Generator and Delaunay Triangulator," *First Workshop on Applied Computational Geometry, ACM, May 1996*.
- Sykes, M. V. (1988). "IRAS Observations of Extended Zodiacal Structures," *Astrophys. J.*, **334**, L55.
- Sykes, M. V. (1990). "Zodiacal Dust Bands - Their Relation to Asteroid Families," *Icarus*, **85**, 267.
- Sykes, M. V., Greenberg, R., Dermott, S. F., Nicholson, P. D., Burns, J. A., and Gautier, T. N. (1989). "Dust Bands in the Asteroid Belt," in *Asteroids II*, eds. R. P. Binzel, T. Gehrels, and M. S. Matthews, (Tucson: U. of Arizona), p.336.
- Wainscoat, R.J, M. Cohen, K. Vold, H. J. Walker, and D. E. Schwartz (1992). "A Model of the 8-25 Micron Point Source Infrared Sky," *Astrophys. J. Supp.*, **83**, 111.

## **Appendix A: CBZODY6 Validation Summary**

### **A.1 Introduction**

This report provides detailed information on the evolving improvements and verification of the AFRL/HRS Celestial Background Scene Descriptor (CBSD) Zodiacal Emission code (CBZODY).

The CBZODY model predicts the flux from the solar system dust cloud for a given line-of-sight or field-of-view that would be detected by optical and infrared sensor systems. CBZODY is currently in use by the MDA as a component of the SSGM simulation package and as part of the AFRL PLEXUS R3V2 atmospheric effects modeling suite.

The intent of the report is to document the quality and fidelity of this component in its application to the design, simulation, and operation of MDA electro-optic sensors having to discriminate targets against zodiacal light and dust band emission sources. This report provides insight into the goodness of the CBZODY model relative to actual observations of the zodiacal background light/emission sources. This report captures the base-line that should ensure system, designers, developers, and operators that CBZODY gives fast, reliable, and realistic representation of the effects of Zodiacal emission sources on E-O systems.

#### **A.1.1 Goals of the CBZODY Program**

The CBSD CBZODY program has the stated goal of reproducing the zodiacal contribution to the celestial background with both a high spectral and spatial fidelity. Spectrally the code must have what we call "dial-a-wavelength" capability over a range of 0.2 to 35 $\mu$ m. This means that the code accepts any spectral filter function in that range. The CBZODY code, by use of the external volume emissivity database, can produce high spectral resolution spectra from 0.2 to 30 $\mu$ m at 0.01 $\mu$ m resolution. It can also reach 300 $\mu$ m with a spectral resolution of 0.1 $\mu$ m.

More importantly, the dial-a-wavelength capability requires the code to be predictive. It does not merely mimic the best-fit results of a certain instrument database.

The second goal is to allow model simulations down to the 2 arc-second level. The CBZODY model is capable of producing such simulations. We do caution however that we can not quote an accuracy for this level of observations. The primary reason is that there are no large scale observations of zodiacal light at a 2 arc-second resolution. This is inherently difficult because of the nature of the zodiacal emission. The zodiacal light is an all-sky phenomenon. The observed brightness in a sensor IFOV is dependent on the IFOV of the sensing element, i.e. the pixel size. The surface brightness of the zodiacal emission is much lower by orders of magnitude than the surface brightness of any star. However, unlike stars, which are mere points, the zodiacal emission completely fills the IFOV. Larger pixels means that more area is sampled and the total, or integrated brightness, can exceed not merely stars but the plane of the galaxy itself.

#### **A.1.2 About Zodiacal Light.**

The solar system, or zodiacal, dust cloud, is seen in thermal emission from 4 $\mu$ m to 35+ $\mu$ m and by scattered sunlight at  $\lambda < 4\mu$ m. This background has two large-scale components:



a broad component whose brightness fills the sky around the Earth; and a narrower band structure confined to within a few tens of degrees of the ecliptic plane (Sykes 1988, 1990). It is theorized that a toroidal dust cloud, composed of debris from asteroid collisions and comets, encircles the Sun (Dermott et al., 1984). The Earth is located inside this cloud and hence the cloud is visible over the entire sky.

The band structure, discovered by IRAS (Low et al. 1984, Hauser et al. 1984), consists of several pairs of faint bands of emission close to the plane of the ecliptic associated with the remnants of the breakup of individual asteroid families (Sykes et al., 1989, Dermott et al. 1985, 1986). The CBSD zodiacal light model, CBZODY, models both the broad and band contributions, including thermal emission and scattered light, and is capable of producing spectra, line-of-sight radiance, and two-dimensional images.

Over the course of its development, CBZODY has been continuously improved through the comparison of the model to observational data of the zodiacal emissions by some of the premier DoD and astronomical research community research programs. Along with improvements to the realism of its simulated results, CBZODY has also been improved with regard to computational speed, thus making it a candidate for application in complex wargaming and operations research simulations for ballistic missile defense.

## A.2 CBZODY: a Zodiacal Light Model.

We have developed a detailed model of the zodiacal emission. The code is called CBZODY6 and was developed for the Air Force's CBSD program whose goal is to provide realistic simulations of the celestial sphere to be used in sensor simulation and development. Following the method of Leinert (1975), the zodiacal dust cloud is separated into two components, a radial dust density function and a latitudinal, or out-of-plane, dust density component. The cloud is assumed symmetric longitudinally ( $l$ ), in the dust cloud symmetry plane, which is close to but not coincident with the ecliptic. Formally, the number density function is defined in heliocentric ecliptic coordinates as:

$$N(d, \beta) = f(d) \cdot f(\beta)$$

$d$  = heliocentric distance

$\beta$  = heliocentric ecliptic latitude

The in-plane or radial function is simply:

$$f(d) = d^{-\nu}$$

On theoretical grounds, the power law index,  $\nu$ , should be 1 (Briggs 1962). This is light drag due to the Poynting-Robertson effect. The model uses a Lorentzian-like function for the out-of-plane, latitudinal distribution (Clark et al. 1993) of the form:

$$f(\beta) = \left( \frac{\Gamma^2}{\Gamma^2 + \tan^2 \beta} \right)$$

where  $\Gamma$  is the half-width-at-half-maximum (HWHM) of the cloud, also known as the scale height. We also note the scale height can be related to an angular measure by:

$$\Gamma = \tan \beta_0$$

The Lorentzian function was used after studying the IRAS survey scan data. Figure A-1 is a scan from the IRAS mission (solid line) plus a model run (dashed line) using a Lorentzian profile. There are three things to note about this image:

1. Between ecliptic latitudes of  $-30^\circ$  to  $-60^\circ$  there is a weak contribution to overall signal from the galaxy
2. Between  $-20^\circ$  and  $20^\circ$  there is an excess not modeled by the Lorentzian; these are the zodiacal bands first observed by IRAS in 1983 (Low et al. 1984, Hauser et al. 1984)
3. The Lorentzian produces an excellent fit to the remaining observed flux.

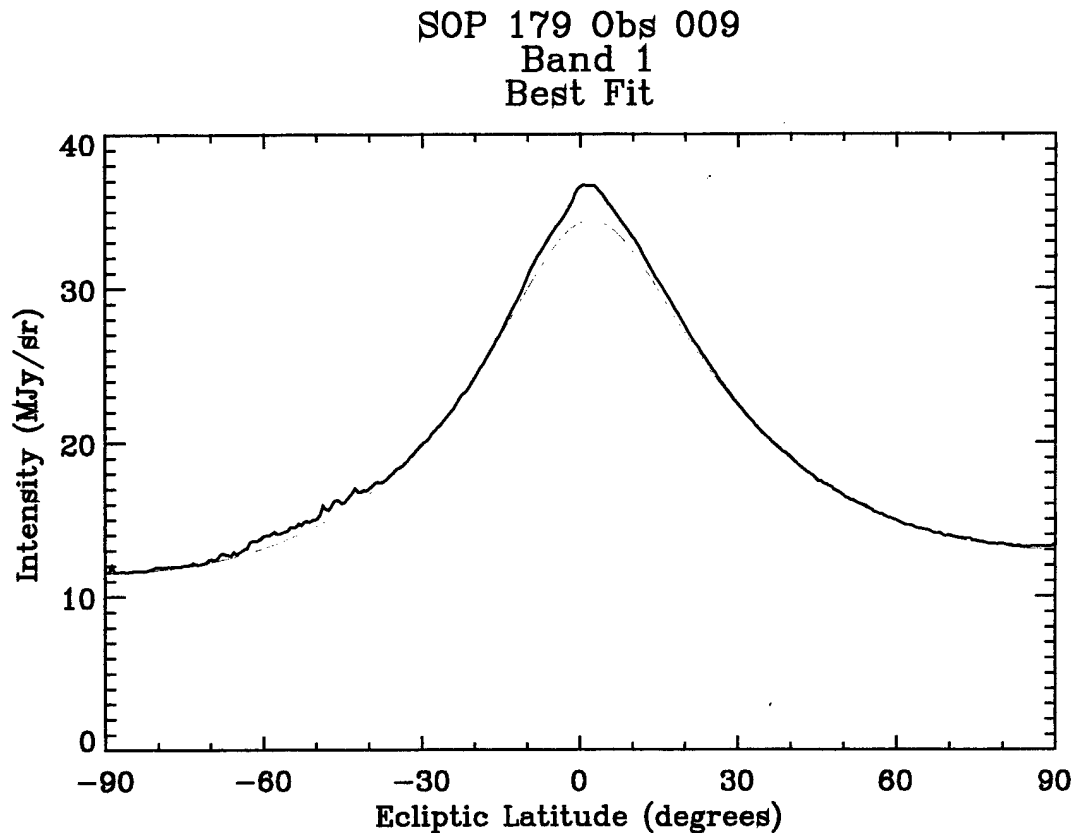


**Figure A-1: IRAS data and the Lorentzian fit.** The IRAS data are presented as a solid line while the Lorentzian model is the dashed line. The match between the data and model is excellent once the galactic and band contributions are ignored.

### A.3 Dust Composition and Volume Emissivity

While the main component of the spatial modeling of the CBZODY model is the Lorentzian out-of-plane dust density model, there is an equally important component for the spectral modeling. The dust composition is contained in a volume emissivity function.

The volume emissivity,  $\epsilon_\nu$ , is defined as the amount of energy that a unit volume of material emits per second per unit solid angle in the frequency range  $\nu$  to  $\nu + d\nu$  (Lang 1980, p. 27). The total intensity along a line of sight is:

$$I_\nu = \int_0^l \epsilon_\nu \cdot e^{-\alpha_\nu x} dx.$$

where:

$l$  = the line of sight distance to the dust cloud outer limit,

$\alpha_\nu$  = the absorption coefficient per unit length.

The absorption coefficient can also be considered an extinction coefficient and is the combination of the amount of energy absorbed by the dust and the energy scattered out of the line of sight (Gray 1976, p. 106). For the zodiacal light calculations, the absorption is essentially zero and is taken to be identically zero. The volume emissivity of an ensemble of particles is calculated by integrating over the size distribution and summing over all constituents (Reach 1988):

$$\epsilon_\nu = \sum_i \int da \frac{dn^{(i)}}{da} B_\nu(T^{(i)}(a)) Q_{abs}^{(i)}(a, \nu)$$

where the size distribution,  $da \frac{dn^{(i)}}{da}$ , is the number density of particles composed of material  $i$  with radius between  $a$  and  $a+da$ . The solution for the temperature  $T$  is found from the condition of radiative equilibrium

$$T = 278^\circ K \left[ \frac{\bar{Q}_{Sun}}{\bar{Q}(T)} \right]^{1/4} D^{-1/2}$$

where  $\bar{Q}_{Sun}$  is the absorption efficiency averaged over the solar spectrum,  $\bar{Q}(T)$  is the absorption efficiency averaged over a blackbody spectrum at temperature  $T$ , and  $D$  is the distance of the grain from the Sun in AU. The solution for the temperature is usually done by iteration. The absorption efficiency,  $Q_{abs}$ , is defined such that the cross section for absorption of a photon of wavelength  $\lambda$  by a spherical particle of radius  $a$  is  $\pi a^2 Q_{abs}^{(i)}(a, \lambda)$ . The solution for  $Q_{abs}$  is based on Mie theory (Van de Hulst 1957, Kerker 1969, and Bohren and Huffman 1983).

The model of Reach (1988) has a variety of materials that can be used. The volume emissivity used in CBZODY consists of mixtures of astronomical silicates and graphite. Figure A-2 gives the temperature distribution for astronomical silicate as a function of particle size for 3 distances from the Sun: 0.05 AU; 1.00 AU; and 3.30 AU.

The volume emissivity used in CBZODY6 is a mixture of 65% astronomical silicate and 35% graphite and is in a pre-computed external file. Figure A-3 gives the volume emissivity spectra used in CBZODY for three heliocentric distances, 0.05 AU, 1.00 AU, and 3.30 AU. The peak shifts to longer wavelength for increased distance following the temperature profile.

For additional information the reader is directed to *Technical Report 8: Validation Report for the Celestial Background Scene Descriptor (CBSD) Zodiacal Emission (CBZODY6) Model*.

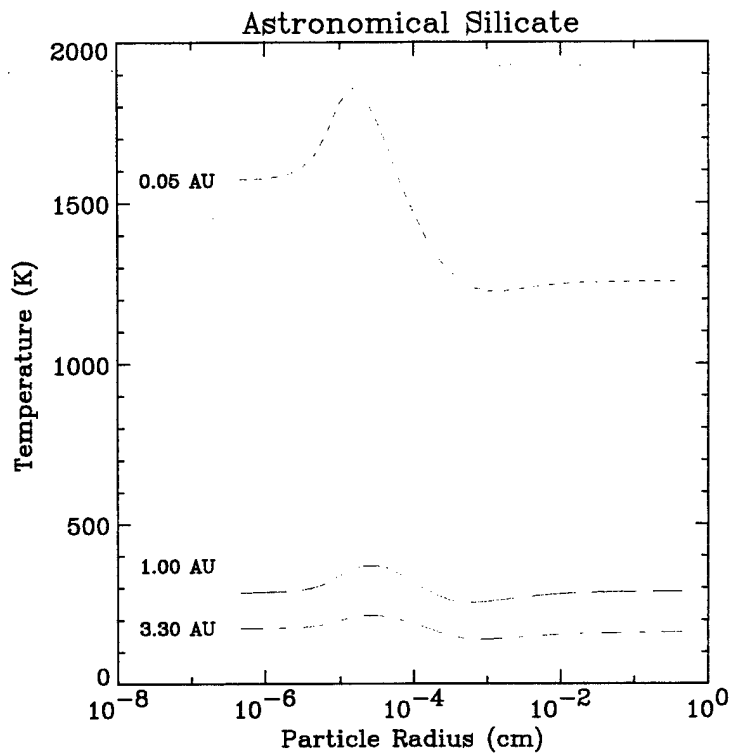
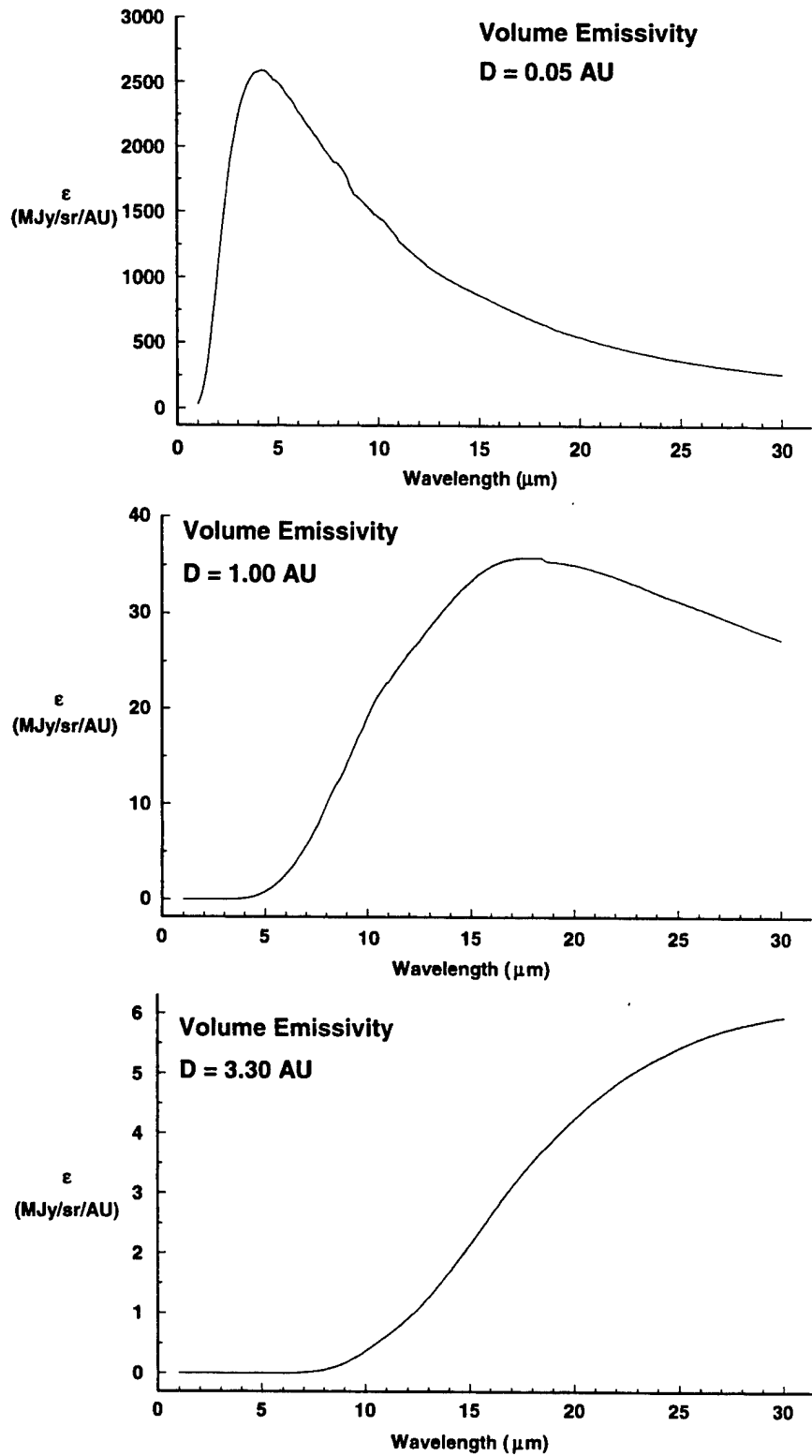


Figure A-2: Temperature profiles for astronomical silicate at three different distances from the Sun as a function of particle size.



**Figure A-3: Volume emissivity.** Astronomical silicate spectra for three different heliocentric distances: top, 0.05 AU; middle, 1.00 AU; and bottom, 3.30 AU.

## **A.4 Validation**

### **A.4.1 Parameter sets**

This section enumerates the final parameter set used in the deployment of the CBZODY6 code. Parameters are defined internally, in data statements, or in the CBZPARMS.DAT file, which was a convenient method of testing new parameters without recompiling the code.

### **A.4.2 CBZPARMS.DAT Parameter set**

Table A-1 shows the current list of parameters in the CBZPARMS.DAT file. While this is an ASCII file, it is not to be edited by the users. These parameters signify the “best fit” to the ensemble of data presented. We have found that by adjusting the parameters it may be possible to improve the fit to a certain dataset, but this tends to worsen the fit to other datasets. These parameters represent our best estimate based on all the tradeoffs between datasets.

Table A-1: Adopted parameters in CBZPARMS.DAT file.

```

nu      -- power index
1.0000000000000000
hwhm1  -- hwhm inner dust plane
0.371
znode1  -- ascending node inner dust plane
83.009
zincl1  -- inclination inner dust plane
3.30
n0thm1  -- Normalization density, inner plane
1.47
n0bnd1  -- Normalization density, bands, inner plane
0.049
break1  -- break point between planes
1.02
hwhm2  -- hwhm middle dust plane
0.281
znode2  -- ascending node middle dust plane
78.256
zincl2  -- inclination middle dust plane
3.30
n0thm2  -- Normalization density, middle plane
1.68
n0bnd2  -- Normalization density, bands, middle plane
0.034
break2  -- break point between planes
4.0000000000000000
hwhm3  -- hwhm outer dust plane
0.2670000000000000
znode3  -- ascending node outer dust plane
67.5400000000000010
zincl3  -- inclination outer dust plane
1.9240000000000000
n0thm3  -- Normalization density, outer plane
1.6050000000000000
n0bnd3  -- Normalization density, bands, outer plane
0.027524312293892
n0a2    -- scattering normalization      0.0070
6.58e-13
albedo  -- dust albedo
0.3000000000000000
offset  -- DC offset
0.0000000000000000
sigma   -- time constant
250.00000000000000
fscale  -- scale factor
0.0000000000000000
again   -- zero point gain
1.0000000000000000
ring_nrm -- leading and trailing ring Normilization density
0.0000000000000000      0.0000000000000000
ring_ang -- leading and trailing ring-Earth separation (deg)
2.0907000000000000      4.4800000000000000
ring_wl  -- leading ring characteristic widths (AU)
0.3542310000000000      0.0187120000000000      0.0744980000000000
ring_wt  -- trailing ring characteristic widths (AU)
0.0097250000000000      0.0154770000000000      0.0092840000000000
n0band  -- band parameters
0.50000  0.20000  0.35000  0.75000  0.65000  0.30000  0.24000
n0bndsct -- band scattering
1.0e-15

```

### A.4.3 Band parameters

The final set of migrating band parameters used for the model validation is presented in Table A-2. Figure A-4 gives the latitudinal profiles of the dust associated with the 7 asteroid families.

Table A-2: Modified migrating band parameters.

Parameter	Themis	Koronis	Nysa	Flora	Eos	Eunomia	Maria
$i_{\text{latitudinal}}^1$	1.209	1.855	2.695	4.457	8.612	11.613	13.986
$i_{\text{orbital}}^2$	0.82	0.82	0.82	0.76	0.76	0.76	0.76
$n_0$	0.50	0.20	0.35	0.75	0.65	0.30	0.24
$\delta_\zeta$	1.219	1.978	2.624	3.570	9.184	12.388	14.905
$v_i$	1.272	0.316	1.480	2.132	0.436	0.376	0.200
$p_i$	4	4	4	4	4	4	4
$R_0$ (AU)	3	3	3	3	3	3	3
$\Omega$	86°	86°	86°	92°	92°	92°	92°

<sup>1</sup> the latitudinal inclination is the observed displacement from the ecliptic plane in the sky.

<sup>2</sup> the orbital inclination is the orbit's tilt.

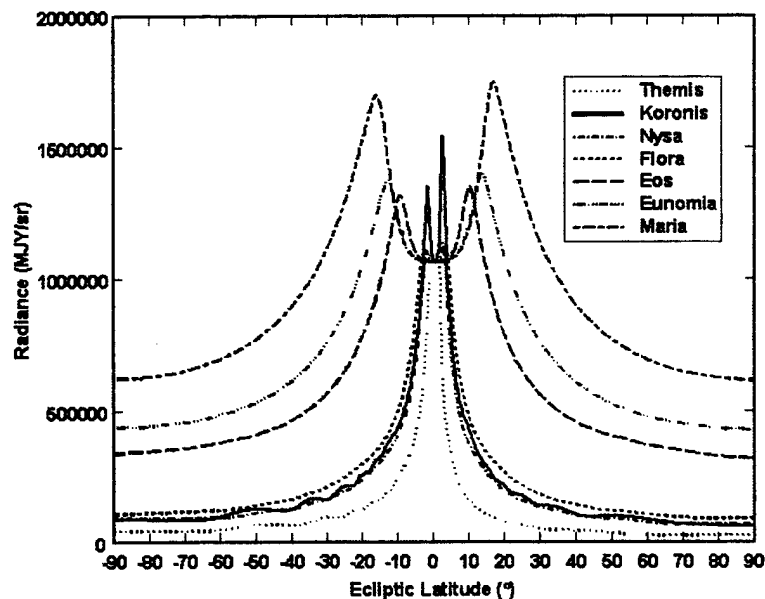


Figure A-4: Latitudinal profiles of dust. Each of the seven dust families profiles are shown for an elongation of 90°.

### A.5 Results

CBZODY6 is a multi-spectral model capable of producing output between 0.2 $\mu\text{m}$  and 300 $\mu\text{m}$ . Any spectral response function may be used in that range. The precomputed volume emissivity function constrains the spectral resolution to either 0.01 $\mu\text{m}$  between 0.2 and 30 $\mu\text{m}$ , or 0.1 $\mu\text{m}$  between 0.2 and 300 $\mu\text{m}$ . The following sections detail comparisons between CBZODY6 and a variety of datasets and data types.



### A.5.1 Reach et al. (1996) ISO comparison

Reach et al. (1996) obtained a spectrum between 5 and 16.5 $\mu\text{m}$  using the Infrared Space Observatory (ISO) on 21 Jan 1996 and having a solar elongation of 104.3°. Their observation and the CBZODY6 fit to the data are shown in Figure A-5. Reach et al. attempted to fit various constituent materials to the observation. They concluded that astronomical silicate with either an interplanetary or a lunar mass distribution had the best fit based on a reduced  $\chi^2$  goodness of fit. For our analysis, we found that a mixture of 65% astronomical silicate and 35% graphite provided an improved fit over astronomical silicate. For astronomical silicate we find a reduced  $\chi^2$  of 0.73, while the astronomical silicate and graphite mixture produced a reduced  $\chi^2$  of 0.41.

Overall, we conclude the fit to the data is quite good considering that the true chemical composition of the zodiacal dust is unknown. Attempts at single chemical compositions have proven to be inadequate. Our choice of graphite clearly shows and improvement in the short wavelength region of the ISO spectrum.

Between 10 and 16 $\mu\text{m}$  Figure A-5 shows that neither astronomical silicate nor the astronomical silicate mixture can completely reproduce the observations. The search for a better match to the spectra will continue.

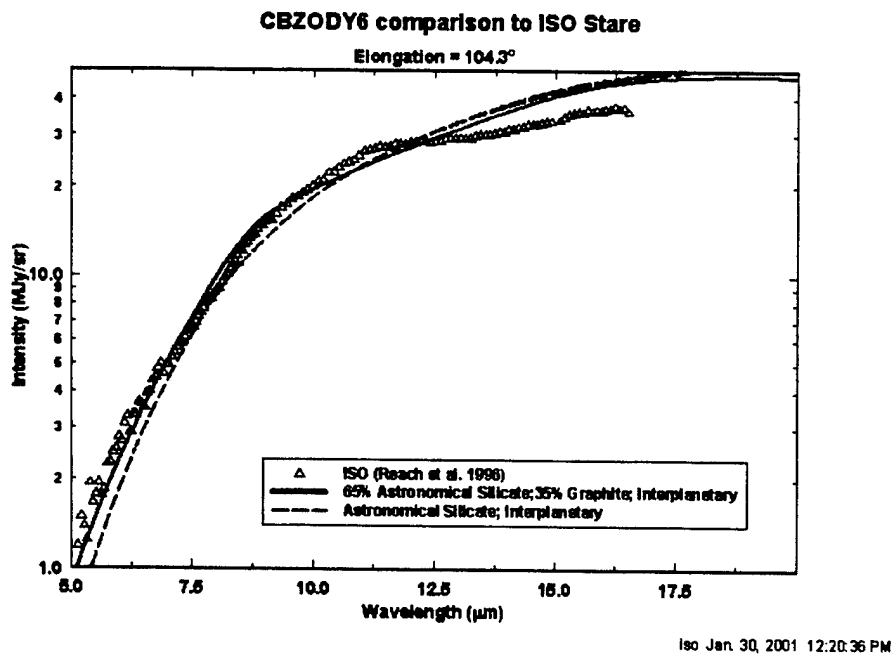
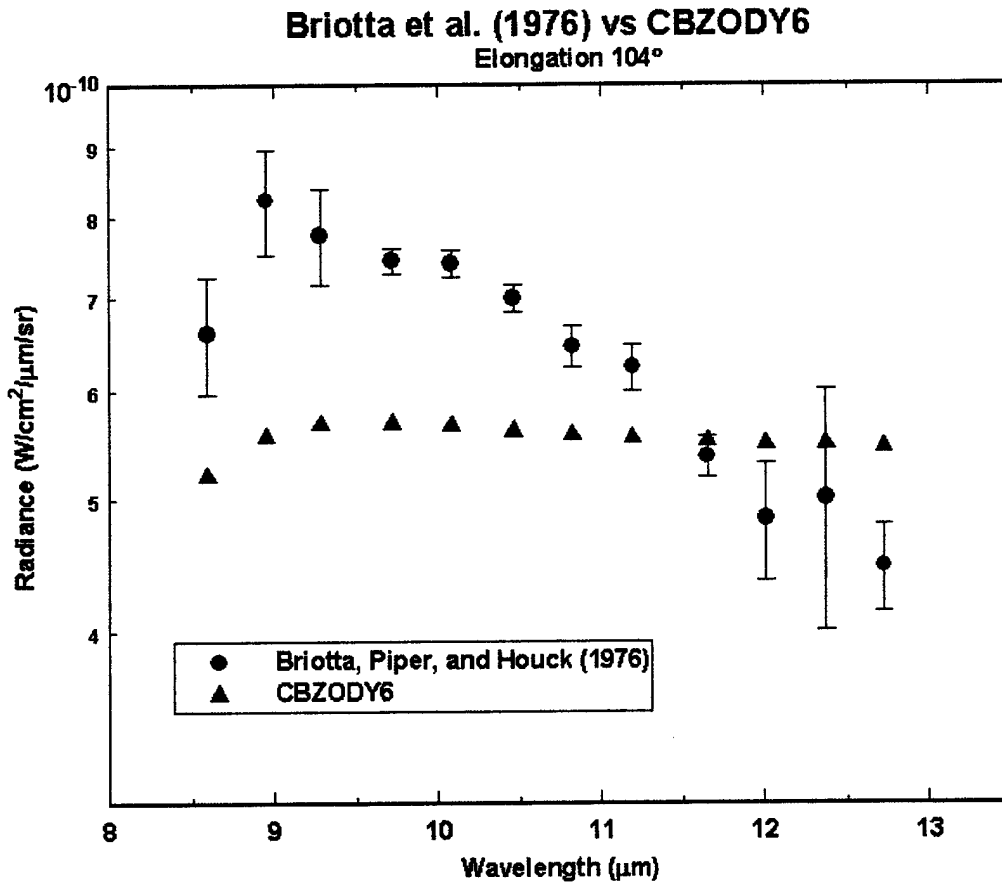


Figure A-5: ISO spectrum of Reach et al. (1996). A comparison of the ISO spectrum compared to Astronomical Silicate and the Astronomical Silicate/Graphite mixture used in CBZODY6.

### A.5.2 Briotta, et al. 1976 Small Rocket Data

At 10h 34m UT on 14 October 1975, a small rocket was sent aloft for observations of the zodiacal light (Briotta et al. 1976). A single observation in 12 channels at an elongation of 104° was obtained and is shown in Figure A-6. This observation is very similar to the ISO observation obtained by Reach et al. This again shows the uncertainties in material composition of the zodiacal cloud.



**Figure A-6: Spectral output of CBZODY compared to the spectrum obtained by Briotta et al. (1976).** The CBZODY composition is 65% astronomical silicate and 35% graphite. There are discrepancies indicating that the true composition has not been determined.

### A.5.3 Extended Spectral Comparisons

Figures A-7 and A-8 show the fit of the CBZODY6 model to a wide range of data covering visible to infrared ranges. The source of the visible data for these figures is the article of Leinert and Grün (1990). Leinert and Grün compiled several satellite and small rocket observations (Vela, Helios, etc.) and scaled them all to a 90° elongation. We have also included a single point from Leinert et al's (1997) sky brightness reference table at 0.5μm. Presumably, the satellite data were used to generate the latter table. The infrared data are from the IRAS, COBE, and MSX satellites. Figure A-7 shows the spectral range from 0.2 to 30μm in spectral steps of 0.01μm. Figure A-8 shows the extended range from 0.2 to 300μm in steps of 0.1μm.

Between 1 and 2μm we have overlap, and considerable variation, between the COBE data, Bands 1 (1.24μm) & 2 (2.4μm), and Leinert and Grün's dataset. We felt the COBE observations have been more carefully calibrated and hence are more trustworthy and we have given the COBE data a higher weight when performing the fit. As a result, as Figure A-7 shows, the CBZODY6 model over-predicts the visible observations from Leinert and Grün by a

considerable amount. We can only speculate at a probable cause; calibration errors or, since the visible observations were all scaled to 90° elongation using an exponential law, the scaling law may not be exact.

The fits to the COBE, IRAS and MSX data are acceptable. As indicated by the ISO spectrum the 12 micron data or IRAS, COBE, and MSX will be slightly under predicted. There also seems to be calibration differences between COBE and IRAS at 25μm. Again, COBE data are considered of higher quality.

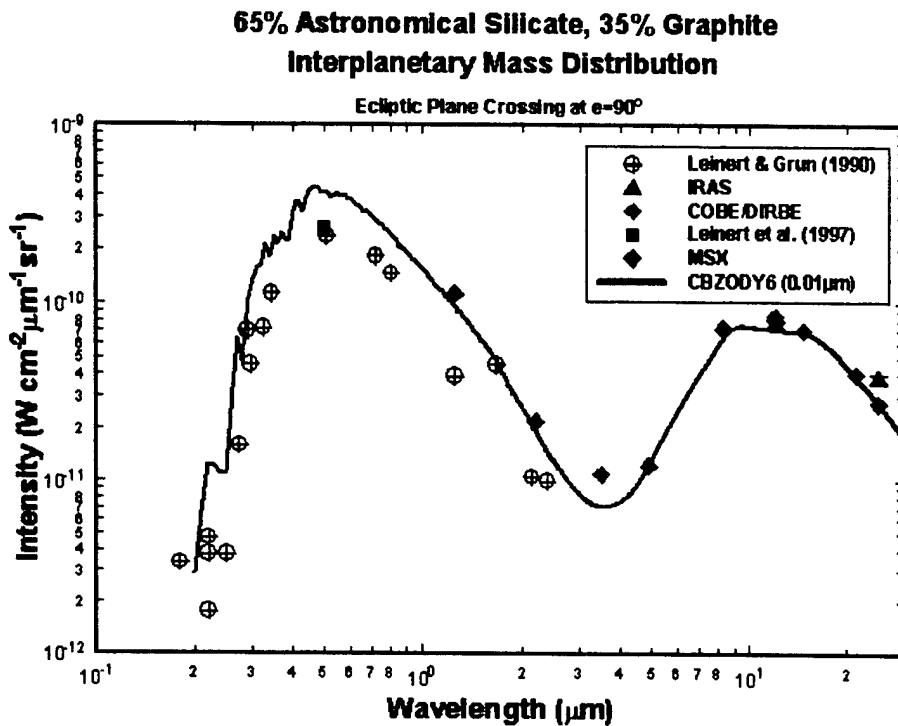
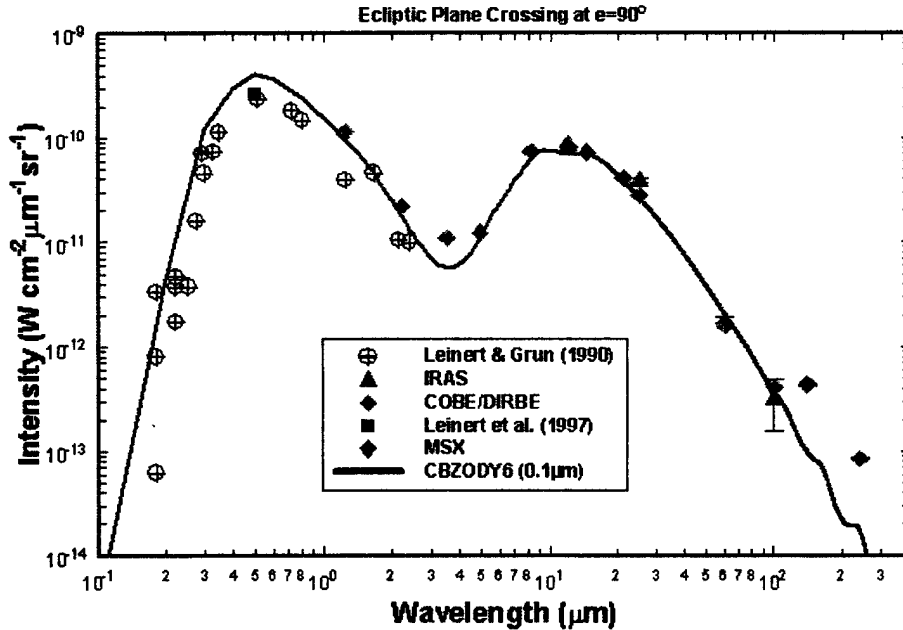


**Figure A-7: Zodiacal spectrum, solid line, compared to a variety of data sets for a 90° elongation.** Between 1 and 3μm, discrepancies appear between the Leinert and Grün data and the COBE/DIRBE data. We chose to weight the COBE/DIRBE data more heavily in the fit.

Figure A-8 is similar to Figure A-7 except that it has a lower spectral resolution and an extended range. The lower spectral resolution leads to fewer spectral features in the scattered, visible, region of the spectrum. Figure A-8 further shows that COBE bands 7 (60μm) and 8 (100μm) show reasonable agreement. Discrepancies are seen in Bands 9 (140μm) and 10 (240μm). This is expected since we have not included a cirrus (galactic dust) model.

**65% Astronomical Silicate, 35% Graphite  
Interplanetary Mass Distribution**



Spectral2 Nov. 17, 2000 11:58:19 AM

**Figure A-8:** Similar to Figure A-7 the zodiacal spectrum out to  $300\mu m$ . The deviations at  $140\mu m$  and  $230\mu m$  between the model and COBE/DIRBE data are due to the lack of a galactic dust (cirrus) model and not errors in the zodiacal dust model.

#### A.5.4 Visible Zodiacal Table

Leinert et al. (1998) produced a table of zodiacal brightness for the visible,  $0.50\mu m$ , their Table 37. That table, in units of  $10^{-8}\ W\ m^{-2}\ sr^{-1}\ \mu m^{-1}$  has been reproduced in Table A-3. However, assuming that Leinert et al.'s table was produced using the visible data of Figure A-7 and A-8, their table will be of lower quality than those produced by the CBZODY6 model which includes the higher quality COBE/DIRBE data. Table A-4 is a listing of the solar elongation for each of the points in Table A-3. We have reproduced tables similar to Leinert et al. in Tables A-5, A-6, A-7, & A-8. These tables give zodiacal brightness in units of  $10^{-8}\ W\ m^{-2}\ sr^{-1}\ \mu m^{-1}$  for four time periods in the year: 21 March; 21 June; 21 September; and 21 December respectively. As expected, the brightness from CBZODY6 is higher than Leinert et al. at all positions.

**Table A-3: Zodiacal light brightness (Leinert et al. 1997) in units of  $10^{-8} \text{ W m}^{-2} \text{ sr}^{-1} \mu\text{m}^{-1}$  for a wavelength of  $0.50 \mu\text{m}$ .**

$\beta$ $\lambda-\lambda_0$	0°	5°	10°	15°	20°	25°	30°	45°	60°	75°	90°
0°				3140	1610	985	640	275	150	100	77
5°				2940	1540	945	625	271	150	100	77
10°			4740	2470	1370	865	590	264	148	100	77
15°	11500	67800	3440	1860	1110	755	525	251	146	100	77
20°	6400	4480	2410	1410	910	635	454	237	141	99	77
25°	3840	2830	1730	1100	749	545	410	223	136	97	77
30°	2480	1870	1220	845	615	467	365	207	131	95	77
35°	1650	1270	910	680	510	397	320	193	125	93	77
40°	1180	940	700	530	416	338	282	179	120	92	77
45°	910	730	555	442	356	292	250	166	116	90	77
60°	505	442	352	292	243	209	183	134	104	86	77
75°	338	317	269	227	196	172	151	116	93	82	77
90°	259	251	225	193	166	147	132	104	86	79	77
105°	212	210	197	170	150	133	119	96	82	77	77
120°	188	186	177	154	138	125	113	90	77	74	77
135°	179	178	166	147	134	122	110	90	77	73	77
150°	179	178	165	148	137	127	116	96	79	72	77
165°	196	192	179	165	151	141	131	104	82	72	77
180°	230	212	195	178	163	148	134	105	83	72	77

**Table A-4: Elongation of observation points in Table A-3.**

$\beta$ $\lambda-\lambda_0$	0°	5°	10°	15°	20°	25°	30°	45°	60°	75°	90°
0°	x	5.00	10.00	15.00	20.00	25.00	30.00	45.00	60.00	75.00	90.00
5°	5.00	7.07	11.17	15.79	20.59	25.46	30.38	45.22	60.13	75.06	90.00
10°	10.00	11.17	14.11	17.96	22.27	26.81	31.48	45.86	60.50	75.23	90.00
15°	15.00	15.79	17.96	21.09	24.81	28.90	33.23	46.92	61.12	75.52	90.00
20°	20.00	20.59	22.27	24.81	27.99	31.61	35.53	48.36	61.98	75.92	90.00
25°	25.00	25.46	26.81	28.91	31.61	34.78	38.29	50.14	63.05	76.43	90.00
30°	30.00	30.38	31.47	33.23	35.53	38.29	41.41	52.24	64.34	77.05	90.00
35°	35.00	35.31	36.22	37.70	39.67	42.06	44.81	54.60	65.82	77.76	90.00
40°	40.00	40.26	41.03	42.27	43.96	46.03	48.44	57.20	67.48	78.56	90.00
45°	45.00	45.22	45.86	46.92	48.36	50.14	52.24	60.00	69.30	79.46	90.00
60°	60.00	60.13	60.50	61.12	61.98	63.05	64.34	69.30	75.52	82.56	90.00
75°	75.00	75.06	75.23	75.52	75.92	76.43	77.05	79.46	82.56	86.16	90.00
90°	90.00	90.00	90.00	90.00	90.00	90.00	90.00	90.00	90.00	90.00	90.00
105°	105.00	104.94	104.77	104.48	104.08	103.57	102.95	100.54	97.44	93.84	90.00
120°	120.00	119.87	119.50	118.88	118.02	116.95	115.66	110.70	104.48	97.44	90.00
135°	135.00	134.78	134.14	133.08	131.64	129.86	127.76	120.00	110.70	100.54	90.00
150°	150.00	149.62	148.52	146.77	144.47	141.71	138.59	127.76	115.66	102.95	90.00
165°	165.00	164.21	162.04	158.91	155.19	151.10	146.77	133.08	118.88	104.48	90.00
180°	180.00	175.00	170.00	165.00	160.00	155.00	150.00	135.00	120.00	105.00	90.00

**Table A-5: Zodiacal light brightness from CBZODY6 in units of  $10^{-8} \text{ W m}^{-2} \text{ sr}^{-1} \mu\text{m}^{-1}$  for a wavelength of  $0.50 \mu\text{m}$  for 21 March.**

$\beta$ $\lambda-\lambda_0$	0°	5°	10°	15°	20°	25°	30°	45°	60°	75°	90°
0°	x	131810	15425	4497	1970	1095	706	307	190	138	120
5°	1020800	100230	15087	4521	1984	1100	708	306	189	138	120
10°	128890	46941	12262	4276	1957	1095	706	305	189	138	120
15°	38795	22341	8702	3691	1837	1063	694	302	188	137	120
20°	16710	11859	5976	2998	1644	1000	668	297	186	137	120
25°	8776	6948	4146	2375	1423	915	631	291	184	136	120
30°	5231	4415	2956	1873	1211	821	586	282	181	135	120
35°	3407	2997	2173	1487	1024	728	538	272	178	134	120
40°	2370	2142	1648	1194	866	642	490	262	174	133	120
45°	1735	1601	1285	975	737	566	444	250	170	132	120
60°	852	820	711	586	480	397	332	214	156	128	120
75°	534	530	482	416	354	303	263	185	145	126	120
90°	407	411	387	348	305	268	236	174	141	125	120
105°	371	379	365	336	302	269	241	178	143	125	120
120°	406	415	404	378	343	307	274	197	151	127	120
135°	536	548	532	497	448	396	346	230	163	130	120
150°	863	873	833	758	663	564	473	276	177	132	120
165°	1596	1580	1443	1238	1015	809	638	321	188	134	120
180°	2313	2246	1966	1602	1251	956	727	341	192	135	120

**Table A-6: Zodiacal light brightness from CBZODY6 in units of  $10^{-8} \text{ W m}^{-2} \text{ sr}^{-1} \mu\text{m}^{-1}$  for a wavelength of  $0.50 \mu\text{m}$  for 21 June.**

$\beta$ $\lambda-\lambda_0$	0°	5°	10°	15°	20°	25°	30°	45°	60°	75°	90°
0°	x	134690	15091	4182	1747	937	591	251	154	110	94
5°	955290	107410	15511	4391	1823	969	606	253	155	110	94
10°	120560	50001	12764	4246	1846	988	616	254	155	110	94
15°	36273	23455	9069	3695	1758	976	615	254	155	110	94
20°	15615	12258	6204	3011	1585	928	600	252	154	109	94
25°	8194	7084	4279	2383	1377	854	572	248	152	109	94
30°	4880	4455	3029	1873	1172	769	534	242	151	108	94
35°	3175	2993	2210	1481	990	683	492	235	148	107	94
40°	2207	2122	1662	1183	835	602	448	226	145	107	94
45°	1615	1574	1286	960	708	530	406	217	142	106	94
60°	795	791	694	565	454	367	302	185	129	103	94
75°	503	503	457	390	326	274	233	157	119	101	94
90°	388	387	360	317	274	236	206	146	115	100	94
105°	357	355	334	301	266	233	206	148	116	100	94
120°	393	389	367	334	297	262	231	162	122	101	94
135°	523	513	481	435	384	334	288	187	131	103	94
150°	843	819	753	663	566	472	390	222	141	105	94
165°	1558	1486	1309	1086	866	676	524	257	149	106	94
180°	2255	2112	1784	1405	1065	795	594	271	151	106	94

**Table A-7: Zodiacal light brightness from CBZODY6 in units of  $10^{-8} \text{ W m}^{-2} \text{ sr}^{-1} \mu\text{m}^{-1}$  for a wavelength of  $0.50 \mu\text{m}$  for 21 September.**

$\beta$ $\lambda-\lambda_0$	0°	5°	10°	15°	20°	25°	30°	45°	60°	75°	90°
0°	x	150480	16384	4357	1743	903	556	229	141	102	87
5°	997370	104520	15393	4294	1739	902	555	228	141	102	87
10°	125910	46630	12017	3971	1701	897	554	227	140	101	87
15°	37898	21734	8303	3363	1584	871	546	225	139	101	87
20°	16323	11417	5597	2691	1406	818	528	222	138	100	87
25°	8572	6643	3834	2106	1209	747	499	218	136	100	87
30°	5110	4198	2705	1644	1022	669	464	213	135	99	87
35°	3328	2833	1972	1293	859	591	426	206	132	98	87
40°	2315	2013	1483	1031	723	520	388	198	130	97	87
45°	1695	1494	1146	835	611	457	351	190	127	96	87
60°	832	748	616	489	390	316	261	163	116	93	87
75°	522	472	402	333	277	234	200	138	106	91	87
90°	397	362	316	270	231	199	174	126	102	90	87
105°	362	333	296	259	225	197	174	128	102	90	87
120°	396	367	330	292	256	224	197	140	107	91	87
135°	524	487	440	388	337	291	250	163	116	93	87
150°	842	785	701	604	508	420	345	196	125	94	87
165°	1557	1442	1240	1010	794	613	472	230	133	96	87
180°	2257	2066	1712	1327	992	733	543	245	137	96	87

**Table A-8: Zodiacal light brightness from CBZODY6 in units of  $10^{-8} \text{ W m}^{-2} \text{ sr}^{-1} \mu\text{m}^{-1}$  for a wavelength of  $0.50 \mu\text{m}$  for 21 December.**

$\beta$ $\lambda-\lambda_0$	0°	5°	10°	15°	20°	25°	30°	45°	60°	75°	90°
0°	x	145780	16473	4612	1949	1054	668	285	176	131	112
5°	1053500	96329	14703	4348	1874	1024	654	282	175	130	112
10°	132940	43419	11377	3945	1789	994	639	278	174	130	112
15°	39997	20538	7887	3326	1646	949	620	273	172	129	112
20°	17220	10944	5355	2665	1456	884	592	267	170	128	112
25°	9038	6448	3700	2095	1251	804	556	260	168	128	112
30°	5384	4116	2636	1646	1060	719	515	252	165	127	112
35°	3504	2804	1940	1305	895	636	472	243	162	125	112
40°	2437	2011	1473	1049	757	561	429	233	158	124	112
45°	1784	1504	1150	856	644	494	389	223	155	123	112
60°	879	771	637	515	420	348	293	192	143	119	112
75°	557	501	430	363	308	265	231	166	132	116	112
90°	429	396	350	304	264	231	205	154	127	115	112
105°	396	372	338	300	265	234	209	157	129	115	112
120°	436	416	383	345	307	272	241	174	136	117	112
135°	579	559	518	466	411	358	311	206	147	119	112
150°	932	903	829	731	625	523	434	250	161	122	112
165°	1721	1652	1464	1222	979	767	597	296	173	124	112
180°	2490	2361	2017	1605	1227	922	692	318	178	126	112

### A.5.5 Photometric observations

An amateur astronomer obtained observations of the zodiacal cloud on the night of 6 March 2000 (Schmude 1999). He obtained 6 observations for each of the 7 points listed in Table A-9.

**Table A-9: Schmude (1999) pointings for zodiacal light observations.**

Point No.	R.A.	Dec
1	2 <sup>h</sup> 05 <sup>m</sup>	+33.5
2	1 <sup>h</sup> 53 <sup>m</sup>	+27.8
3	2 <sup>h</sup> 15 <sup>m</sup>	+23.5
4	2 <sup>h</sup> 21 <sup>m</sup>	+19.2
5	2 <sup>h</sup> 32 <sup>m</sup>	+13.1
6	2 <sup>h</sup> 52 <sup>m</sup>	+9.5
7	2 <sup>h</sup> 54 <sup>m</sup>	+3.6

Schmude visually estimated that Point #4 was the brightest and that points # 1, 2, 6, and 7 were outside of the cloud. He averaged points 1, 2, 6, and 7 to obtain a sky background and used point #4 as sky + zodiacal. Table A-10 is a summary of his observations.

**Table A-10: Schmude B, V, and B-V observations for 6 March 2000.**

	Johnson B	Johnson V
Brightness (mag/sq. arc-sec)	22.37 ± 0.27	21.89 ± 0.42
B-V	0.48 ± 0.50	

To reproduce his observations with CBZODY6, we took the 7 pointings of Table A-9 and ran the model for 0<sup>h</sup> UT on 6 March 2000. Our results are shown in Table A-11.

**Table A-11: CBZODY6 runs for the 7 points of Table A-7.**

R.A.	Dec	Ecl Long	Ecl Lat	Elong	Johnson B	Johnson V
					W/cm <sup>2</sup> /μm	W/cm <sup>2</sup> /μm
33.500	31.250	40.850	19.532	57.387	1.0882E-13	1.1291E-13
27.800	28.250	36.169	15.151	52.065	1.5404E-13	1.5982E-13
23.500	33.750	39.388	9.393	54.220	1.7812E-13	1.8480E-13
19.200	35.250	39.284	4.873	53.706	2.0920E-13	2.1705E-13
13.100	38.000	39.838	-1.751	54.126	2.1547E-13	2.2355E-13
9.500	43.000	43.428	-6.668	57.942	1.6177E-13	1.6784E-13
3.600	43.500	42.150	-12.453	57.310	1.3136E-13	1.3629E-13

Table A-12 shows the photometric parameters for the Johnson B and V bands used to convert the flux units to magnitudes. Using a pixel size of 0.8209 deg/pixel = 2955.25 arc-sec/pixel gives an area, in magnitude units, of 2.5 log (2955.25<sup>2</sup>) = 17.353. Adding the area to the brightness in magnitudes gives a surface brightness in magnitudes per square arc-second.

**Table A-12: Johnson B & V photometric parameters.**

	Johnson B	Johnson V
Center	0.44	0.55
Bandwidth	.098	.089
Flux at 0 mag (W/cm <sup>2</sup> /μm)	6.61e-12	3.72e-12



Table A-13 gives the results of averaging points 1, 2, 6, and 7 which is our representation of the sky background. Our contention is that each of Schmude's 7 observations contains a uniform sky background plus a varying zodiacal component. We can safely ignore true sky radiance since it is ultimately subtracted from the answer.

Table A-14 further shows the contribution from point 4 [zodiacal] and the zodiacal-sky computation. Finally, the flux is converted to magnitudes and magnitudes/square arc-second.

**Table A-13: Point 4 brightness as computed by CBZODY6.**

	Johnson B	Johnson V
Sky (Average of 1,2,6,7) (W/cm <sup>2</sup> /μm)	1.390E-13	1.442E-13
Zodiacal (Point 4) (W/cm <sup>2</sup> /μm)	2.092E-13	2.171E-13
Zodiacal - Sky (W/cm <sup>2</sup> /μm)	7.020E-14	7.284E-14
Brightness (mag)	4.93	4.27
B-V		0.66
Brightness (mag/sq. arc-sec)	22.29	21.62

We find B, V, and B-V are all within the quoted observational errors. CBZODY6 B is 0.08 magnitudes per square arc-second brighter than the observation. The V band is 0.27 magnitudes per square arc-second brighter. His error in B-V gives a range of values which includes Allen's reference value of +0.66 accepted range of B-V for the Sun 0.66.

Schmude's Point #5 actually has the highest zodiacal brightness, being closest to the ecliptic plane. The brightness for that point is given in Table A-14. Note that since his sky measurements were not subtracted, the zodiacal light is over 1 magnitude brighter than his quotes.

**Table A-14: Zodiacal brightness for Point 5.**

	Johnson B	Johnson V
Zodiacal (Point 5) (W/cm <sup>2</sup> /μm)	2.1547E-13	2.2355E-13
Brightness (mag)	3.72	3.05
B-V		0.66
Brightness (mag/sq. arc-sec)	21.07	20.41

Absolute ground based measurements of the zodiacal light are difficult to obtain. However, the zodiacal light is a measurable, not to mention visible to the naked eye, phenomenon which sensor systems must be aware of for proper operation.

### A.5.6 Visible Imaging

On the evening of 5 April 1997 Marco Fulle climbed to the 750m mark on the volcanic island of Mt. Stromboli off the coast Sicily. He took the 3 minute photograph shown in Figure A-9 (which also appeared in the January 2001 issue of Sky & Telescope). The image has several components:

- The image is looking west towards the horizon with the last few minutes of twilight visible as the bright yellow band.

- Below the twilight is the hard Earth
- Just above the twilight, bottom left of center, is the planet Mercury
- The stars are visible with the Pleiades prominent near the top left of center
- Comet Hale-Bopp is very noticeable to the right of center
- The zodiacal light is visible above the twilight

Figure A-10 shows our effort to recreate this image using the components of CBSD and the Air Force Research Laboratory's atmospheric transmission model MODTRAN. The creation of the image took several steps. Since this is a horizon image, atmospheric attenuation is an important factor. Also, the sky radiance from twilight needs to be included.

1. The image was taken using Kodak Elitechrome 400 film. Using the Kodak data sheets, filter functions were derived for Yellow, Magenta, and Cyan forming layers. Since this is a reversal film, these correspond to Blue, Green, and Red with responses similar to the human eye.
2. Refraction was also found to be important and a simple refraction function was included in the CBSD codes (Meeus 1996, p56).
3. Using MODTRAN, we created a database of radiance and transmittance as a function of altitude for the date, time, and look angles associated with the image in each of the three bands.
4. The models CBAMP4 and CBSKY4 were run with the atmospheric attenuation found from MODTRAN.
5. A point spread function, simple circular with gaussian fall off, was used on the CBAMP4 and CBSKY4 images.
6. It was found that the atmospheric radiance as produced by MODTRAN extended  $1.2^\circ$  above the horizon (the Sun was  $15.7^\circ$  below the horizon for this image). This is contrary to the observation that shows Mercury, at an apparent altitude of  $3.1^\circ$ , still within the twilight. To compensate, the radiance database was extended by a simple extrapolation.
7. The model CBZODY6 was run with atmospheric attenuation and included the MODTRAN sky radiance (only one model needed the sky radiance). CBZODY6 was structurally closest to the requirements of a sky radiance model.
8. Finally, the images needed the application of the film's characteristic curve for the correct color balance. This proved to be difficult due to the lack of information on the low light level characteristics of this film. The published characteristic curve was used. However, the log intensity of the illumination for the characteristic curve ranges from  $-3.5$  to  $0$  lux-seconds. The model predicated a range of  $-6$  to  $-2$  lux-seconds (wavelength dependence was included in the  $W\text{-cm}^2$  to lux conversion). The solution was to use an empirical approximation of the characteristic curve (Lehmann and Häupl, 1986). We then included a linear extension for low illumination levels.



**Figure A-9: Image of the zodiacal light taken from Mt. Stromboli by Marco Fulle.** On the evening of 5 April 1997, Marco Fulle took an image of the zodiacal light seen stretching from the horizon to the Pleiades. (© Marco Fulle, 1997, used with permission.)



**Figure A-10: A CBSD and MODTRAN view of the same region as Figure A-9.**

We have come up with a final image that resembles, but is not identical to the observations:

- The contrast and color balance of the simulated image are very close to but do not exactly match the original. This is attributable to uncertainties in the shape of the characteristic curve.
- The sky radiance was used as a linear function with altitude above the horizon. No azimuthal dependencies were included and this clearly is a limitation.

- The overall shape of the zodiacal light shows more of an egg shape rather than a bubble. We attribute this to two possible causes; 1) the atmospheric attenuation is not as great as MODTRAN predicts; 2) the sky radiance extends even higher filling in the zodiacal structure. Figure A-11 shows the shape of the zodiacal light without (a) and with (b) atmospheric attenuation. The unattenuated image shows a shape much closer to the observed image.
- Comets are not included in the CBSD simulation.

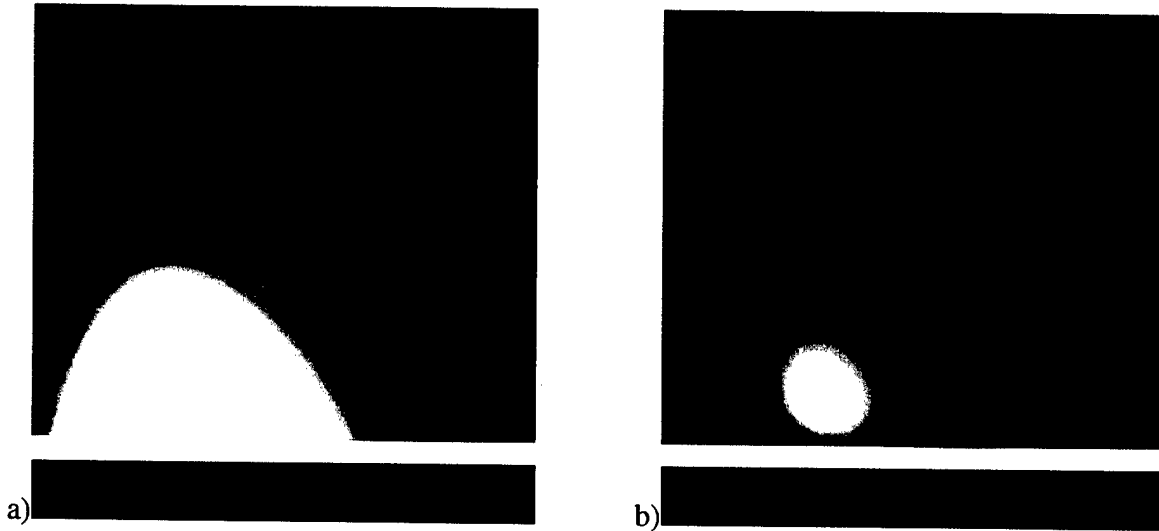
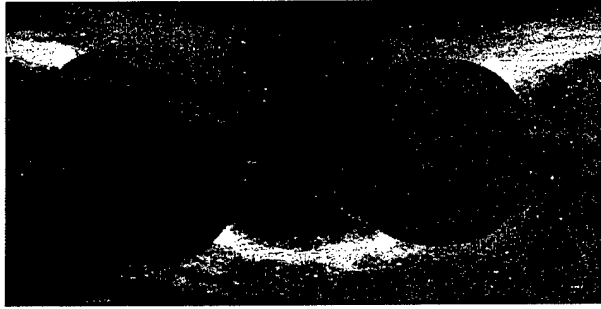


**Figure A-11: Single band atmospheric attenuation.** a) CBZODY6 including refraction and twilight sky radiance from MODTRAN b) CBZODY6 refraction, twilight sky radiance, and attenuation (twilight sky radiance and attenuation from MODTRAN). Indications are that the atmospheric attenuation observed is much less than that predicted by MODTRAN.

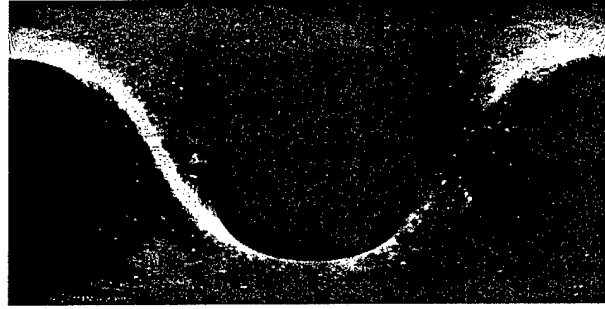
### A.5.7 COBE CIO daily all sky coverage

The COBE/DIRBE CIO (Calibrated Individual Observations) are the complete set of observations obtained during the COBE mission. They have not been weekly averaged, as the skymap data have.

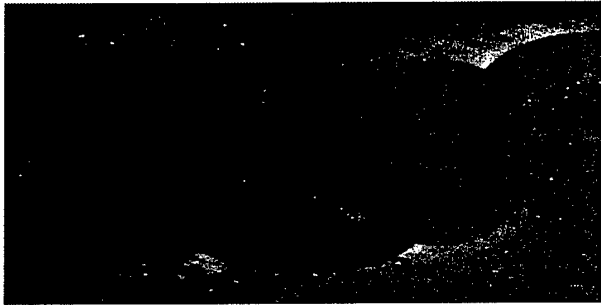
For our analysis, we took 38 CIO days distributed throughout the mission. For each day we ran a non-linear least squares routine for a set of 8 parameters; ascending node, inclination, HWHM, and normalization density for the two planes. We excluded the region of the image that contained the galactic plane. Figure A-12 shows the percentage error for two typical days a) and b). In Figures A-12 c) and d) the exclusion zone are overlaid. Since the galaxy is not regular, some regions of the plane do appear outside of the zone. We found this had very little effect on the fit results, however, it did occasionally affect the quoted standard deviation.



a) CIO 89365 percentage error



b) CIO 90263 percentage error



c) CIO 89365 percentage error with galactic exclusion zone shown



d) CIO 90263 percentage error with galactic exclusion zone shown

**Figure A-12: Location of the galactic exclusion zone.** Note that the zone does not always exclude all galactic components.

Table A-15 shows the results of individually fitting 38 CIO datasets. This represents the best fit to that dataset for only Band 5.  $l$  is the mean solar longitude during the observation. The Mean Deviation ( $\alpha$ ) is defined as:

$$\alpha = 100 \times \frac{1}{N} \sum_i \left| \frac{d_i - x_i}{d_i} \right| \%$$

where  $d_i$  is the observed data value and  $x_i$  is the modeled data value. The subscripts 1 and 2 refer to the inner and outer plane respectively.

Table A-16 shows the mean and standard deviations for 67 CIO datasets using the generalized parameter of the Table A-1 set obtained from the fit in 3 COBE/DIRBE bands (4,5 and 6)

Table A-17 is the mean of all observations. It represents our final error between CBZODY6 and the CIO data. Figure A-13 shows the mean error plotted against the heliocentric ecliptic longitude of the Earth.

Figures A-14, A-15, and A-16 show typical fits in COBE/DIRBE bands 4, 5, and 6 respectively. Each figure has 4 panes a) the original CIO data, b) the CBZODY6 fit, c) the residual, and d) the percentage error.

**Table A-15: Mean deviations for all NLS parameter fit CIO datasets for Band 5.**

CIO	$l$ (°)	$\alpha$ (%)	$\sigma$	$\Omega_1$	$\Omega_2$	$i_1$	$i_2$	$\Gamma_1$	$\Gamma_2$	$N_1$	$N_2$
89345	79.6	1.70	0.60	86.89	79.19	2.467	2.392	0.378	0.288	1.208	1.550
89346	80.2	1.69	0.77	85.85	79.05	2.600	2.332	0.379	0.288	1.205	1.553
89347	81.5	1.69	0.75	86.44	79.35	2.488	2.377	0.376	0.288	1.208	1.547
89348	82.4	1.68	1.15	85.83	79.03	2.489	2.376	0.376	0.287	1.208	1.547
89349	83.8	1.69	0.61	85.96	78.87	2.498	2.370	0.376	0.287	1.210	1.546
89350	84.3	1.71	1.10	85.37	78.89	2.553	2.377	0.381	0.284	1.201	1.557
89365	99.9	1.67	0.27	82.82	78.92	2.496	2.457	0.377	0.286	1.205	1.531
90005	104.5	1.72	11.43	84.17	76.01	2.772	2.344	0.385	0.280	1.192	1.551
90010	110.0	1.70	0.29	81.69	78.62	2.621	2.475	0.379	0.285	1.200	1.526
90020	120.0	1.71	16.32	77.43	77.40	2.317	2.380	0.372	0.282	1.215	1.524
90041	141.0	1.69	0.72	76.80	79.65	2.677	2.425	0.368	0.283	1.219	1.506
90050	151.2	9.17	0.64	83.59	75.95	2.946	2.444	0.375	0.283	1.198	1.504
90060	160.2	1.46	1.61	85.46	72.26	2.900	2.387	0.371	0.282	1.208	1.511
90071	171.2	1.33	5.01	90.98	71.04	2.989	2.417	0.369	0.281	1.222	1.515
90080	181.1	1.27	1.24	81.42	75.43	3.000	2.371	0.366	0.278	1.227	1.520
90100	200.1	1.28	8.12	93.48	85.05	2.706	2.269	0.388	0.275	1.188	1.533
90114	214.7	1.29	2.77	83.50	83.79	2.785	2.300	0.373	0.281	1.202	1.504
90115	215.7	1.30	1.56	82.89	83.47	2.792	2.311	0.372	0.281	1.204	1.502
90116	216.0	1.30	2.02	82.94	82.61	2.792	2.299	0.371	0.281	1.206	1.504
90118	217.1	1.53	27.72	78.80	82.90	2.667	2.234	0.351	0.276	1.250	1.506
90134	232.5	1.59	15.39	80.89	80.17	3.000	2.331	0.361	0.277	1.227	1.527
90135	233.8	1.62	19.84	80.92	79.58	3.000	2.286	0.362	0.272	1.226	1.548
90140	239.8	1.49	10.69	80.68	79.88	3.000	2.300	0.361	0.280	1.229	1.532
90145	244.2	1.63	25.10	80.52	79.35	3.000	2.328	0.350	0.277	1.249	1.534
90150	248.2	1.60	23.53	80.44	78.16	3.000	2.251	0.356	0.277	1.236	1.542
90166	264.0	1.54	14.20	81.81	78.89	3.000	2.392	0.366	0.279	1.208	1.550
90168	265.1	1.64	84.35	84.48	78.58	3.000	2.030	0.351	0.280	1.235	1.542
90175	272.1	1.53	10.36	82.62	77.93	3.000	2.523	0.366	0.286	1.209	1.541
90187	284.6	1.73	46.08	81.94	78.10	3.000	2.484	0.367	0.276	1.199	1.562
90199	295.6	1.61	13.92	80.99	77.47	2.978	2.633	0.367	0.284	1.202	1.556
90205	302.5	1.68	40.76	80.95	77.16	2.949	2.568	0.370	0.277	1.203	1.581
90212	307.8	1.77	18.87	78.89	76.04	2.888	2.570	0.377	0.276	1.193	1.599
90220	315.1	1.58	30.56	70.28	77.49	2.641	2.533	0.376	0.280	1.197	1.593
90235	330.2	1.60	70.42	78.78	75.25	3.000	2.439	0.379	0.277	1.204	1.624
90241	336.0	1.58	66.73	80.67	75.21	3.000	2.438	0.382	0.277	1.195	1.635
90245	338.2	1.47	29.42	83.29	76.38	3.000	2.489	0.375	0.281	1.201	1.620
90251	346.0	1.49	48.77	88.21	74.82	3.000	2.453	0.375	0.280	1.199	1.623
90263	356.9	1.62	147.59	95.66	75.80	3.000	2.409	0.384	0.271	1.188	1.662

**Table A-16: Mean deviations and standard deviations for all modeled CIO datasets in 3 bands using generalized parameter set.**

Day	Solar Longitude	Band 4		Band 5		Band 6	
		$\alpha$	$\sigma$	$\alpha$	$\sigma$	$\alpha$	$\sigma$
89345	79.65	8.27	0.15	11.76	9.84	3.26	3.68
89346	80.18	8.21	0.16	11.67	9.39	3.2	3.44
89347	81.42	7.89	0.14	11.98	10.44	3.23	3.75
89348	82.46	7.91	0.14	12.01	10.83	3.2	3.59
89349	83.76	7.92	0.13	12.01	10.3	3.18	3.48
89350	84.28	8.07	0.19	12.17	10.8	3.15	3.86
89351	85.46	8.04	0.79	12.05	39.18	3.13	51.53
89360	95.00	8.56	0.11	12.67	10.75	3.08	3.27
89365	99.94	8.41	0.16	12.88	10.91	3.06	3.11
90005	104.51	8.2	0.24	13.27	22.44	3.08	35.71
90010	110.05	7.96	0.17	13.29	11.32	4.09	3.09
90015	115.47	8.3	0.39	13.34	13.71	3.15	6.73
90017	116.62	8.26	0.15	13.36	11.74	3.18	3.83
90020	120.05	8.63	0.24	13.53	27.24	3.19	53.66
90023	123.64	8.58	0.12	13.69	13.75	3.27	3.22
90025	124.71	8.57	0.13	13.86	14.87	3.36	3.46
90031	131.76	8.5	0.18	13.9	16.07	3.45	12.04
90035	135.82	8.89	0.57	13.94	42.06	3.64	63.25
90041	141.09	8.53	0.16	14.23	12	3.84	25.03
90045	144.92	8.97	0.44	14.68	19.95	3.98	44.1
90047	147.52	8.8	0.27	14.66	17.05	4	29.17
90050	151.27	9.41	0.19	24.02	11.75	38.89	16.48
90055	155.39	8.74	0.13	14.83	11.01	4.05	14.62
90060	160.16	8.79	0.27	14.49	11.18	3.94	31.09
90065	165.78	9.35	1.61	14.14	43.33	3.88	76.97
90071	171.15	8.5	0.16	14	13.6	3.8	20.41
90073	173.91	8.51	0.19	14.04	9.81	3.76	22.18
90075	175.93	9.08	0.47	13.93	46.6	3.79	105.32
90078	178.33	8.82	0.15	14.02	9.46	3.81	12.11
90080	181.21	9.16	0.54	14.08	9.53	3.8	33.8
90085	184.75	8.95	0.18	13.99	11.82	3.82	47.2
90090	191.41	8.78	0.18	13.94	8.84	3.81	26.09
90095	194.57	9.05	0.47	14.1	85.42	3.87	177.54
90100	200.06	9.32	1.51	14.36	17.17	3.91	44.8
90105	205.9	9.14	0.61	14.8	13.01	4.01	6.16
90114	214.82	9.69	0.4	14.66	14.62	3.9	7.5
90115	215.72	9.47	0.29	14.51	13.5	3.87	6.63
90116	216	9.34	0.38	14.51	13.98	3.88	6.34
90118	217.06	9.35	0.53	14.35	39.65	3.85	95.62
90127	225.83	8.88	0.41	13.88	27.22	3.73	74.9
90134	232.47	9.04	0.34	13.34	26.62	3.68	65.15
90135	233.73	9.56	0.34	12.69	29.22	3.63	71.66
90140	239.83	9.03	0.65	12.59	20.51	3.41	42.98
90145	244.23	9.1	0.27	12.64	34.95	3.41	114.64
90150	248.18	8.73	0.3	12.58	33.61	3.61	63.48



**Table A-16: (cont.)**

Day	Solar	Band 4		Band 5		Band 6	
	Longitude	$\alpha$	$\sigma$	$\alpha$	$\sigma$	$\alpha$	$\sigma$
90155	254.48	8.65	0.65	12.71	28.28	3.19	63.66
90164	263.23	9.34	1.76	12.6	54.19	3.03	138.34
90165	263.78	9.19	0.24	12.47	19.32	2.96	33.83
90166	264.03	8.81	0.15	12.34	24.12	2.93	62.07
90168	265.1	8.82	0.52	12.35	94.79	2.95	80.61
90175	272.15	8.69	0.23	11.66	19.81	2.99	28.8
90180	278.35	8.8	0.16	11.83	34.43	3.01	112.96
90185	281.46	8.88	0.2	12.18	45.72	3.4	168.9
90187	284.71	8.93	0.23	12.23	56.41	3.41	208.35
90195	290.56	9.03	0.22	11.61	35.38	3.26	109.43
90199	295.45	8.93	0.15	11.24	23.12	3.21	58.2
90205	302.53	9.11	0.22	10.96	49.88	3.25	172.62
90212	307.56	9.98	0.32	10.48	27.14	3.35	72.83
90215	310.67	10.01	0.19	10.1	17.71	3.25	49.19
90220	315.22	10.13	0.21	9.94	37.99	3.36	127.97
90225	320.08	10.62	0.69	9.53	59.41	3.45	195.73
90235	330.41	10.07	0.34	9.37	76.77	3.42	321.63
90241	335.99	10.12	0.21	9.18	72.57	3.33	321.06
90245	338.14	9.85	0.22	9.14	34.66	3.27	147.07
90251	346.16	9.92	0.2	9.31	54.32	3.12	218.66
90255	350.78	9.77	0.28	9.16	79.38	3.06	334.3
90263	356.78	9.59	0.31	9.06	154.9	3.08	309.6

**Table A-17: Average of all mean deviations; the mean deviation of all modeled observations.**

<b>Band 4</b>	<b>Band 5</b>	<b>Band 6</b>
9.0%	12.8%	4.0%

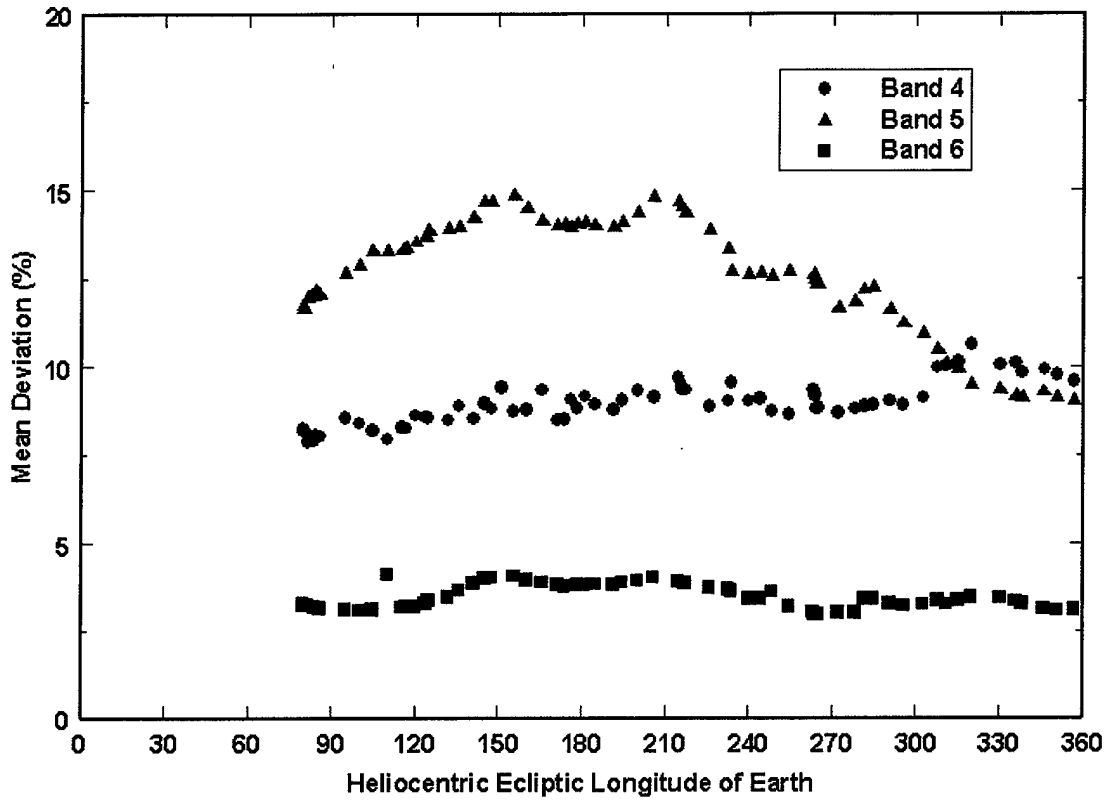
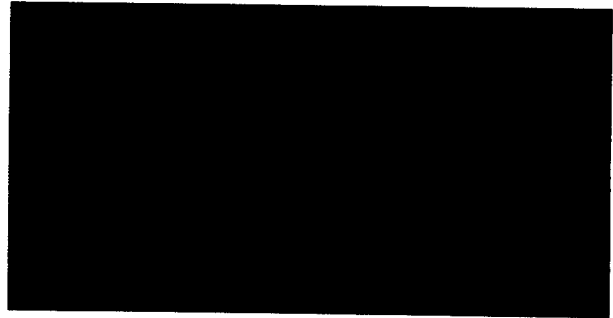


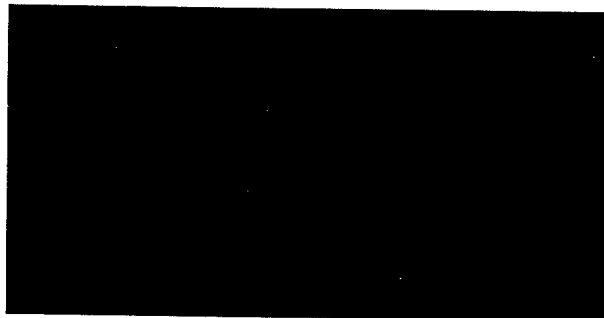
**Figure A-13: Mean deviation errors versus Heliocentric ecliptic longitude of Earth.** The three COBE/DIRBE bands are plotted with the mean error for one CIO day versus heliocentric ecliptic longitude of Earth. Band 5 shows the highest deviation as expected from the fit to the ISO spectrum of Figure A-5.



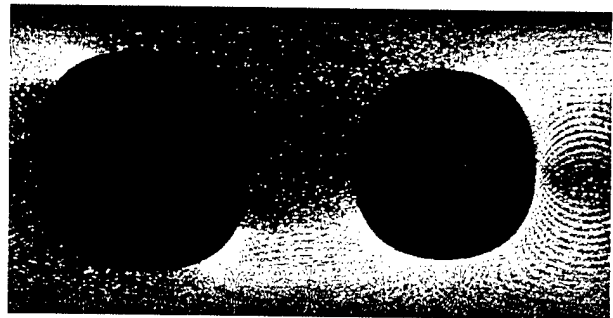
a) Data



b) Model

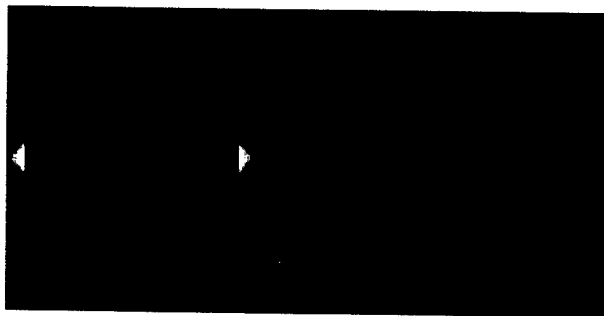


c) Residual

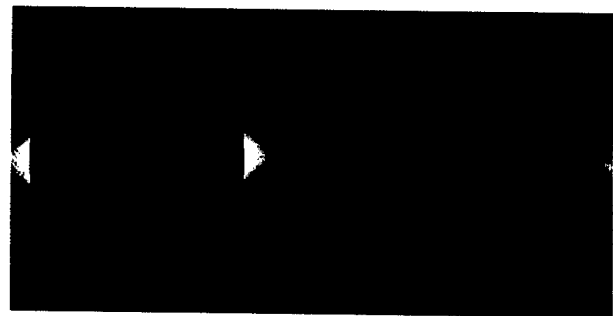


d) Percentage Error

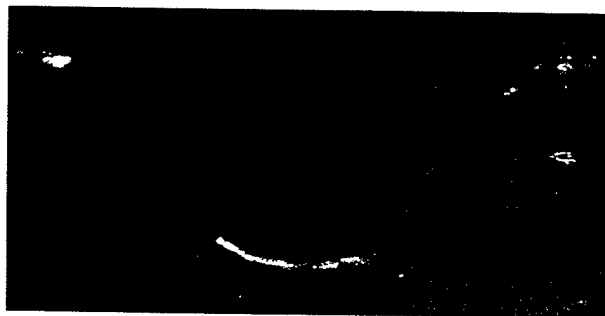
**Figure A-14: Day 90005 Band 4**



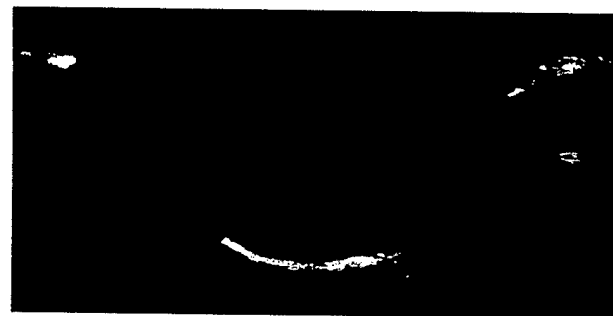
a) Data



b) Model



c) Residual



d) Percentage Error

**Figure A-15: Day 90005 Band 5**

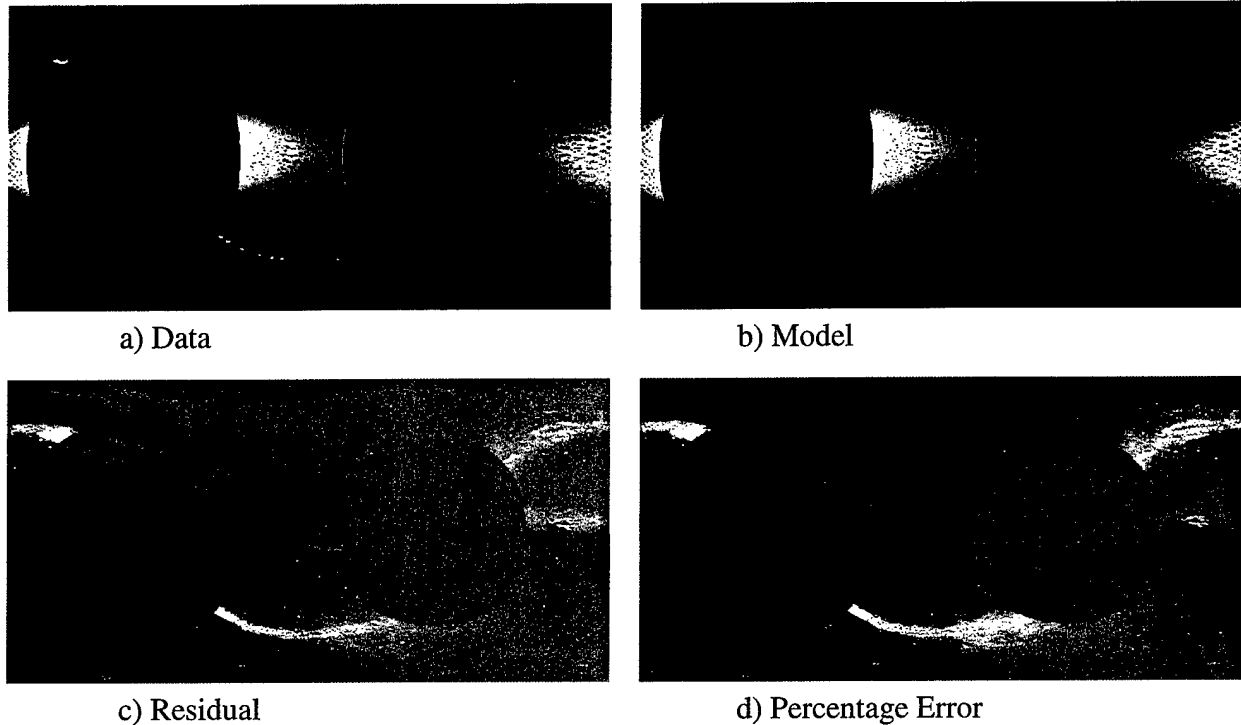
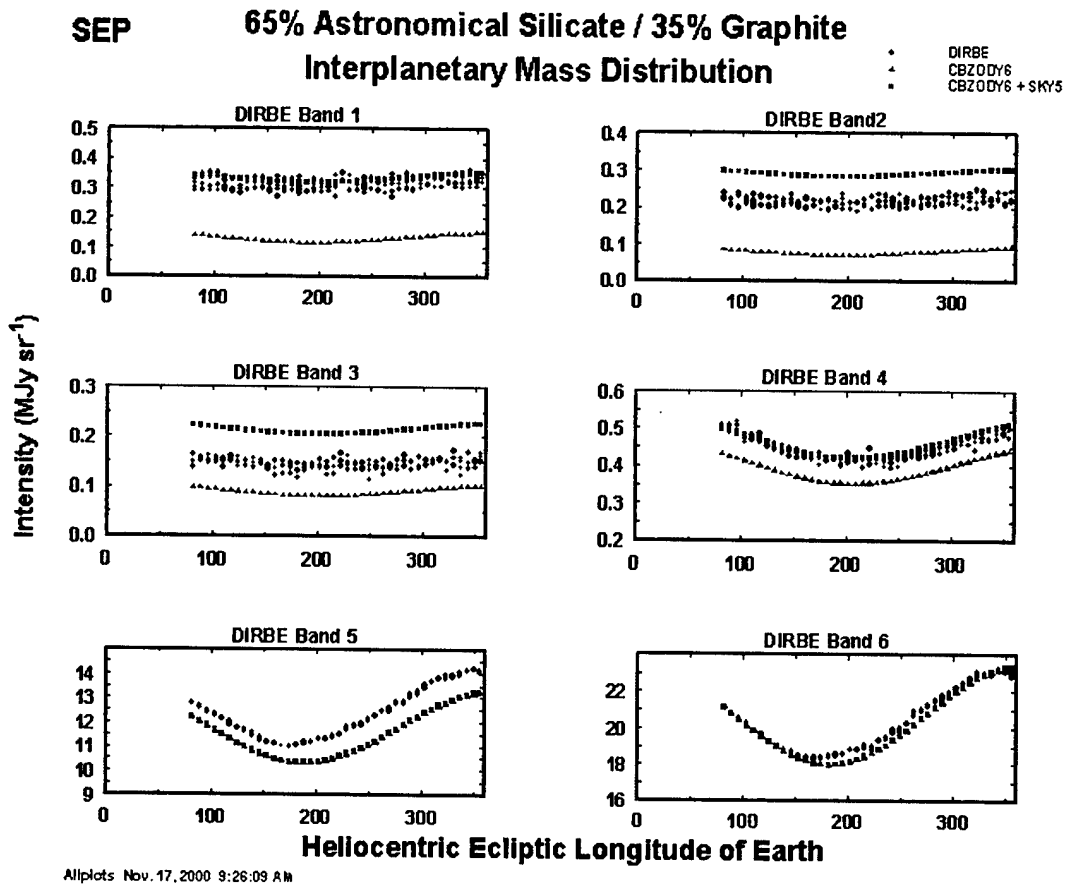


Figure A-16: Day 90005 Band 6

### A.5.8 South Ecliptic Pole (SEP)

During the COBE mission one of the early release products was observations of the South Ecliptic Pole (SEP). The initial data were 10 values representing the brightness seen in the 10 DIRBE bands. However, single values are insufficient to represent the zodiacal brightness, as the zodiacal light is a time-varying phenomenon. The poles of the ecliptic plane and the zodiacal cloud symmetry do not line up, which results in a slight sinusoidal variation of the brightness of the ecliptic pole. Figure A-17 shows the COBE data (Band 1 through 6) for observations of the SEP using the weekly skymap data. We have plotted the brightness data versus the heliocentric ecliptic longitude of the Earth. Bands 1, 2, and 3 show little sinusoidal variations. However, bands 4, 5, and 6 show a strong sinusoidal component. We also noted that the brightness at the SEP in bands 1 through 4 is higher than CBZODY6 predictions. In conjunction with Martin Cohen (1999), we obtained his SKY5 estimates of the SEP brightness due to unresolved stellar point sources.

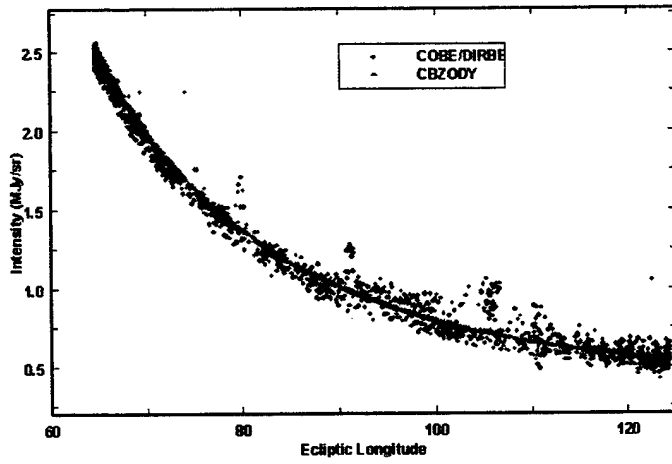


**Figure A-17: Final SEP fit.** The six COBE/DIRBE bands compared to a CBZODY6 + SKY4 fit.

### A.5.9 COBE CIO in-plane data

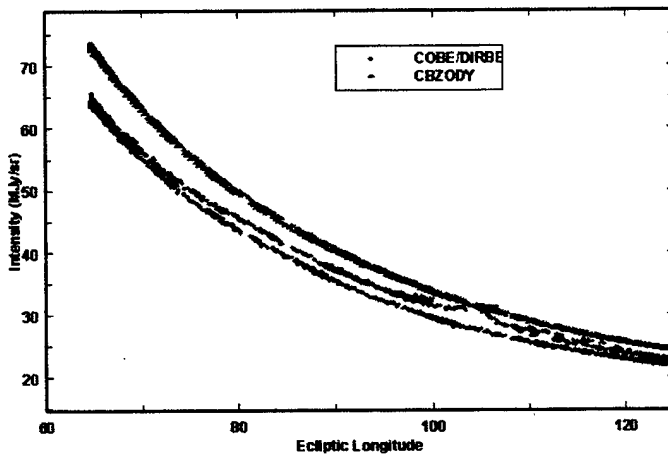
The in-plane data represent the zodiacal intensity in the ecliptic plane. The data of Figure A-18 have been extracted from the COBE CIO data. Three of the COBE bands are shown, Band 4 (4.4 $\mu$ m), Band 5 (12 $\mu$ m) and Band 6 (25 $\mu$ m).

**COBE/DIRBE Band 4**  
90005



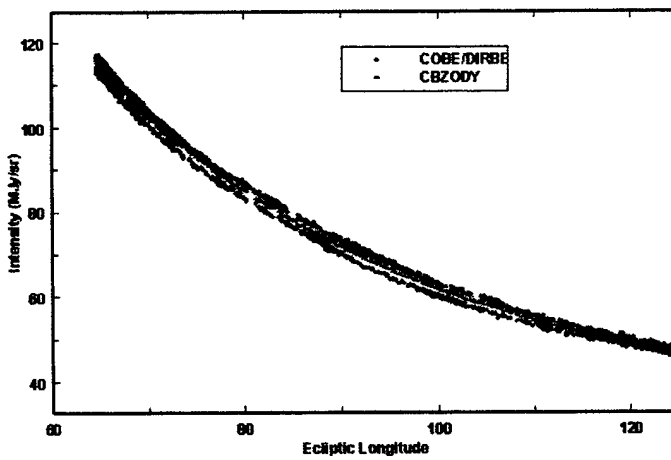
a) 90005 Band 4

**COBE/DIRBE Band 5**  
90005



b) 90005 Band 5

**COBE/DIRBE Band 6**  
90005



c) 90005 Band 6

**Figure A-18: In-plane fits to the CIO data.**

### A.5.10 COBE CIO Psuedo-Scans

Figure A-19 shows COBE pseudo-scans of constant elongation similar to IRAS Zodiacal Observation History File pole-to-pole scans. Again, the average parameter set has been used. These data are taken directly from the CIO data. One of the features of the CBZODY6 model is the Lorentzian out of plane density distribution. This feature does not show up well in other data plots.

In the plot, the solid line represents the COBE/DIRBE Band 5 ( $12\mu\text{m}$ ) data. The dashed line is the CBZODY6 model. The residual is represented by the solid line near an intensity of  $0.2 \text{ MJy sr}^{-1}$ . The residual has been multiplied by a factor of 10 for clarity.

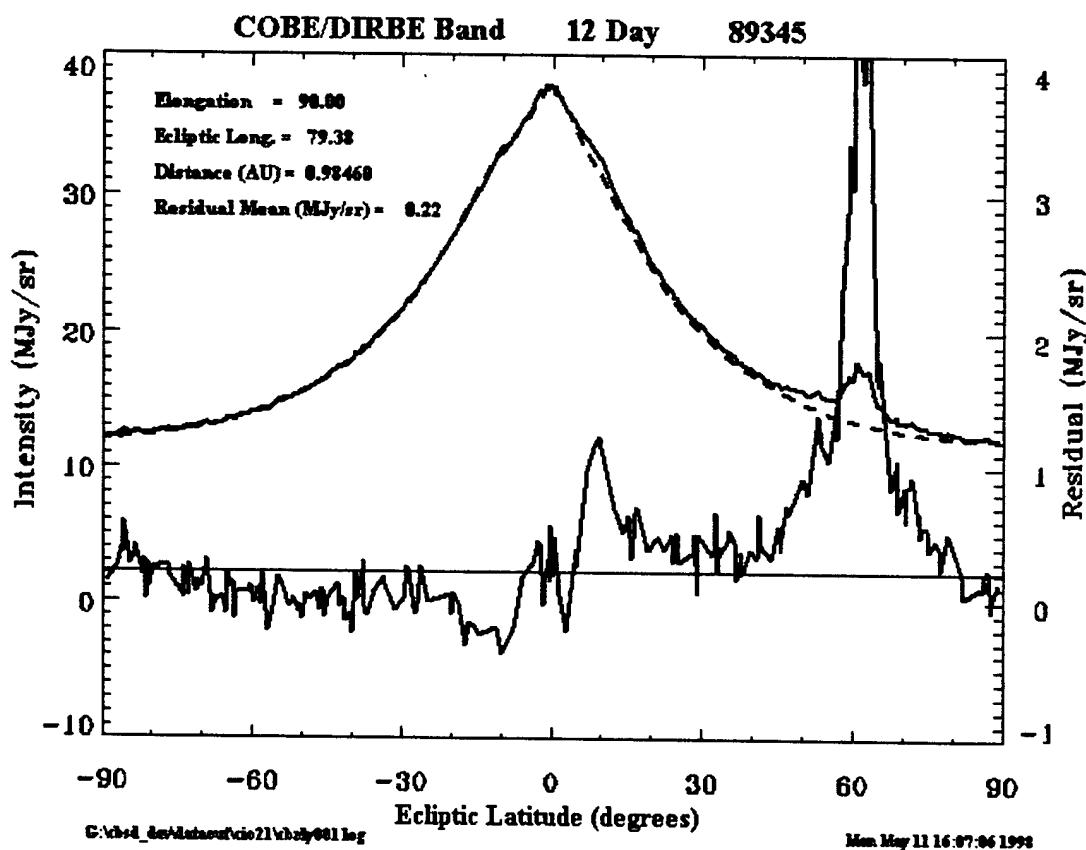


Figure A-19: Pole-to-Pole pseudo-scans. Band 5 pole-to-pole pseudo-scans for leading and trailing scans.

## A.6 Summary

The Air Force's CBSD code CBZODY6 accurately reproduces the spectrum and spatial (image) data of the zodiacal interplanetary dust cloud from 0.1 to 300 $\mu$ m. Spectral resolutions possible are limited to the spacing of the external volume emissivity database and are available at 0.1 or 0.01 $\mu$ m.

The CBZODY6 model simulations have been compared to IRAS, ZIP, MSX, COBE, and other small rocket and balloon data. The accuracy of the predicted flux can be stated to be within 10%.

There is still work that needs to be done with the CBZODY6 model. The composition of the dust cloud is poorly known. This limits the accuracy of the overall model.

One component of the zodiacal cloud model that has not been tested is the Gegenschein. The Hong (1985) function does have a strong backscatter component. While the Gegenschein has been visually observed and photographed we have not come across any observations that can directly test the CBZODY model. Therefore, backscatter should be tested in future versions of the CBZODY model.

While strides have been made to increase the execution speed of the model, two factors have changed. The speed of the average processor has increased markedly since the beginning of the program. At the same time, the complexity and expectation of the model has increased. Future development of CBZODY6 will have to stress efficiency while maintaining fidelity.

New datasets are being made available. The MSX zodiacal observations are now being made available. NASA's Project Stardust promises to return comet particles of Comet Wild-2 in 2006. The SIRTf mission, scheduled for launch in December 2001, is the next cryogenically cooled space observatory. SIRTf could provide further understanding of the zodiacal cloud such as small structure, time variability, and composition.



## References

- Bohren, C.F. and Huffman, D.F. (1983). *Absorption and Scattering of Light by Small Particles*, (New York: Wiley).
- Briggs, R. E., (1962). "Symposium: Astrometry I: The Steady-State Space Distribution of Meteoric Particles Under the Operation of the Poynting-Robertson Effect," *Astron. J.*, **67**, 710-723.
- Briotta, D. A., J. A. Piper, and J. R. Houck, (1976). *Rocket Infrared Spectroscopy of the Zodiacal Dust Cloud*, AFGL-TR-76-0236 (AD A034 054).
- Clark, F. O.; Torbett, M. V.; Jackson, A. A.; Price, S. D.; Kennealy, J. P.; Noah, P. V.; Glauddell, G. A.; Cobb, M, (1993). "The Out-of-Plane Distribution of Zodiacal Dust Near the Earth," *Astron. J.*, **105**, 976.
- Cohen, M., (1999). Private communication.
- Dermott, S. F., P. D. Nicholson, J. A. Burns, and J. R. Houck. (1984). "Origin of the Solar System Dust Bands Discovered by IRAS," *Nature*, **312**, 505
- Dermott, S.F., P. D. Nicholson, J. A. Burns and J. R. Houck. (1985). "Properties and Interaction of Interplanetary Dust," in IAU Colloquium #85, (eds. R. H. Giese and P. Lamy) (D. Reidel Pub. Co.) p395.
- Gray, D. F. (1976). *The Observation and Analysis of Stellar Photospheres* (New York: Wiley).
- Hauser, M. G.; Gillett, F. C.; Low, F. J.; Gautier, T. N.; Beichman, C. A.; Aumann, H. H.; Neugebauer, G.; Baud, B.; Boggess, N.; Emerson, J. P. (1984). "IRAS Observations of the Diffuse Infrared Background," *Astrophys. J.*, **278**, L15-L18.
- Kerker, M. (1969). *The Scattering of Light and other Electromagnetic Radiation*, (New York: Academic Press).
- Lang, K.R. (1980). *Astrophysical Formulae*, (New York: Springer-Verlag).
- Lehmann, H. and W. Häupl (1986). *AAS Photo-Bul.*, **43**, 5.
- Lienert, Ch. (1975). *Space Sci.Rev.*, **18**, 281.
- Leinert, C. and E. Grün (1990). "Interplanetary Dust, in Physics and Chemistry in Space," in *Space and Solar Physics 20*. (eds. Schwenn R. and Marsch E. eds.) – Springer, Berlin, Heidelberg, p. 207.
- Leinert, Ch.; Bowyer, S.; Haikala, L. K.; Hanner, M. S.; Hauser, M. G.; Levasseur-Regourd, A.-Ch.; Mann, I.; Mattila, K.; Reach, W. T.; Schlosser, W.; Staude, H. J.; Toller, G. N.; Weiland, J. L.; Weinberg, J. L.; Witt, A. N. (1998). "The 1997 reference of diffuse night sky brightness," *Astron. Astrophys. Supp.*, **127**, 1.
- Low, F. J.; Young, E.; Beintema, D. A.; Gautier, T. N.; Beichman, C. A.; Aumann, H. H.; Gillett, F. C.; Neugebauer, G.; Boggess, N.; Emerson, J. P. (1984). "Infrared Cirrus - New Components of the Extended Infrared Emission," *Astrophys. J.*, **278**, L19-L22.
- Meeus, J. (1996). *Astronomical Algorithms*, (William-Bell: Virginia).

- Reach, W. T., (1988). "Zodiacal Emission. I - Dust Near the Earth's Orbit," *Astrophys. J.*, **335**, 468.
- Reach, W. T.; Abergel, A.; Boulanger, F.; Desert, F.-X.; Perault, M.; Bernard, J.-P.; Blommaert, J.; Cesarsky, C.; Cesarsky, D.; Metcalfe, L.; Puget, J.-L.; Sibille, F.; Vigroux, L. (1996), "Mid-Infrared Spectrum of the Zodiacal Light," *Astron. Astrophys.*, **315**, L381-L384.
- Schmude, R. W. Jr. (1999). "Photoelectric Magnitude Measurements of the Zodiacal Light," *IAPPP Communications*, **75**, 24.
- Sykes, M. V. (1988). "IRAS Observations of Extended Zodiacal Structures," *Astrophys. J.*, **334**, L55.
- Sykes, M. V. (1990). "Zodiacal Dust Bands - Their Relation to Asteroid Families," *Icarus*, **85**, 267.
- Sykes, M. V., Greenberg, R., Dermott, S. F., Nicholson, P. D., Burns, J. A., and Gautier, T. N. (1989). "Dust Bands in the Asteroid Belt," in *Asteroids II*, eds. R. P. Binzel, T. Gehrels, and M. S. Matthews, (Tucson: U. of Arizona), p.336.
- van de Hulst, H. C. (1957), *Light Scattering by Small Particles* (New York: Wiley).

## **Appendix B: CBSKY4 Validation Summary**

### **B.1 Introduction**

The CBSD suite currently represents celestial phenomenology through independent software components each producing infrared signatures of one class of celestial objects. Each model computes the position and flux of celestial objects handled by that model. The components do not interact, and output is synthesized into a description of the real world celestial background through simple co-adding of fluxes with simple masking. The CBAMP model produces infrared signatures of the asteroids, moon, and planets. The CBZODY model produces infrared signatures arising from zodiacal dust in the solar system. The CBSKY4 model produces infrared signatures of point sources, most of which are part of our galaxy. Other components in progress produce signatures of HII regions, galaxies, planetary nebulae, celestial cirrus, and other extended sources that can have significant infrared flux values.

The CBSKY4 code runs as a stand-alone command line program, with no graphical interface. All user inputs are defined in text files. The CBSKY4.inp file is a Windows INI file format of sets of initialization variables, their values, and optional comment fields, all grouped under section headings for easy editing. There are no command line options or variables. The program uses input text files and binary data files built by the user when installing the software. These are described in the CBSD user manual. A separate reference manual provides detailed information about each input variable.

Alternatively, the CBSKY4 may be accessed through the CBSD control component that drives all the models and synthesizes their outputs into a single representation of the celestial background as a whole.

For additional information the reader is directed to Technical Report 9: Validation Report for the Celestial Background Scene Descriptor (CBSD) Stellar Point Source (CBSKY4) Model.

### **B.2 Model Validation Results**

The following sections outline our rationale for validation, and our qualitative and quantitative assessment of the performance of the model.

### **B.3 Predictive Validation of Stellar Distributions**

Validating that CBSKY4 accurately predicts a stellar distribution is the heart of this document. This involves comparing model output to the "real world" or "ground truth." For CBSKY4, Martin Cohen's SKY4 model is taken as truth, and the bulk of this effort is verifying that CBSKY4 produces the same statistical distributions of stars as the Cohen SKY4 model.

#### **B.3.1 SKY4 Description**

The Cohen SKY4 model is a stand-alone FORTRAN code that models the counts per magnitude bin for an arbitrary line-of-sight at any location in the sky. The code produces histograms of star counts per magnitude bin for arbitrary rectangular regions in the sky and for pre-defined bandpasses and arbitrary bandpasses. The code optionally outputs the star counts on a component or source basis for the following galactic structures:

- The disk
- The bulge
- The spheroid
- The spiral arms (including the 'local arm')
- The molecular ring, and
- The extragalactic sky (distant galaxies).

Other code features:

- The default solar displacement from the galactic plane (15 parsecs North) can be overridden.
- Surface brightness (flux describing extended sources including confused regions) can be output.
- Computation of total flux in an area (flux arising from all the stars in a region).
- Bandpass options: B, V, J, K, 2.4  $\mu\text{m}$ , 12  $\mu\text{m}$ , 25  $\mu\text{m}$ , 1565  $\text{\AA}$ , 1400  $\text{\AA}$ , 1660  $\text{\AA}$ , user-defined 2-30 micron response filter.

Star counts for giant molecular clouds (for the 12  $\mu\text{m}$  band or the 25  $\mu\text{m}$  band), galactic extinction, and absent regions are included in the modeling.

The output of Cohen's SKY4 is a set of text files. The file SKY4.OUT is a two-column text file. The first column is the magnitude or flux bins. The second column is the differential or cumulative Log(N) star counts. The Sky4.Log file is also a text file. The input parameter values are listed as well as numbers like the total FOV size in square degrees.

### **B.3.2 Cohen's Spectral Classes**

The spectral classification scheme used by CBSKY4 is based on the work of Martin Cohen (1993, 1994). Martin Cohen defined his spectral classification system for the program SKY4. Cohen's classification system includes 87 spectra templates. There are 33 normal stellar types; 42 types of AGB star, both oxygen and carbon rich; six types of objects that are distinct from others only by their midinfrared high luminosity; and six types of exotica including T Tau stars, HII regions, planetaries, and reflection nebulae. Their relationship to standard spectral types published in other catalogs is presented in Table B-1.

**Table B-1: Cohen Spectral Classification Types**

Cohen Number	Related Spectral Type	Cohen Number	Related Spectral Type	Cohen Number	Related Spectral Type
1	B0,1 V	30	YOUNG OB	59	AGB C 25
2	B2,3 V	31	A-G I-II	60	AGB CI 01
3	B5 V	32	K-M2 I-II	61	AGB CI 03
4	B8-A0 V	33	M3-4 I-II	62	AGB CI 05
5	A2-5 V	34	AGB M 01	63	AGB CI 07
6	F0-5 V	35	AGB M 03	64	AGB CI 09
7	F8 V	36	AGB M 05	65	AGB CI 11
8	G0-2 V	37	AGB M 07	66	AGB CI 13
9	G5 V	38	AGB M 09	67	AGB CI 15
10	G8-K3 V	39	AGB M 11	68	AGB CI 17
11	K4-5 V	40	AGB M 13	69	AGB CI 19
12	M0-1 V	41	AGB M 15	70	AGB CI 21
13	M2-3 V	42	AGB M 17	71	AGB CI 23
14	M4-5 V	43	AGB M 19	72	AGB CI 25
15	M late V	44	AGB M 21	73	AGB CI 27
16	F8-G2 III	45	AGB M 23	74	AGB CI 29
17	G5 III	46	AGB M 25	75	AGB CI 31
18	G8 III	47	AGB C 01	76	X 1E
19	K0,1 III	48	AGB C 03	77	X 1A
20	K2,3 III	49	AGB C 05	78	X 2
21	K4,5 III	50	AGB C 07	79	X 3
22	M0 III	51	AGB C 09	80	X 4
23	M1 III	52	AGB C 11	81	X 5
24	M2 III	53	AGB C 13	82	PN BLUE
25	M3 III	54	AGB C 15	83	PN RED
26	M4 III	55	AGB C 17	84	RN BLUE
27	M5 III	56	AGB C 19	85	RN RED
28	M6 III	57	AGB C 21	86	H II REG
29	M7 III	58	AGB C 23	87	T TAURI

Every category of source has its own set of absolute magnitudes in the hardwired bandpasses and its own dispersion of M12 and its own individual scale height and volume density in the local solar neighborhood. Some sources may be absent from specific galactic structures. The galactic arms and ring have higher populations of high-mass stars whereas the galactic halo does not.

### **B.3.3 Log(N) vs. Log(S) Plots**

#### **B.3.3.1 Brief History of Star Count Techniques**

Star counting and star cataloging of positions and magnitudes of bright stars date back to antiquity; however, only in the last few hundred years has star counting been used to infer the shape and size of our galaxy. A very brief timeline of major events in the history of star counting or "star gauging" is presented in Table B-2.

**Table B-2: Timeline of Star Count Techniques**

**Year**      **Events**

2 - 1600      The principal catalog used for star maps until 1600 was compiled by Claudius Ptolemy in the second century A.D. This catalog contains the positions of 1028 stars, and it first appeared in print in this edition of Ptolemy's authoritative *Almagest*, the basic ancient work on astronomical theory.

<del>Antecedens carum</del>	1 26 10	M 3 0 50	4
<del>Lucida que est in pede sinistro: et est communis et eaque</del>	1 19 10	M 3 1 30	1
<del>Que est sup declinatioe ea ad septentrione: et est sup calcaneum</del>	1 21 0	M 3 0 15	4 .2m.
<del>Que est super calcaneum sinistrum exterius</del>	1 23 20	M 3 1 10	4
<del>Que est super genu dextrum septentrionale</del>	1 0 10	M 3 3 30	3
<del>Starum triginta octo stellarum in magnitudine prima sunt due. in secunda quatuor. in tertia octo. in quarta quindecim. in quinta tres. in sexta quinq. et nebulosa una.</del>			
<del>(Stellatio Sinist.)</del>		<del>Imago Trichinae</del>	
<del>Que est post illa que est in pede sublimati sine audacia sup principi flammis</del>	1 18 20	M 3 1 50	4
<del>Que est declinatio hac ad sept. et est tortuositate apud pedem et crura sub</del>	1 18 50	M 2 8 15	4
<del>Sequens vultu strinas que sunt post barre</del>	1 18 0	M 2 9 50	4

This detail from a 1515 Ptolemy's catalog shows the last few stars of Orion, and the beginning of the entry for Eridanus. In the second line from the top, Ptolemy catalogs the star that will later become known as Rigel. He describes it as "The bright star that is in the left foot in common with the water", gives its longitude and latitude, and assigns a magnitude of "1".

1738 - 1822      William Herschel was the first to use star counts to construct a model of the universe. He counted the number of stars he could see in different directions down to a particular limiting magnitude. His model describes the galaxy as a thin lens-like structure bulging at the center. His statement that "the galactic plane is to our Milky Way what the plane of the ecliptic is to the solar system" was a profound contribution.

1896 - 1900      The Herschel survey resulted in the publication of the *Cape Photographic Durchmusterung*, listing positions and magnitudes for 454,875 stars on the Southern Hemisphere.

1904      Studying the proper motions of stars, Kapteyn found evidence that these proper motions were not random, as was generally accepted in that time. Surprisingly, the stars could be divided into two streams, apparently moving in opposite directions. This discovery ultimately led to the finding of galactic rotation by Lindblad and Oort.

1922      J. Kapteyn modeled star counts for 206 selected uniformly distributed areas of the sky. Counting stars down to the 17<sup>th</sup> apparent magnitude, he constructed a model of the Milky Way that resembled a flattened ellipsoid of revolution with a diameter 5 times the central thickness. He described the Milky Way as a lens-shaped 'island universe' of which the density decreased away from the center. This galaxy was thought to be 40,000 light years in size, the sun being relatively close (2,000 light years) to its center. He estimated that there are  $4.7 \cdot 10^{10}$  stars in the galaxy, and that the central stellar density is 45 stars per pc<sup>3</sup>.

mid-1920s      Using the 100 inch Hooker Telescope at Mount Wilson, then the largest telescope in the world, astronomer Edwin Hubble identified Cepheid variable stars in the Andromeda Galaxy (M31). These stars allowed Hubble to show that the distance to M31 was greater than even Shapley's proposed extent of our Milky Way galaxy. Therefore M31 was a galaxy much like our own.

1928      F. H. Sears counted the number of stars per square degree.

1930      R. J. Trumpler quantifies the interstellar absorption and reddening of starlight by cosmic dust, making it possible for precise distance measurements of galactic objects. Combined with an increased understanding of the distances and distribution of globular clusters ultimately led to the acceptance that the size of our Milky Way Galaxy had indeed been seriously underestimated and that the Sun was not close to the center. This discovery increased the estimate of the galaxy's size to 100,000 light years, with the sun replaced to a distance of 30,000 light years from its center.

1937      Hubble publishes a paper that includes references to two fainter points on the  $N(m)$  count curve determined at Mount Wilson plus the important  $N(m)$  additional data point from Mayall's (1934) Ph.D. survey. A principal part of the analysis centers on the effects of red shifts on the observed  $N(m)$  distribution and the corrections required due to the redshift effect. Hubble concluded that his observed  $\log N(m)$  distribution showed a large departure from Euclidean geometry, provided that the effect of redshifts on the apparent magnitudes was calculated as if the redshifts were due to a real expansion. A different correction is required if no motion exists, the redshifts then being due to an unknown cause. Hubble believed that his count data gave a more reasonable result concerning spatial curvature if the redshift correction was made assuming no recession. To the very end of his writings he maintained this position, favoring (or at the very least keeping open) the model where no true expansion exists, and therefore that the redshift "represents a hitherto unrecognized principle of nature".

Based on the star catalogs and star count our present view of the Milky Way galaxy is:

- ◆ The main portion of stars forms a flat disk about 30 kpc in diameter.
- ◆ This disk contains spiral arms.
- ◆ The outer portions of the center of the galaxy can be viewed as bright swarms of stars in Scorpio and Sagittarius.
- ◆ The disk is surrounded by a considerably less flattened halo, which contains the globular clusters and certain types of individual stars. Halo objects, sometimes referred to as high velocity stars, follow elliptical orbits about the galactic center; their relative velocities with respect to the Sun are 100-300 km/s.
- ◆ Our solar system is about 9 kpc from the center of the galaxy. The Sun orbits the galactic center every ~250 million years at a velocity of ~220 km/s.
- ◆ The galactic center is hidden from Earth's view by thick, dark interstellar clouds.
- ◆ The whole system is about  $2 \cdot 10^{11}$  solar masses.

### B.3.3.2 Magnitude Defined

CBSKY4 output magnitudes are apparent magnitudes. Apparent magnitude is the measure of how bright a star appears, and magnitude differences between stars measure the relative brightness of stars. The most negative magnitude numbers correspond to the brightest objects, while the largest positive numbers correspond to the faintest objects.

Apparent magnitudes are defined for a specified spectral region. Astronomers traditionally speak of visual magnitudes or brightness as the human eye would perceive it. Magnitudes output in CBSKY4 are reported for the spectral region defined by the user.

The following formula relates magnitude and brightness:

$$(m_2 - m_1) = 2.5 \log(b_1/b_2)$$

$$(m_1 - m_2) = -2.5 \log(b_1/b_2)$$

where,  $m_1$  and  $b_1$  are the magnitude and brightness of object 1 and  $m_2$  and  $b_2$  are the magnitude and brightness of object 2.

To convert magnitudes to brightness values, one needs a reference object, typically reported as the flux at magnitude zero. Using,

$$m = -2.5 \log(F / F_0)$$

with,  $F_0$  being the flux at magnitude zero, and  $F$  being the flux of the star, the magnitude,  $m$ , of the star can be computed. Conversely, the flux can be computed from the magnitude:

$$F = F_0 \cdot 10^{-m/2.5}$$

Table B-3 illustrates the relative differences in apparent magnitudes of objects through familiar examples.

**Table B-3: Comparison of Apparent and Absolute Magnitudes**

<b>Object</b>	<b>Apparent Visual Magnitude</b>	<b>Absolute Magnitude</b>
The Sun	-26.8	4.8
100 Watt Bulb at 3 m	-18.7	66.3
Full Moon	-12.5	32
Venus (at brightest)	-4.4	28
Sirius (brightest star)	-1.5	1.4
Alpha Centauri (closest star)	-0.04	4.4
Andromeda Galaxy (farthest seeable object)	3.5	-21
Faintest naked eye stars	6-7	-----
Faintest star visible from Earth telescopes	~25	-----

The absolute magnitude is a measure of the energy produced by a star or object. It is defined as the apparent magnitude of the star if the star were located at a standard distance of 10 parsecs from the observer. Absolute magnitudes can be inferred from the spectrum of a star.

Apparent magnitude values are the result of both the intrinsic brightness of the star (which is related to its internal energy production) and the effect of distance (which has nothing to do with the intrinsic structure of the star). The inverse square law of brightness can be used to infer distances to stars. The difference between the absolute magnitude,  $M$ , and the apparent magnitude,  $m$ , is called the distance modulus ( $m - M$ ). The formula:

$$m - M = 5.0 \log (D/10.0)$$

is used where  $D$  is the distance between the observer and the object in parsecs. If a star's distance cannot be computed from parallax or other means, this formula is often used by assuming an absolute magnitude for its spectral type.

The apparent magnitude, spectral type, luminosity and distance from Earth of the 20 brightest visible stars are provided in Table B-4.



**Table B-4: The 20 (Apparent) Brightest Stars in the Sky (not including the Sun).**

Common Name	*Mag	Luminosity [Solar Units]	Distance [Light Years]	Spectral Type	Proper Motion [arcsec /year]	RA [Hr Min]	Dec [Deg Min]
Sirius ( $\alpha$ CMa)	-1.46	40	9	A1V	1.33	06 45.1	-16 43
Canopus ( $\alpha$ Car)	-0.72	1,500	98	F0I	0.02	06 24.0	-52 42
Alpha Centauri	-0.04	2	4	G2V	3.68	14 39.6	-60 50
Arcturus ( $\alpha$ Boo)	0.00	100	36	K2III	2.28	14 15.7	+19 11
Vega ( $\alpha$ Lyr)	0.03	50	26	A0V	0.34	18 36.9	+38 47
Capella ( $\alpha$ Aur)	0.08	200	46	G5III	0.44	05 16.7	+46 00
Rigel ( $\beta$ Ori)	0.12	80,000	815	B8Ia	0.00	05 12.1	-08 12
Procyon ( $\alpha$ Cmi)	0.38	9	11	F5IV-V	1.25	07 39.3	+05 13
Betelgeuse ( $\alpha$ Ori)	0.0 - 0.9	100,000	500	M2Iab	0.03	05 55.2	+07 24
Achernar ( $\alpha$ Eri)	0.46	500	65	B3V	0.10	01 37.7	-57 14
Beta Centauri		9,300	300	B1III	0.04	14 03.8	-60 22
Altair ( $\alpha$ Aql)	0.77	10	17	A7IV-V	0.66	19 50.8	+08 52
Aldeberan ( $\alpha$ Tau)	0.85	200	20	K5III	0.20	04 35.9	+16 31
Spica ( $\alpha$ Vir)	0.98	6,000	260	B1V	0.05	13 25.2	-11 10
Antares ( $\alpha$ Sco)	0.96	10,000	390	M1Ib	0.03	16 29.4	-26 26
Pollux ( $\beta$ Gem)	1.14	60	39	K0III	0.62	07 45.3	+28 02
Fomalhaut ( $\alpha$ PsA)	1.16	50	23	A3V	0.37	22 57.6	-29 37
Deneb ( $\alpha$ Cyg)	1.25	80,000	1,400	A2Ia	0.00	20 41.4	+45 17
Beta Crucis	1.25	10,000	490	B0.5IV	0.05	12 47.7	-59 41
Regulus ( $\alpha$ Leo)		150	85	B7V	0.25	10 08.3	+11 58

Source: Fraknoi, Morrison, and Wolff, Appendix 11

\* except Magnitude values source: <http://www.krysstal.com/brightest.html> (note: This web site has a different set of 20 brightest stars, and the values for distance, luminosity, RA/Dec, are also different from those provided by Fraknoi, Morrison, and Wolff.

### B.3.3.3 The Use of Log(N) vs. Log(S) Plots

The stellar density of the sky for a given sky region is defined by the Log(N) vs. Log(S) values. The Log(N) is the logarithm of the number of stars in a given magnitude bin; the Log(S) is the logarithm of the flux, or the magnitude of the stars. Further, the Log(S) values are quantized into bins of equal (apparent) magnitude.

For a cumulative Log(N) vs. Log(S) plot, the x-axis is the magnitude bin and the y-axis is the logarithm of the number of stars brighter than or equal to that magnitude. The curve is the logarithm of the cumulative histogram of star counts.

For a differential Log(N)/m vs. Log(S) plot, the x-axis is the magnitude bin and the y-axis is the number of stars per magnitude bin for that magnitude. It is not a histogram of the number of stars in that magnitude bin.

For validating the stellar distributions produced by CBSKY4, Log(N) vs. Log(S) plots are created overlaying the SKY4 results (our "truth" data) with the CBSKY4 results for a given region and bandpass and other code parameters. The plots are visually compared to subjectively determine that CBSKY4 is reproducing SKY4 stellar densities.

Unless otherwise noted, the CBSKY4 model was run for statistical stars (including molecular clouds) only, with real or catalog stars not included. While many bandpasses were compared for select regions, the majority of the comparisons were run for the K and the 12  $\mu\text{m}$  fiducial bands.

### B.3.4 Validation Results For Select Regions

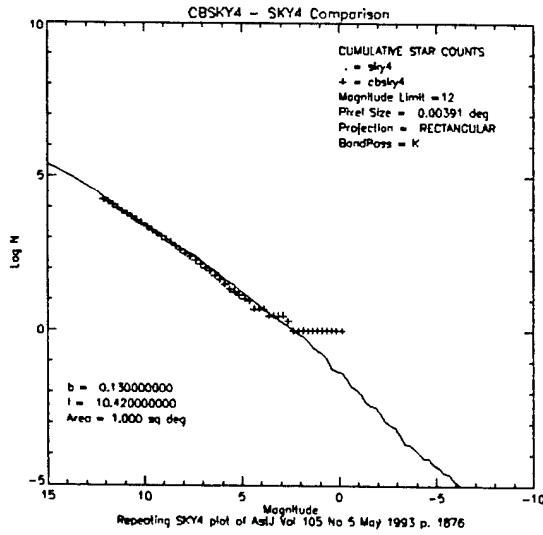
The set of validation regions discussed in this section were selected on the basis of their inclusion in Martin Cohen's publications about the SKY4 model improvements. These regions are presumed to have significant features in the bandpasses and for the FOV size reported. For all of these regions, two pre-defined bands were selected as the basis for all star distribution validations. The two fiducial bands chosen were the K and the 12  $\mu\text{m}$  bands.

Regions in Cohen (1993) were first selected (Table B-5). The following table lists these regions and parameters used for the validation. Comparison plots were generated for the K band and for the 12  $\mu\text{m}$  band.

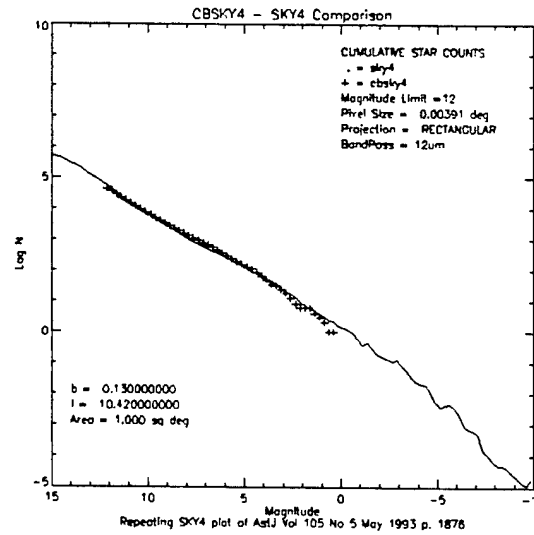
**Table B-5: May 1993 Test Regions (K and IRAS Band 1)**

Galactic Longitude [degrees]	Galactic Latitude [degrees]	Field-of-Regard [square degrees]
90.0	90.0	1.0
80.0	0.0	10.0
0.08	0.02	1.0
19.93	0.46	1.0
10.42	0.13	1.0
29.26	0.08	1.0
39.96	0.07	1.0
59.7	0.09	1.0
49.68	0.16	1.0

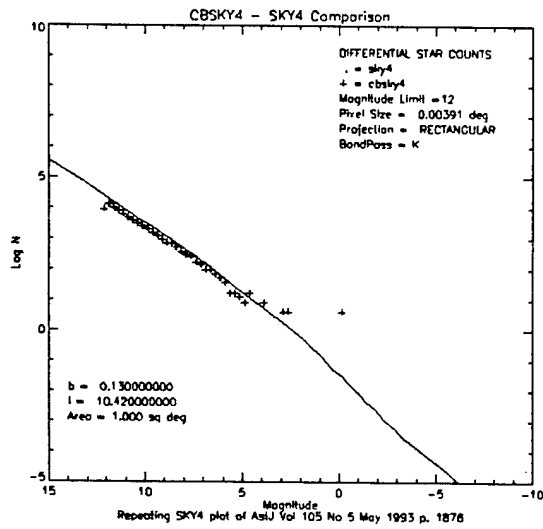
The output of the  $l=10.43$   $b=0.13$  case is shown in the Figure B-1. As  $\text{Log}(N)$  approaches zero, the CBSKY4 model is confounded by fractional star counts. Unable to place a fraction of a star, when  $\text{Log}(N)$  becomes less than or equal to zero, CBSKY4 assigns a single star to a single bright magnitude bin so that the  $\text{Log}(N=0)$  magnitude is the same on both curves. The results for the K band image below show the single bright star placement. These curves show excellent agreement between CBSKY4 and SKY4 statistical stars.



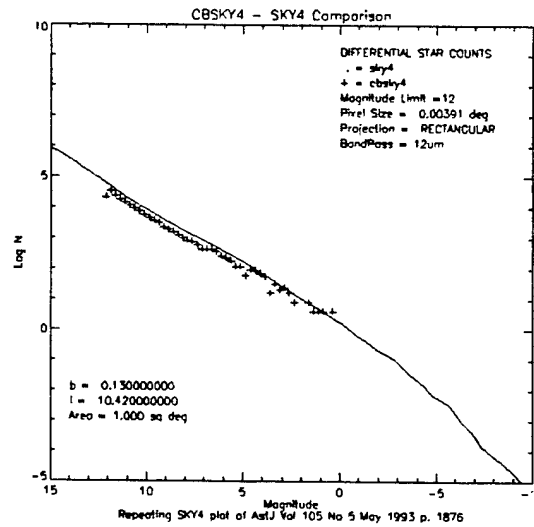
a) Cumulative star counts for the K band.



b) Cumulative star counts for the IRAS Band 1.



c) Differential star counts for the K band.



d) Differential star counts for the IRAS Band 1.



whole sky min = 3.4142E-018 W/CM2  
 whole sky max = 1.2718E-013 W/CM2  
 image total = 4.9219E-014 W/CM2  
 image min = 0.0000E+000 W/CM2  
 image max = 1.8455E-014 W/CM2  
 image size = 258 x 258 pixels  
 BandPass = K

e) The entire sky (left) in the K band along with the test case region indicated and zoomed.



whole sky min = 1.8325E-022 W/CM2  
 whole sky max = 1.0050E-014 W/CM2  
 image total = 8.4227E-015 W/CM2  
 image min = 0.0000E+000 W/CM2  
 image max = 3.9383E-016 W/CM2  
 image size = 258 x 258 pixels  
 BandPass = 12um

f) The entire sky (left) in the IRAS Band 1 along with the test case region indicated and zoomed.

Figure B-1: Output for the  $l=10.43$   $b=0.13$  test case.

The next set of validation regions were regions used in Cohen (1994). The following table lists the regions and parameters used for the validation. Note that Cohen's paper uses different bandpasses to describe the new ultraviolet extensions to his code; however, since this validation report focuses on the K and 12  $\mu\text{m}$  bands, the bandpasses used here are different in some cases. Comparison plots were generated for the bands listed in Table B-6.

**Table B-6: February 1994 Test Regions**

<b>Galactic Longitude (deg.)</b>	<b>Galactic Latitude (deg.)</b>	<b>Field-of- Regard (sq. deg)</b>	<b>Bandpass</b>
80.0	0.0	10.0	25 $\mu\text{m}$
107.5	1.25	22.49	12 $\mu\text{m}$
1.00	-3.9	0.9977	B
1.00	-3.9	0.9977	V
342.0	-70.0	0.3420	12 $\mu\text{m}$
73	55	0.5736	12 $\mu\text{m}$
223.0	-52.0	0.6157	12 $\mu\text{m}$
342.0	-70.0	2.241	12 $\mu\text{m}$
194.0	-60.0	3.277	12 $\mu\text{m}$
73.0	55.0	3.759	12 $\mu\text{m}$
223.0	-52.0	4.035	12 $\mu\text{m}$
345.0	-43.5	4.754	12 $\mu\text{m}$
333.0	-13.0	6.386	12 $\mu\text{m}$
5.50	-10.0	6.454	12 $\mu\text{m}$
83.50	-9.0	6.43	12 $\mu\text{m}$

### B.3.5 Validation Results For Zoom-In On Selected Confused Regions

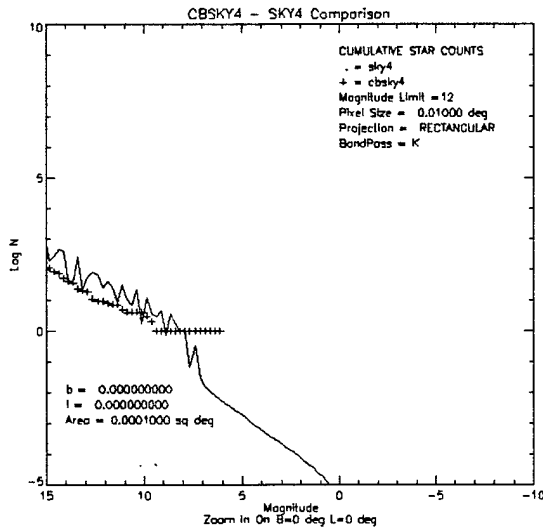
The code was tested for its ability to reproduce statistics in confused regions from very large FOV to very small FOV. The code positional accuracy is reported to be 2 arc seconds. At that resolution, most FOV will have stellar densities of less than one star. Each line-of-sight in Table B-7 was run for a single pixel with the following angular extents (in degrees): {10, 5.555, 1, .5555, 0.1, 0.05555, 0.01, 0.005555, 0.001, 0.0005555} and in all cases, smaller FOV produced fewer than one star. Most FOV produced fewer than one star at the 0.001 degree angular extent. The K band and IRAS Band 1 runs were made for the following central lines-of-sight. A total of 120 comparisons were made (6 centers, 2 bands, 10 FOV) for zooming in on a confused region.

**Table B-7: Confused-Region Centers for Zoom-In**

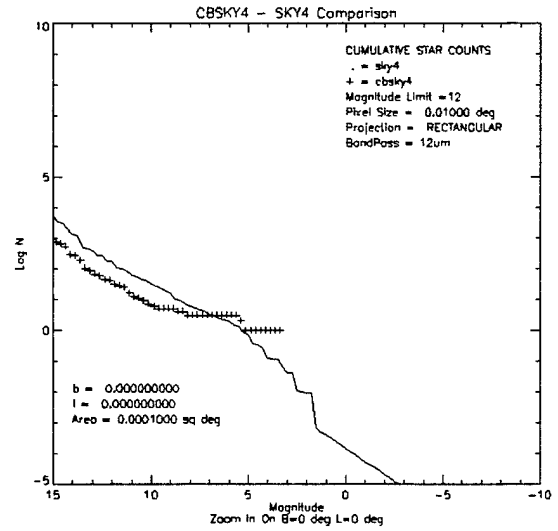
<u>Galactic Latitude [degree]</u>	<u>Galactic Longitude [degree]</u>
3.0	0.0
3.0	28.0
-3.0	0.0
-3.0	28.0
0.0	0.0
0.0	28.0

The Figures B-2 and B-3 show that the CBSKY4 model mirrors Cohen's SKY4 results even for a very small FOV on the galactic center.

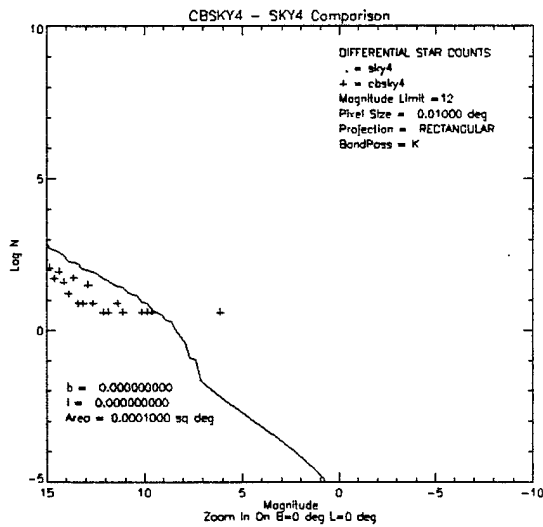
At small fields of regard at  $l = 28^\circ$  and  $b = 0^\circ$ , CBSKY4 provides star counts closely matched to Cohen's SKY4 as shown in the Figure B-3.



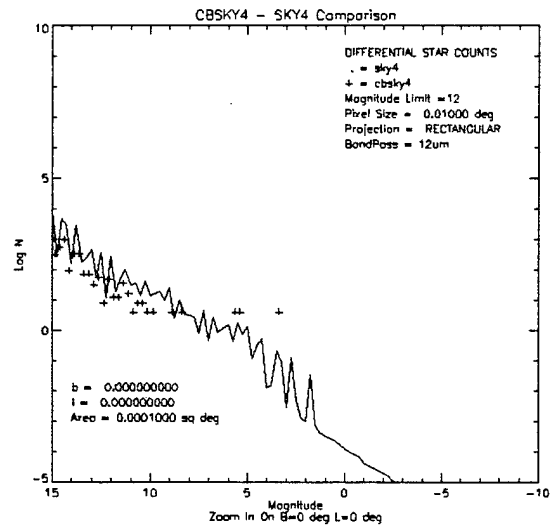
a) Cumulative star counts for the K band.



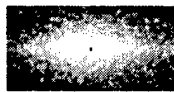
b) Cumulative star counts for the IRAS Band 1.



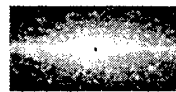
c) Differential star counts for the K band.



d) Differential star counts for the IRAS Band 1.



whole sky min = 3.4142E-018 W/CM2  
 whole sky max = 1.2716E-013 W/CM2  
 image total = 7.7017E-017 W/CM2  
 image min = 7.7017E-017 W/CM2  
 image max = 7.7017E-017 W/CM2  
 image size = 1 x 1 pixels  
 BandPass = K

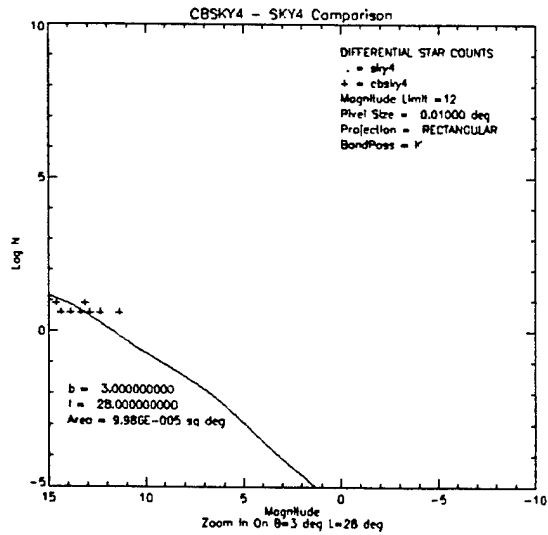


whole sky min = 1.8325E-022 W/CM2  
 whole sky max = 1.0050E-014 W/CM2  
 image total = 3.5200E-017 W/CM2  
 image min = 3.5200E-017 W/CM2  
 image max = 3.5200E-017 W/CM2  
 image size = 1 x 1 pixels  
 BandPass = 12um

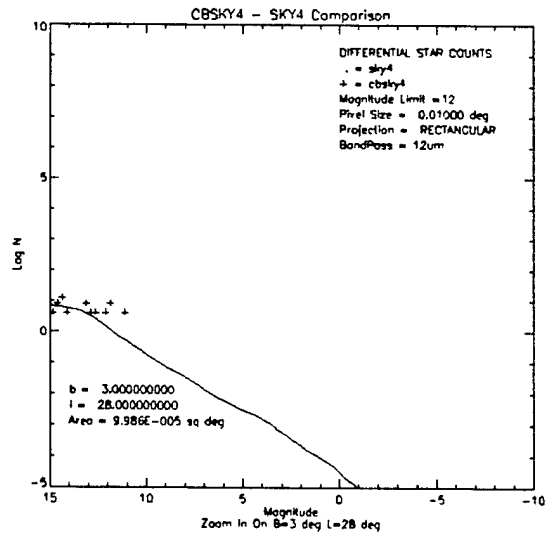
e) The entire sky (left) in the K band along with the test case region indicated and zoomed.

f) The entire sky (left) in the IRAS Band 1 along with the test case region indicated and zoomed.

Figure B-2: Small field-of-view looking at the Galactic Center.



a) Differential star counts for the K band.



b) Differential star counts for the IRAS Band 1.



whole sky min = 3.4142E-018 W/CM2  
 whole sky max = 1.2718E-013 W/CM2  
 Image total = 1.2348E-018 W/CM2  
 Image min = 1.2348E-018 W/CM2  
 Image max = 1.2348E-018 W/CM2  
 Image size = 1 x 1 pixels  
 BandPass = K

c) The entire sky (left) in the K band along with the test case region indicated and zoomed.



whole sky min = 1.8325E-023 W/CM2  
 whole sky max = 1.0050E-014 W/CM2  
 Image total = 7.5619E-020 W/CM2  
 Image min = 7.5619E-020 W/CM2  
 Image max = 7.5619E-020 W/CM2  
 Image size = 1 x 1 pixels  
 BandPass = 12um

d) The entire sky (left) in the IRAS Band 1 along with the test case region indicated and zoomed.

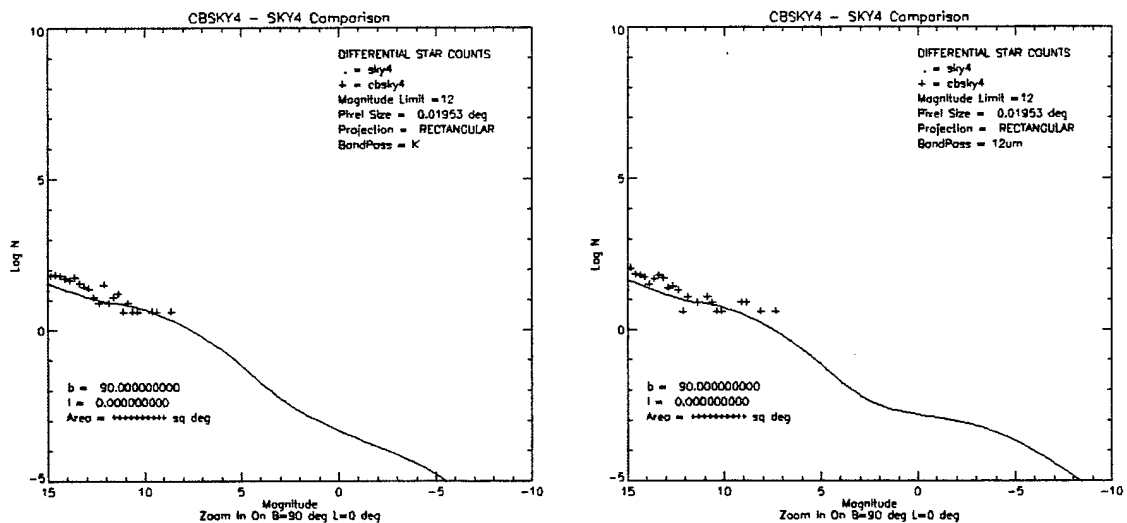
Figure B-3: Small fields of regard at  $l = 28^\circ$  and  $b = 0^\circ$

### B.3.6 Galactic North and South Poles

The CBSKY4 code was tested for its ability to reproduce statistics in stressing regions from very large FOV to very small FOV. The CBSKY4 positional accuracy is 2 arc seconds. At that resolution, most FOV will have stellar densities of less than one star. Each line-of-sight in Table B-8 was run for a single pixel with the following angular extents (in degrees): {10, 5, 1, 0.5}. Figure B-4 shows the agreement at the Galactic North Pole for a pixel 5 degrees on a side. As the region size decreases, Cohen's SKY4 produces only fractional stars. The area field doesn't display because the center is on the pole ( $\cos(90^\circ) = 0$ ). The Galactic North Pole region had no stars in the 0.5 degree field. The K band and 12 $\mu$ m band runs were made for the following central lines-of-sight. All were run using the Galactic coordinate system option.

**Table B-8: Galactic Poles For Zoom-In**

Galactic Latitude [degree]	Galactic Longitude [degree]	Location
90.0	0.0	Galactic North Pole
-90.0	0.0	Galactic South Pole



a) Differential star counts for the K band.

b) Differential star counts for the IRAS Band 1.

**Figure B-4: Small field-of-regard at the Galactic North Pole.**

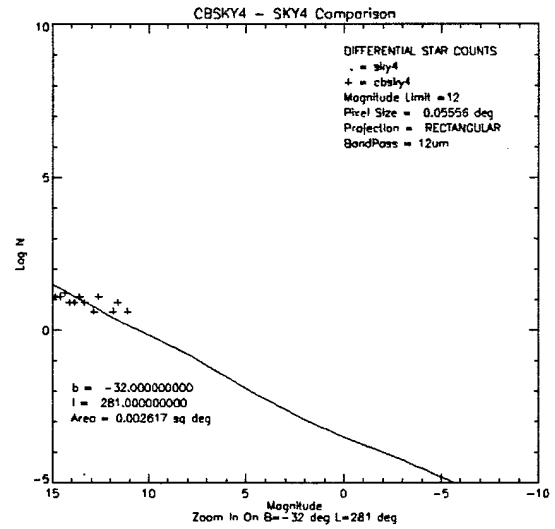
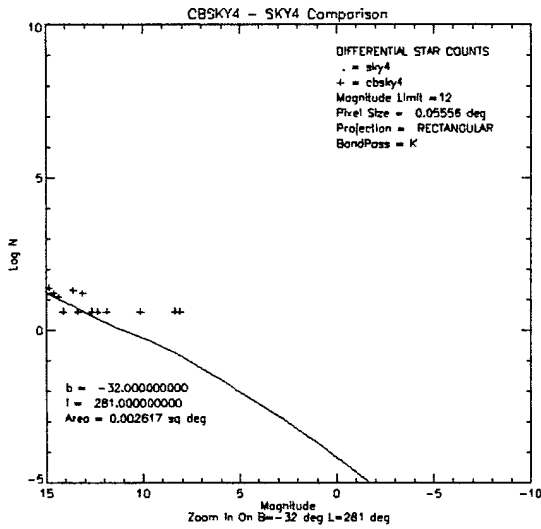


### B.3.7 LMC/SMC Confused Region

The CBSKY4 code was tested for its ability to reproduce statistics in stressing high star density or confused regions from very large FOV to very small FOV. The K band and 12  $\mu\text{m}$  band runs were made for the following central lines-of-sight, centered in the Large Magellanic Cloud and the Small Magellanic Cloud (Table B-9). All were run using the galactic coordinate system option. The comparisons of Figure B-5 once again illustrate the excellent agreement between CBSKY4 and Cohen's SKY4.

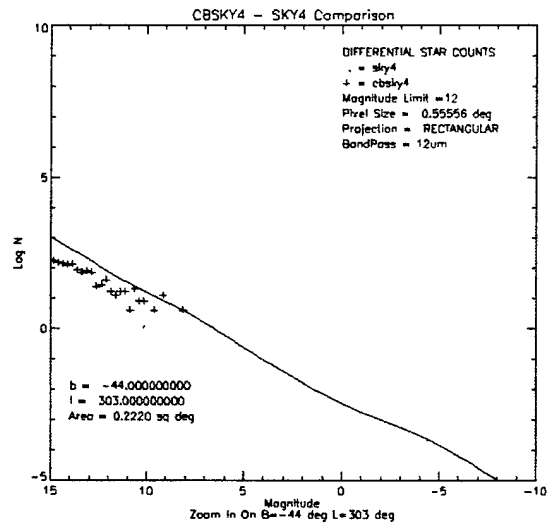
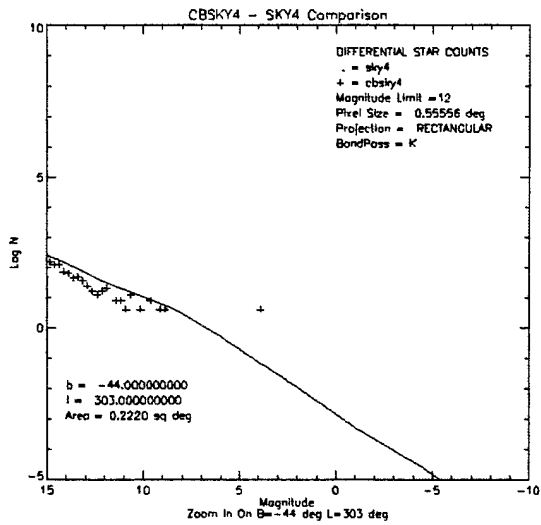
**Table B-9: Confused Regions For Zoom-In**

<b>Galactic Latitude [degree]</b>	<b>Galactic Longitude [degree]</b>	<b>Approx. Location</b>
-32	281	Large Magellanic Cloud
-44	303	Small Magellanic Cloud



a) Differential star counts for the K band for the LMC.

b) Differential star counts for the IRAS Band 1 for the LMC.



c) Differential star counts for the K band for the SMC.

d) Differential star counts for the IRAS Band 1 for the SMC.

Figure B-5: Magallemic cloud comparisons.

### B.3.8 Validation Results For Horizontal Slices

The CBSKY4 model was run for large regions in both the K band and IRAS Band 1. Here, the whole sky was divided into 18 regions each the full 360 degree longitude extent by 10 degrees of latitude extent. The latitudes where contiguous 10 degree intervals. The code showed excellent agreement the Cohen SKY4. The plots of Figure B-6 all showed excellent agreement; however, only two are included in this document.

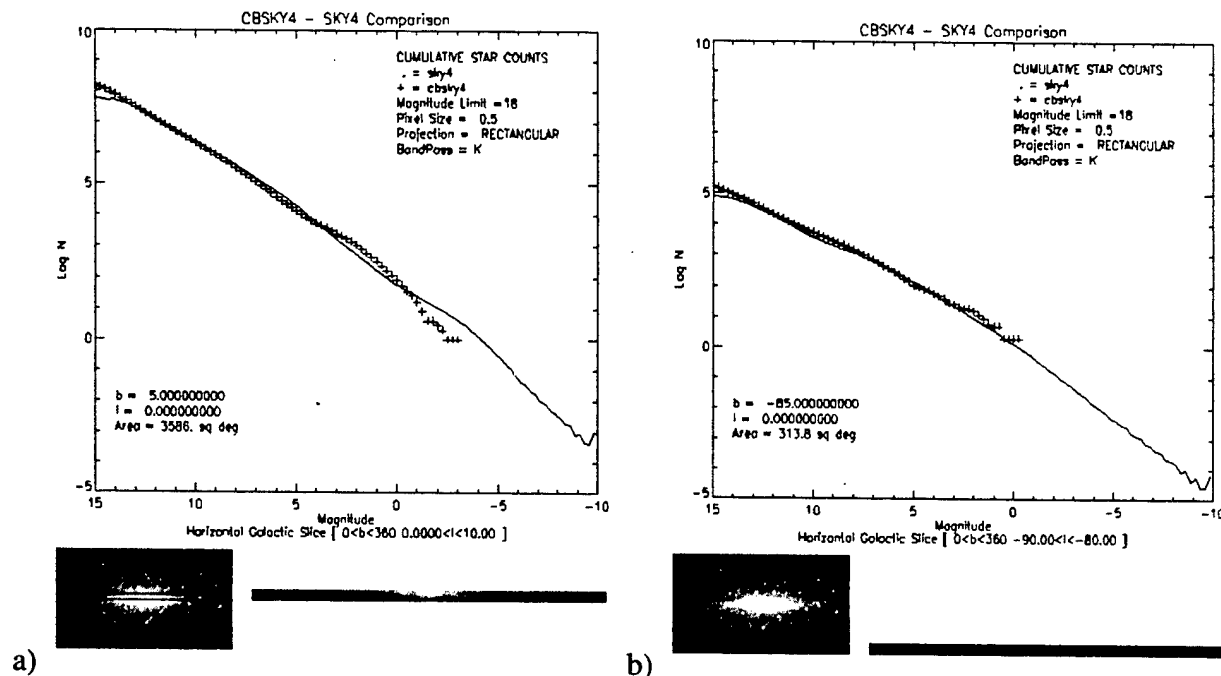
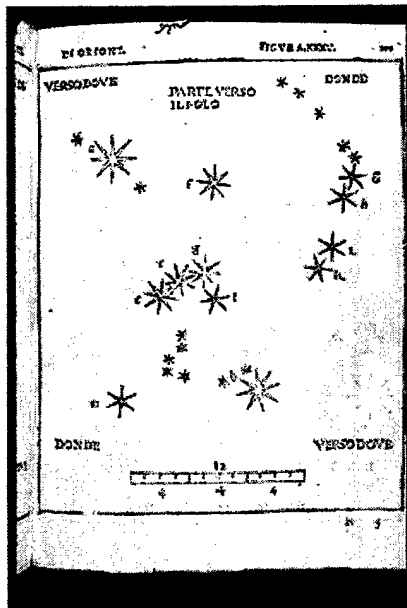


Figure B-6: K band cumulative star counts of horizontal slices parallel to the Galactic Plane. a) Horizontal slice  $5^\circ$  north of the galactic plane. b) Horizontal slice  $5^\circ$  away from the South Galactic Pole.

## B.4 Implementation of Star Catalogs

### B.4.1 Historical Notes

Ptolemy's star catalogs were among the first tabulations of stellar positions and magnitudes. Piccolomini's *On the Fixed Stars* (1540) is probably the first star atlas (Figure B-7a), since Piccolomini charted the actual positions of the stars, rather than presenting constellation figures with the stars filled in at random. His depiction of Orion, based on Ptolemy's catalog (Figure B-7b), is much more accurate than earlier pictures based on drawing the figure of Orion. Piccolomini also used a magnitude scale, so that brighter stars are represented by larger symbols. The Piccolomini atlas went through at least ten editions between 1540 and 1570.



a) Piccolomini's Star Atlas

Star Name	Longitudo	Latitudo	Magnitudo
Aldebaran	150° 00'	16° 30'	1
Rigel	150° 00'	7° 30'	2
Saiph	150° 00'	11° 30'	2
Antares	150° 00'	23° 30'	1
... (many more stars listed)			

b) Ptolemy's Star Catalog

Figure B-7: Example star atlas and star catalog.

### B.4.2 Validation of Catalog Use

To verify star catalog inputs, we validated that the selected star catalog data was read and interpreted, and that units of flux and position are consistently carried through the program execution for final star placement. For this validation, select regions were analyzed for completeness and accuracy against the star catalogs.

Table B-10 was generated for a model run of the Orion region with 3 different spectral bands. The table on the next page lists the output of a catalog with a catalog limit of magnitude 3 for the V spectral band. Orion is famous for its hot, young OB stars (Cohen Type 30). The shaded stars are from the brt\_iras.dat file. The other stars are from the brt\_bsc5.dat file.

**Table B-10: Output of CBSKY4 for the Orion region.**

Right Ascension	Declination	Magnitude	Class
68.262278	16.409710	-0.1738654	21
72.424535	14.169373	2.7787196	22
78.029306	-8.256815	-0.8680001	30
82.319068	18.559455	2.4490589	32
83.174611	-5.495305	-1.1767017	1
83.257945	-5.295801	-2.1422117	1
88.114508	7.400883	-1.4928668	32
91.331987	-6.374648	1.1022027	85
92.491647	18.003777	2.7210263	85
92.963563	22.523927	2.8706929	25
94.403635	-10.614598	0.7322221	84
94.982804	22.540709	2.3545027	25
68.262888	16.407713	0.8913612	32
76.346241	-5.150663	2.7909519	5
78.033512	-8.257995	0.1309763	30
80.611888	6.305895	1.6817131	30
82.359820	0.263732	2.2813688	30
83.246491	-5.941264	2.8290252	30
83.418656	-1.232277	1.7396323	30
84.558543	-1.967674	2.0993074	30
86.346074	-9.686005	2.1054589	30
88.116216	7.399391	0.5001933	12
94.984511	22.539618	2.8873885	25

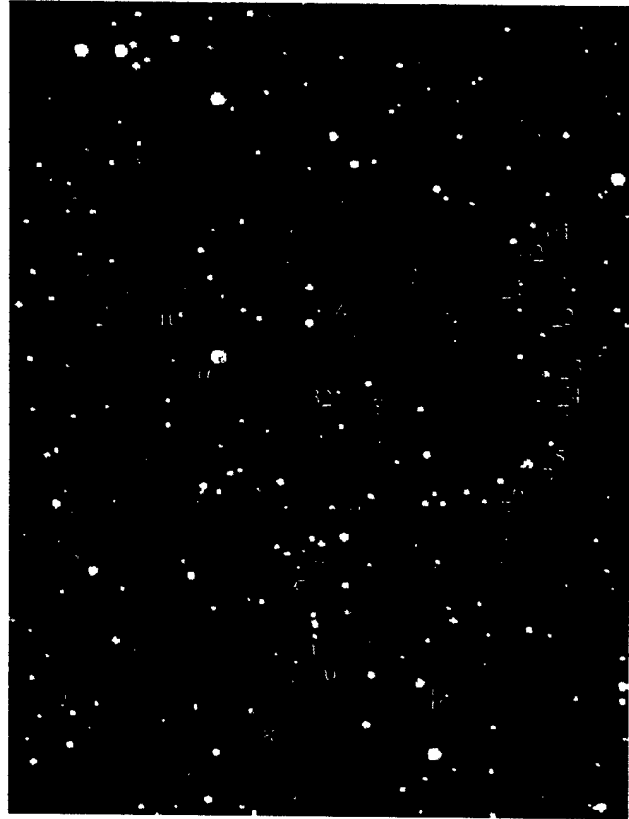


**Figure B-8: Chart of the Constellation Orion with the brightest stars labeled.**

Table B-11 gives a finding list for the first few IRAS stars:

**Table B-11: The brightest IRAS stars of Figure B-8.**

RA(J2000) Deg	Dec(J2000) Deg	Class	Magnitude
68.9794	16.5112	21	-3.48
73.1324	14.2518	22	-1.20

When the first values are precessed to B1950 coordinates (the reference equinox of the input cbsky4.inp file was B1950) the RA/Dec (68.262279, 16.409710) matches the listing values. Thus, the output catalog is in the coordinate system with equinox being the user input. Likewise the star listing in the brt\_bsc5.dat file: (68.9800 16.5092 32 0.785) when precessed yields: RA/Dec (68.262891, 16.407712). It was also validated that when the reference\_frame is set to another equinox, the catalog listing has the RA/Dec values referenced to that equinox.

### **B.4.3 Finding Stars From Other Catalog Listings**

The list of stars of Table B-12 was taken from a set of IR spectra found at <ftp://adc.gsfc.nasa.gov/pub/adc/archives/catalogs/3/3045/>. This data set contains the relative fluxes for 46 spectra (30 stars plus the Sun), ranging in spectral type from A0 to M7. Spectra of seven carbon stars are included. Although some spectra cover the wavenumbers from 2500 to 8200, many spectra do not include wavenumbers less than 4000 and there are many gaps as a result of atmospheric absorption.

The star coordinates are listed, and the results of finding the corresponding catalog stars are presented in the table on the next page. It is not surprising that there are discrepancies between the listings, since the reported values may be truncated, thus not preserving the 2 arcsec accuracy. The greatest deviation was found in Arcturus (alpha Boo). This was not surprising since the NASA spectra were acquired in the late 1960s, and considering the proper motion of Arcturus (2.28 arcsec/year) listed in the table of the 20 brightest stars in Table B-4.

Sometimes, there is a corresponding star in both the Yale Bright Star Catalog and the IRAS Catalog. This could result in an over-estimation of brightness because the star might be included twice. Furthermore, the two catalogs do not necessarily assign the star to the same Cohen SKY4 spectral class.

**Table B-12: CBSKY4 Catalog Stars Corresponding to NASA Archive of IR Spectra Stars  
(RA / Dec in J2000)**

Star Name	NASA's Archive Listing			CBSKY4 IRAS Listing			CBSKY4 Yale Bright Star Listing		
	RA	Dec	Spectral Class	RA	Dec	Cohen Spectral Class	RA	Dec	Cohen Spectral Class
$\sigma$ Cet	34.8363	-1.02556	M6 e	34.8345	-2.97410	27 (M5 III)	34.8362	-2.97750	29 (M7 III)
$\rho$ Per	46.2917	38.8417	M3 II III	46.2971	38.8446	26 (M4 III)	46.2942	38.8403	33 (M3-4 I-II)
$\alpha$ Tau (Aldebaran)	68.9792	16.5119	K5 III	68.9794	16.5112	21 (K4,5 III)	68.9800	16.5092	32 (K-M2 I-II)
W Ori	76.3483	1.17750	C 5,3	76.3459	1.17980	47 (AGB C 01)	-	-	-
$\alpha$ Ori (Betelgeuse)	88.7925	7.40694	M1-2 lab	88.7912	7.40840	32 (K-M2 I-II)	88.7929	7.40690	12 (M0-1 V)
$\epsilon$ Gem	93.7204	22.5069	M3 III	93.7193	22.5077	25 (M3 III)	93.7192	22.5067	25 (M3 III)
$\mu$ Gem	95.7392	22.5150	M3 III	95.7383	22.5147	25 (M3 III)	95.7400	22.5136	25 (M3 III)
UU Aur	99.1367	38.4456	C 5,3	99.1390	38.4455	48 (AGB C 03)	-	-	-
$\alpha$ CMa (Sirius)	101.295	-15.3006	A1 V	101.285	-16.7112	4 (B8-A0 V)	101.287	-16.7161	5 (A2-5 V)
VY CMa	110.743	-24.2325	C M3-5e la-lab	110.744	-25.7688	39 (AGB M 11)	-	-	-
X Cnc	133.845	17.2311	C 5,4	133.847	17.2299	47 (AGB C 01)	-	-	-
R Leo	146.889	11.4294	M8 e	146.889	11.4280	29 (M7 III)	146.890	11.4289	29 (M7 III)
U Hya	159.387	-12.6161	C 7,3	159.378	-13.3834	48 (AGB C 03)	159.388	-13.3844	33 (M3-4 I-II)
Y CVn	191.283	45.4400	C 5,4	191.282	45.4369	47 (AGB C 01)	-	-	-
R Hya	202.429	-22.7186	M7 e	202.428	-23.2849	29 (M7 III)	202.428	-23.2814	29 (M7 III)
$\alpha$ Boo (Arcturus)	213.931	19.2103	K2 III p	213.919	19.1895	20 (K2,3 III)	-	-	-
$\delta$ Oph	243.587	-2.30778	M0.5 III	243.585	-3.69590	23 (M1 III)	243.586	-3.69440	22 (M0 III)
$\alpha$ Sco (Antares)	247.352	-25.5683	M2 Ia	247.343	-26.4333	32 (K-M2 I-II)	247.352	-26.4319	23 (M1 III)
$\alpha$ Her	258.662	14.3897	M5 IB-II	258.660	14.3880	27 (M5 III)	258.662	14.3903	33 (M3-4 I-II)
$\gamma$ Dra	269.151	51.4892	K5 III	269.147	51.4865	21 (K4,5 III)	269.152	51.4889	21 (K4,5 III)
T Lyr	278.083	36.9989	C 6,5	278.081	36.9970	48 (AGB C 03)	-	-	-
$\alpha$ Lyr (Vega)	279.231	38.7797	A0 V	279.230	38.7801	4 (B8-A0 V)	279.235	38.7836	5 (A2-5 V)
$\delta^2$ Lyr	283.626	36.8986	M4 II	283.623	36.8969	26 (M4 III)	283.626	36.8989	33 (M3-4 I-II)
R Lyr	283.833	43.9450	M5 III	283.826	43.9437	27 (M5 III)	283.834	43.9461	27 (M5 III)
$\chi$ Cyg	297.641	32.9147	M p,e, s	297.639	32.9133	29 (M7 III)	-	-	-
EU Del	309.477	18.2675	M6 III	309.478	18.2676	28 (M6 III)	309.478	18.2692	28 (M6 III)
$\mu$ Cep	325.876	58.7800	M2 Ia	325.874	58.7805	32 (K-M2 I-II)	325.877	58.7800	32 (K-M2 I-II)
$\beta$ Peg	345.940	28.0808	M2-3 II-III	345.939	28.0833	33 (M3-4 I-II)	345.944	28.0828	24 (M2 III)
19 Psc	356.598	3.48722	C 6,2	356.598	3.48980	47 (AGB C 01)	-	-	-
R Cas	359.601	51.3883	M7 e	359.602	51.3916	29 (M7 III)	359.603	51.3886	29 (M7 III)

### B.4.4 Catalog Synthesis with Statistical Stars

We also validated that when CBSKY4 synthesizes star catalog data and SKY4 statistical stars, the statistical distributions of bright stars are not skewed. The real stars are added to the statistical stars. No changes are made to the SKY4 log(N) vs. magnitude statistics prior to including statistical stars in the image and output. The Orion image of Figure B-8 was run for the K band for real stars only, statistical stars, only, and the synthesis of real and statistical stars. Table B-13 shows that the number of real stars is a very small fraction of the statistical star count. The Log(N) vs. Log(S) plots of Figure B-9 show no significant changes to the statistics when catalog stars are included.

**Table B-13: Star Counts for Options of Statistical and Real Stars**

Real Stars Only	Statistical Stars Only	Real and Statistical Stars
526	5190557	5191083

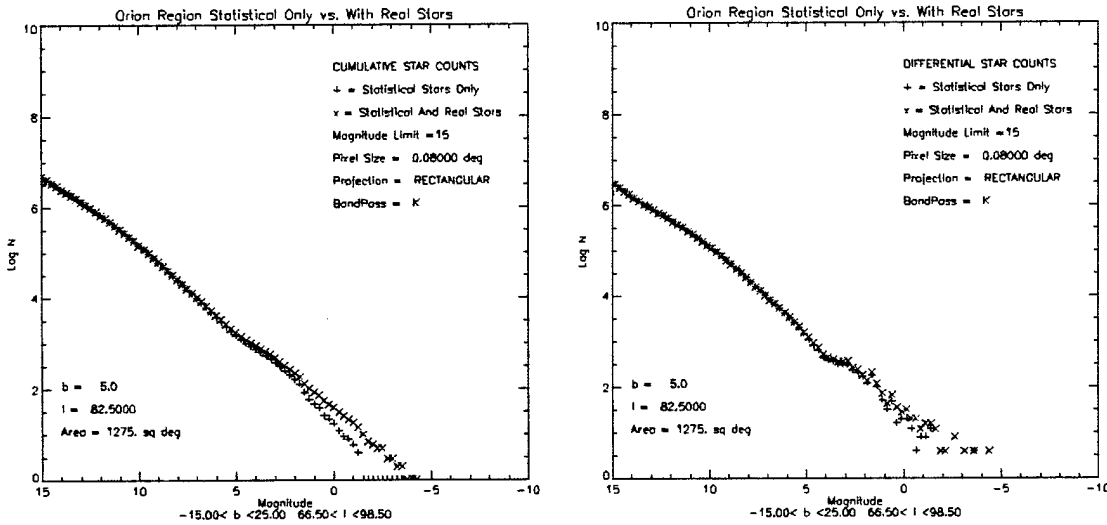


**Figure B-9: Log(N) vs. Log(S) Plots Show No Skewing with Inclusion of Catalog Stars**



## B.5 Predictive Positional Validation

### B.5.1 Different Projections

The code was run centered on one star for the various map projections, etc., and appears to be inserting the star in the correct pixel. The positional accuracy of the output image depends on the pixel resolution.

### B.5.2 Convolution Applied

When a convolution is applied, the star is convolved into the image with its position at the center of the pixel that its coordinate falls into, thus some positional accuracy is lost in the convolution process. The accuracy depends on the user's definition of the pixel size.

## B.6 Predictive Flux Validation

### B.6.1 Flux of Arcturus In Different Bands

Arcturus is included in the IRAS catalog at RA=213.918500 degrees, Dec=19.189500 degrees (J2000). The reported 12 $\mu$ m apparent magnitude is -3.6197126. IRAS lists Arcturus as a Cohen spectral class 20, (K2, 3 III). The pixel size for the simulation is 0.00027 degrees on a side. The values are consistent with the

$$F = F_0 \cdot 10^{-m/2.5}$$

formula, given the CBSKY4 pre-defined flux at magnitude zero values. Thus, it appears that the flux computation in different bands is valid (assuming that the conversion from 12 $\mu$ m magnitude to the in-band magnitude is correct). Table B-14 gives the flux for Arcturus in a variety of bands.

**Table B-14: CBSKY4 Flux Values for Arcturus Run for different output spectral band options.**

Band	Code Output Flux [W/CM2/MICRON]	Code Output Flux [W/CM2]	Code Output Magnitude	CBSKY4 F <sub>0</sub> (W/m <sup>2</sup> )
B	5.25431e-012	5.14923e-013	0.247906	6.47E-09
V	9.40025e-012	8.36623e-013	-0.984032	3.38E-09
J	2.58173e-012	9.81059e-013	-2.72832	7.95E-10
H	2.77867e-012	8.33600e-013	-3.37896	3.71E-10
K	8.23927e-013	3.95485e-013	-3.48933	1.59E-10
2.4UM	6.23605e-013	5.61245e-014	-3.36938	2.52E-11
12UM	2.21931e-015	1.55352e-014	-3.61971	5.539E-12
25UM	1.30369e-016	1.45362e-015	-3.67997	4.903E-13
1565A	simulation failed			1.118E-9
1400A	simulation failed			2.44E-9
1660A	simulation failed			1.044E-9

### B.6.2 12 $\mu$ m Flux of Arcturus In Different Units

Arcturus is included in the IRAS catalog at RA=213.918500 degrees, Dec=19.189500 degrees (J2000). The reported 12 $\mu$ m apparent magnitude is -3.6197126. IRAS lists Arcturus as

a Cohen spectral class 20, (K2,3 III). The pixel size for the simulation is 0.00027 degrees on a side. Table B-15 gives the flux of Arcturus at 12 $\mu$ m in different units. Table B-16 shows the relationship between the units and W/cm<sup>2</sup>.

**Table B-15: CBSKY4 12 $\mu$ m Flux Values for Arcturus Run for Different Output Unit Options.**

cbsky.inp Units Parameter Value	12 $\mu$ m Flux
W/CM2	1.55352e-014
W/CM2/MICRON	2.21931e-015
JY	25.9444
W/CM2/SR	0.000699575
W/CM2/MICRON/SR	9.99393e-005
MJY/SR	not implemented in CBSKY4
MJY	not implemented in CBSKY4
JY/SR	not implemented in CBSKY4

**Table B-16: Formulas for Conversion between Units (Using W/cm<sup>2</sup> as Reference)**

Units	Radiance	Conversion factor from W/cm <sup>2</sup> to this unit
W/cm <sup>2</sup> /sr/ $\mu$ m	Average Spectral Radiance	(pixels/radian) <sup>2</sup> / ( $\lambda_{\max}$ - $\lambda_{\min}$ )
W/cm <sup>2</sup> /sr	In-band Radiance.	(pixels/radian) <sup>2</sup>
JY/SR	Jansky per steradian.	(pixels/radian) <sup>2</sup> / ( $\lambda_{\max}$ - $\lambda_{\min}$ ) / (Fluxj)
W/cm <sup>2</sup>	In-band Astronomical Radiance or Flux (differs by a factor of $\pi$ from other definitions of radiosity.)	
W/cm <sup>2</sup> / $\mu$ m	Average Astronomical Spectral Radiance	1 / ( $\lambda_{\max}$ - $\lambda_{\min}$ )
JY	Jansky	1 / ( $\lambda_{\max}$ - $\lambda_{\min}$ ) / (Fluxj)

For this simulation the following values:

$$(\text{pixels/radian})^2 = (180.0 / \pi \cdot 0.00027)^2 = 45031637174.372342863946428093212 / \text{rad}$$

$$(\lambda_{\max} - \lambda_{\min}) = 7 \text{ microns}$$

$$(\text{Fluxj}) = \text{The } 12 \mu\text{m flux at magnitude zero is } 5.539\text{E-}12 \text{ W/m}^2.$$

are used to find the conversion factors. The implemented units appear to have been implemented properly.

### B.6.3 User-Defined Flux at Magnitude Zero

The flux at magnitude zero feature does not appear to have been implemented to override the flux at magnitude zero of the pre-defined bands or the computed value for user-defined bands.

### B.6.4 Convolution Applied

To check out the convolution algorithm, the code was run for a very small region centered on Arcturus with the K band. Table B-17 lists the key parameters and their values.

**Table B-17: CBSKY4 Parameters Used for Testing the Convolution Routine**

<b>Key Parameters</b>	<b>Value</b>
image_projection	Rectangular
x_column_pixels	21
y_row_pixels	21
pixel_size	.00027
image_center_longitude_degrees	213.919
image_center_latitude	19.1895
units	W/CM2
Reference_Frame	J2000
coordinate_system	equatorial
positions	apparent
Reference_system	geocentric
start_wavelength	K

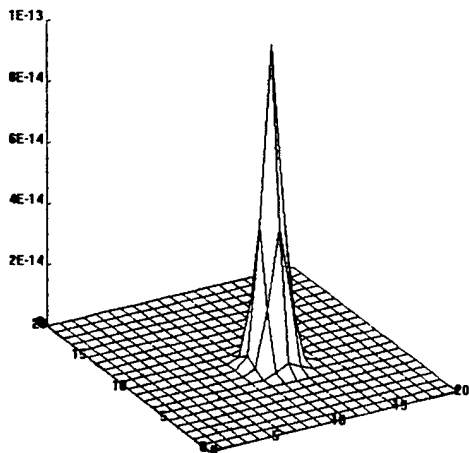
These values were run for no convolution, Gaussian convolution, and circular convolution, for a set of point-spread-function half widths, and the image statistics were tabulated. The total radiance is preserved. Spatially, the Gaussian convolution looks like a Gaussian convolution. The circular convolution has a square shape, and appears like the negative of what might be expected from a circular convolution. There probably are not many applications that would use the circular convolution option, and it has artifacts of square shape and sharp edges. Table B-18 summarizes the results of different convolutions.

Figure B-10 shows four convolution surface plots of the convolved Arcturus.

**Table B-18: CBSKY4 Output Shows Convolution Preserves Total Radiance**

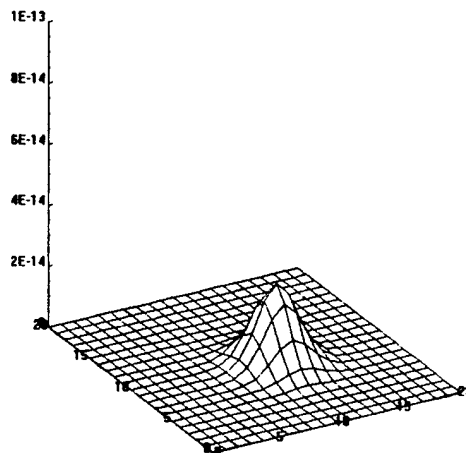
Convolution	PSF Half Width [pixels]	Maximum Image Value [W/cm <sup>2</sup> ]	Total Image Value [W/cm <sup>2</sup> ]	Output Catalog Radiance	Scaled Image
no convolution	n/a	3.95485e-013	3.95485e-013	3.9550000e-009	
Gaussian	1.100	1.04036e-013	3.95485e-013	3.9550000e-009	•
Gaussian	1.200	8.74211e-014	3.95485e-013	3.9550000e-009	•
Gaussian	1.300	7.44892e-014	3.95485e-013	3.9550000e-009	•
Gaussian	1.400	6.42279e-014	3.95485e-013	3.9550000e-009	•
Gaussian	1.500	5.59497e-014	3.95485e-013	3.9550000e-009	•
Gaussian	1.600	4.91745e-014	3.95485e-013	3.9550000e-009	•
Gaussian	1.700	4.35594e-014	3.95485e-013	3.9550000e-009	•
Gaussian	1.800	3.88539e-014	3.95485e-013	3.9550000e-009	•
Gaussian	1.900	3.48717e-014	3.95485e-013	3.9550000e-009	•
Gaussian	2.000	3.14717e-014	3.95485e-013	3.9550000e-009	•
Gaussian	2.100	2.85457e-014	3.95485e-013	3.9550000e-009	•
Gaussian	2.200	2.60096e-014	3.95484e-013	3.9550000e-009	•
circular	1.100	1.99339e-014	3.95485e-013	3.9550000e-009	•
circular	1.200	1.29097e-014	3.95485e-013	3.9550000e-009	•
circular	1.300	1.29097e-014	3.95485e-013	3.9550000e-009	•
circular	1.400	1.12984e-014	3.95485e-013	3.9550000e-009	•
circular	1.500	8.06600e-015	3.95485e-013	3.9550000e-009	•
circular	1.600	8.06600e-015	3.95485e-013	3.9550000e-009	•
circular	1.700	7.25787e-015	3.95485e-013	3.9550000e-009	•
circular	1.800	7.25787e-015	3.95485e-013	3.9550000e-009	•
circular	1.900	5.51151e-015	3.95485e-013	3.9550000e-009	•
circular	2.000	5.05068e-015	3.95485e-013	3.9550000e-009	•
circular	2.100	5.05069e-015	3.95485e-013	3.9550000e-009	•
circular	2.200	4.00249e-015	3.95485e-013	3.9550000e-009	•

Gaussian Convolution with PSF = 1.100 Radiance in W/CM2



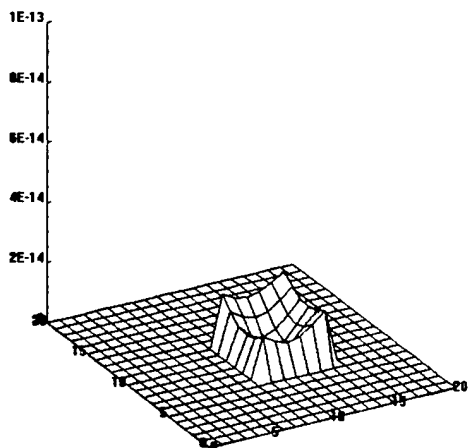
a) Gaussian PSF= 1.1 pixels

Gaussian Convolution with PSF = 2.200 Radiance in W/CM2



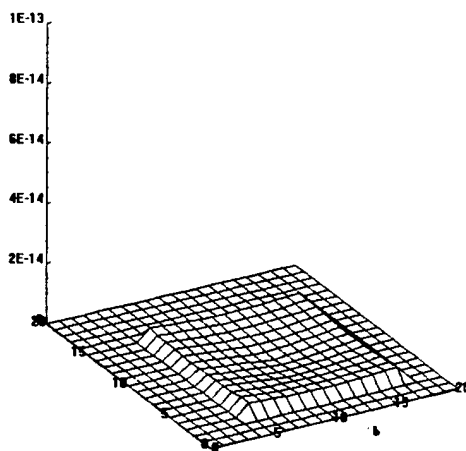
b) Gaussian PSF = 2.2 pixels

Circular Convolution with PSF = 1.100 Radiance in W/CM2



c) Circular PSF = 1.1 pixels

Circular Convolution with PSF = 2.200 Radiance in W/CM2



d) Circular PSF = 2.2 pixels

**Figure B-10: Surface plots of the result of convolving Arcturus with different functions.**

### B.6.5 Comparison To Measured Spectra

The Arcturus example was run for a series of contiguous user-defined bands, each  $0.2 \mu\text{m}$  in width, from  $2 \mu\text{m}$  to  $6 \mu\text{m}$ . The radiance values of Arcturus in the output images were plotted as a spectrum. This spectrum is compared with the corresponding Cohen Spectral Class 20 spectrum, converted from the CBSKY4 distribution file library.dat to  $\text{W}/\text{cm}^2/\mu\text{m}$ . In the IRAS bright star catalog, Arcturus is assigned to Class 20, the K2, 3 III stars.

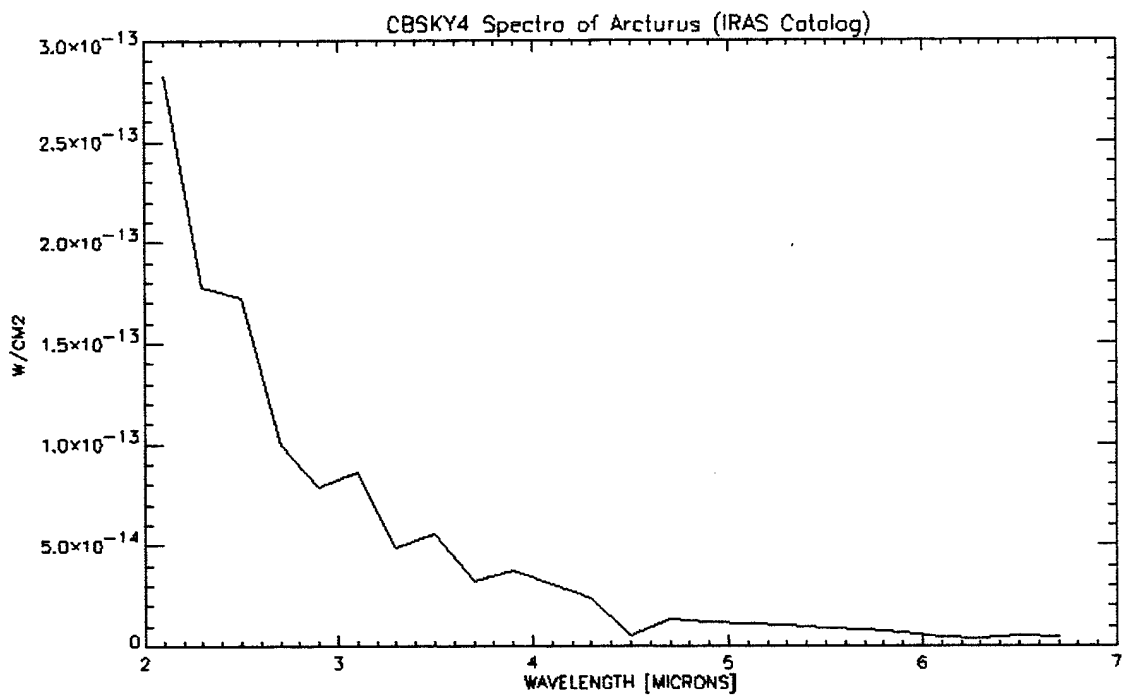
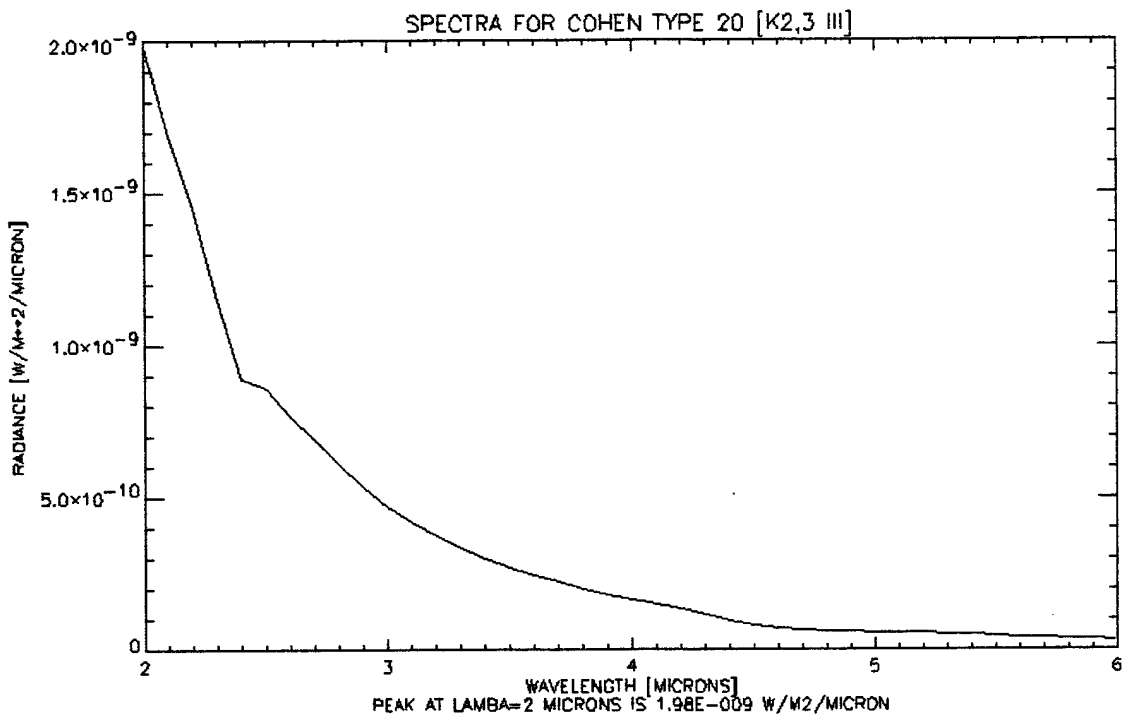


**Figure B-11: Comparison of Original Cohen Class 20 spectrum (top) with the generated spectrum from CBSKY4 (bottom).**

Finally, these spectra are compared to a measured spectrum of Arcturus of Figure B-12 (units are not reported) acquired at <ftp://adc.gsfc.nasa.gov/pub/adc/archives/catalogs/3/3045/>. This spectra is reported to be of Alpha Bootis, a K2 III p star, taken on March 14, 1968, and covering wavenumbers 3900-8200  $\text{cm}^{-1}$ . For comparison, the values were converted to units per micron, and only the 2 to 6  $\mu\text{m}$  portions plotted.

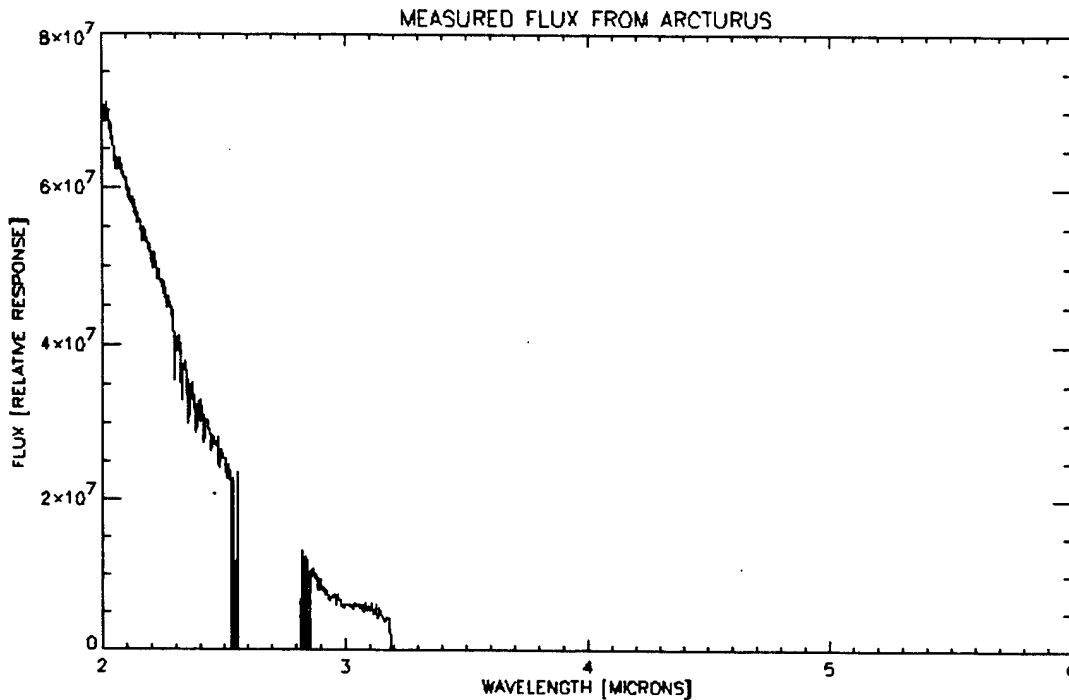


**Figure B-12:** Measured spectrum of Arcturus from the NASA/GSFC ADC archive.

### **B.7 Code Operation Validation**

The code operation performs according to descriptions provided in the user's manual. One idiosyncrasy is that even when statistical stars are turned off, the code still produces a 0 length *.sta* (Log(N) vs. Log(S)) file; however, this has no impact on the user. This will be corrected in future updates of the model.

### **B.8 Acceptance Regression Validation**

A set of test cases has been adopted for code validation through code changes. This test set may be revised however due to code changes. These test cases are provided with the model.

### **B.9 Documentation Validation**

The code performs according to the descriptions provided in the user's manual.

## **B.10 Summary**

When applied within the limitations noted in this report, the CBSKY4 model has been shown to produce high fidelity physics-based, celestial background simulations with the accuracy required to support the development of MDA electro-optic sensors/systems.

This validation is based on comparisons of the CBSKY4 model using the following benchmarks:

- The Cohen SKY4 Model
- The Yale Bright Star Catalog
- IRAS & MSX Bright Infrared Stars

CBSKY4 thus represents the state-of-the-art with regard to modeling the effects of celestial performance, and operation of MDA target detection systems. CBSKY4 can be used with confidence to meet the accuracy and speed requirements for backgrounds modeling in support of MDA system simulations.



## References

- Cohen, M. (1993). "A Model of the 2-35  $\mu\text{m}$  Point Source Infrared Sky," *Astron. J.*, **105**, 1860.
- Cohen, M. (1994a). "Powerful Model for the Point Source Sky: Far-Ultraviolet and Enhanced Midrange Performance," *Astron. J.*, **107**, 1993.
- Fraknoi, Morrison, and Wolff (2000). *Voyages Through the Universe*, Saunders College Publishing.
- Gray, David (1976). *The Observations and Analysis of Stellar Photosphere*, Wiley.
- Hoffleit, Dorrit (1964). *Catalog of Bright Stars*, Yale University Observatory.
- Mihalas, D. (1978). *Stellar Atmospheres*, W. H. Freeman and Company.
- Piccolomini, Alessandro (1540). *On the Fixed Stars*, Venice.
- Sillion, Francois and Claude Puech (1994). *Radiosity and Global Illumination*, Morgan Kaufmann.
- Unsöld, A. and B. Baschek, (1991). *The New Cosmos*, Springer-Verlag.

## Web Sites with Data

<ftp://adc.gsfc.nasa.gov/pub/adc/archives/catalogs/3/3045/>.

<http://www.krysstal.com/brightest.html>

## Web Sites with Historical Astronomy Information

<http://www.lhl.lib.mo.us/pubserv/hos/stars/pto.htm>

<http://www.phys-astro.sonoma.edu/BruceMedalists/BM2H-L.html>

<http://www.phys-astro.sonoma.edu/BruceMedalists/BM2O-P.html>

<http://www.mtwilson.edu/Education/History/cal88/cal1188.html>

<http://www.mtwilson.edu/Education/History/cal89/cal1189.html>

<http://www.mtwilson.edu/Education/History/cal90/cal1090.html>